DEVELOPMENTAL BIOMECHANICS OF EARLY VERTEBRATE EMBRYONIC TISSUES

by

Jian Zhou

Bachelor of Science, ZheJiang University, 2003

Master of Science, University of Toledo, 2006

Submitted to the Graduate Faculty of

Swanson School of Engineering in partial fulfillment

of the requirements for the degree of

Doctor of Philosophy

University of Pittsburgh

2010

UNIVERSITY OF PITTSBURGH

SWANSON SCHOOL OF ENGINEERING

This dissertation was presented

by

Jian Zhou

It was defended on

January 6th, 2010

and approved by

Kris Noel Dahl, Assistant Professor, Chemical Engineering and Biomedical Engineering, Carnegie Mellon University

Michael S. Sacks, John A. Swanson Endowed Chair in the Swanson School of Engineering, Department of Bioengineering

James H-C. Wang, Associate Professor, Departments of Orthopaedic Surgery and Bioengineering

Dissertation Director: Lance Davidson, Assistant Professor, Department of Bioengineering

DEVELOPMENTAL BIOMECHANICS OF EARLY VERTEBRATE EMBRYONIC TISSUES

Jian Zhou, PhD

University of Pittsburgh, 2010

Embryonic development involves a fundamental biomechanical process that constructs complicated three-dimensional tissue structures through massive cellular movements. During early gastrulation stages, polarized cell intercalation movements drive the dramatic extension of the *Xenopus laevis* frog embryo in the anterior-posterior direction. How those individual cellular protrusive forces integrate to produce the bulk force at the tissue level remains unknown. Furthermore, the embryo is shaped not only by active forces, but also by the mechanical properties such as the viscoelastic properties of the constituent tissues. Although rapid progresses have been made to identify the genes or proteins involved in this process, there is much less known about mechanical roles of the genes and proteins in the process. By investigating the contribution of subcellular-, cellular-, and tissue-level structures to the tissue mechanical properties, we found that, on the tissue-level, there were large temporal and spatial variation in tissue stiffness of dorsal isolates and the stiffness was largely dependent on paraxial mesoderm tissues, while notochord tissue, which has been proposed to support the early embryos, was not a major contributor to the tissue mechanics. On the cellular-level, the mechanical properties of dorsal isolates were mainly dependent on cells, but not their ECM. On the subcellular-level, the mechanical properties of the embryonic cells were determined by actin and myosin II contractility, while microtubules indirectly controlled the tissue stiffness by regulating actomyosin network through a Rho-GEF mediated signaling pathway. In order to measure the

tissue extension forces, we developed a high throughput technique combining imaging techniques and finite element models. Using this technique, we identified two cases of mechanical adaptation. In the first case we found that dorsal axial tissues generated less force to compensate for their own lower mechanical resistance. In the second we found that dorsal axial tissues encountering a stiffer environment were capable of generating nearly 2-fold greater force. These cases of adaptation demonstrate that force production is quantitatively balanced during CE and that the mechanisms responsible for this adaptation are able to ensure robust morphogenesis against environmental and genetic variation in physical force production and tissue stiffness.

TABLE OF CONTENTS

LIST OF FIGURES

PREFACE

I would like to thank the members of this dissertation committee for their stimulating comments and helpful suggestions. I thank Dr. Sachin Velankar for his helps on performing the mechanical tests of agarose gel using rheometer. I would like to thank Dr. Lance Davidson for the opportunity to join his great lab and for his extremely patient guidance and wonderful mentoring. I would like to thank my lab mates for their helps and discussions and particularly thanks to Hye Young Kim for the fruitful cooperation, thanks to Lin Zhang for making molecular constructs for this work and thanks to Dr. Michelangelo von Dassow and Sagar Joshi for the inspiring suggestions to this dissertation. Finally, I would like to thank my family, without their supports I could not finish this work. Especially, I would like to thank my wife Xiaochun, who came here to be with me, and we were very happy to have our baby Alan to join us.

1.0 INTRODUCTION

1.1 EMBRYONIC DEVELOPMENT

Gastrulation is a critical process in embryonic development, during which dorsal isolates extend along their anterior-posterior axis, deform the whole embryo from a ball shape to a tube-like shape, separate it into three germ layers and thus establish a basic body plan for embryos setting the environment for organogenesis (**Figure 1**). The three germ layers include endoderm, mesoderm and ectoderm, which develop into different tissues and organs. For example, the inner-most germ layer, endoderm, develops into the internal organs, such as liver and pancreas; the middle layer, mesoderm develops into tissues such as somites, notochord, bone, and muscles; and the outermost germ layer, ectoderm, develops into tissues, such as skin, brain, and nervous system (Stern, 2004).

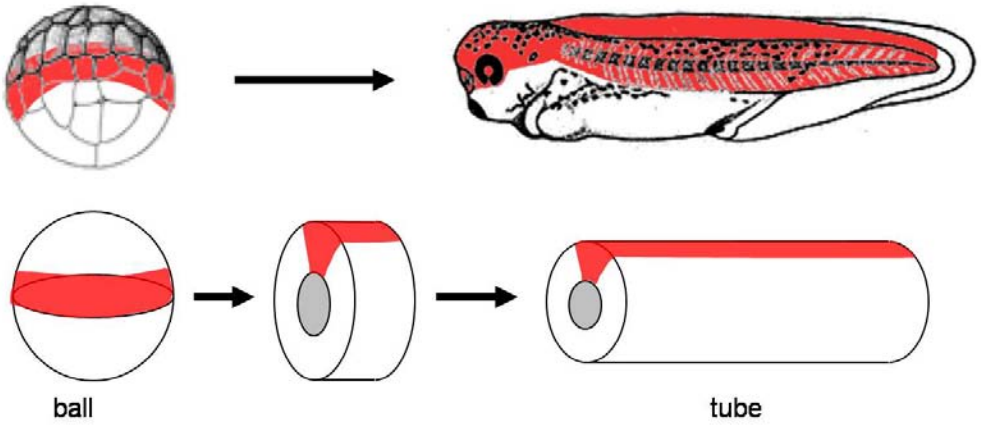

Figure 1.Gatrulation deforms embryo from a ball-like to a tube-like shape (From Lance Davidson).

Gastrulation involves massive cellular and tissue movements such as involution, invagination, convergent extension and epiboly (Gilbert, 2006). Convergent extension is one of the most important tissue movements in vertebrate embryos, during which cells intercalate between each other in a directed manner, elongate the whole embryo along the anterior-posterior axis while narrowing in the medial-lateral direction (Keller et al., 2003). Convergent extension has been proposed to be driven by a cellular rearrangement movement called mediolateral cell intercalation (**Figure 2**), during which polarized cells constrain their lamellipodia protrusions to the mediolateral direction, slide between each other by frequently breaking and reforming adhesions to pull the neighboring cells towards midline, and change their shapes to become elongated in the mediolateral axis (Keller, 2002).

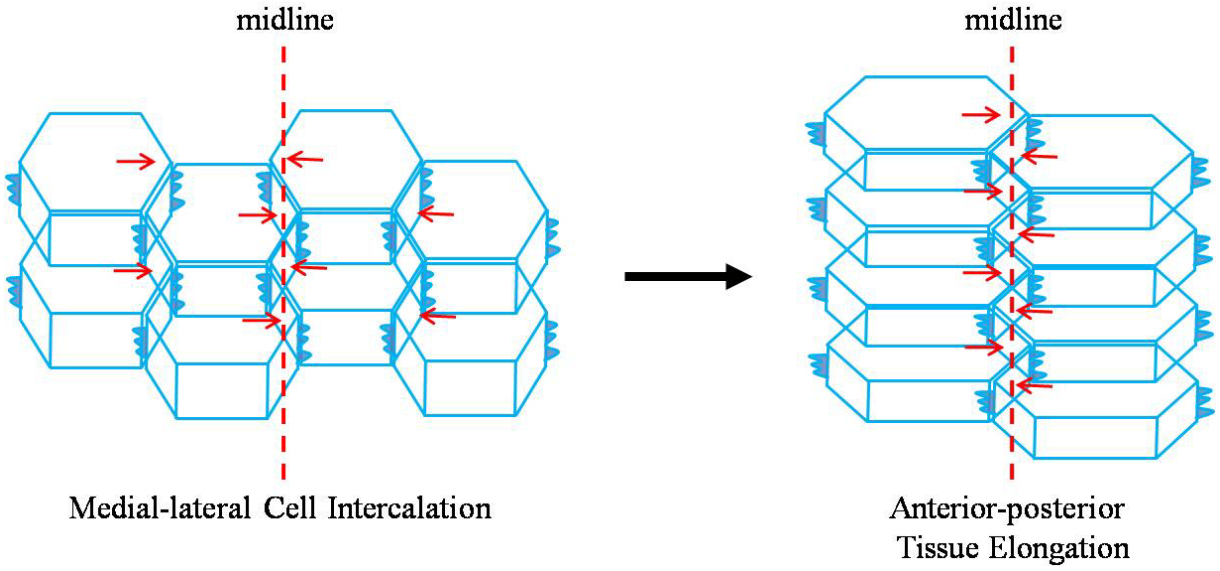

Figure 2. Convergent extension is driven by mediolateral cell intercalation.

The polarized cell protrusive activities are molecularly regulated by upstream non-canonical Wnt/planar cell polarity (PCP) pathway which directs otherwise randomly oriented protrusions into the mediolateral direction (Wallingford et al., 2002). The PCP components

include extracellular protein Wnt 11, transmembrane protein frizzled 7 (Fz) and intercellular signaling proteins dishevelled (Dsh) and Daam1 (Keller, 2002). They control convergent extension by modulating the cytoskeletal effectors, such as actin cytoskeleton and myosin II through small GTPase molecules such as Rho, Rac and cdc42 (Habas et al., 2003; Tahinci and Symes, 2003).) Recently, more and more genes and subcellular proteins have been identified to direct the CE movement. For example, by controlling cytoskeleton network, ECM or cellular adhesions, these genes regulate the cellular behavior, such as converting otherwise randomly oriented protrusions into the mediolateral direction (**Figure 3**). However, due to the difficulties to measure the tissue mechanics, there is very limited information about how these genes or proteins pattern the tissue mechanics. For example, it is not clear how the cytoskeleton regulates cellular traction force, which integrates to produce extension forces at tissue level, or how the cytoskeleton or ECM controls the cell shapes and maintains the cellular tension, which determine the deformability of cells or tissues (**Figure 3**). It is also not clear whether there is feedback between force and stiffness. To fill these gaps, we proposed to study the both active force production and passive tissue mechanical properties of embryonic tissues.

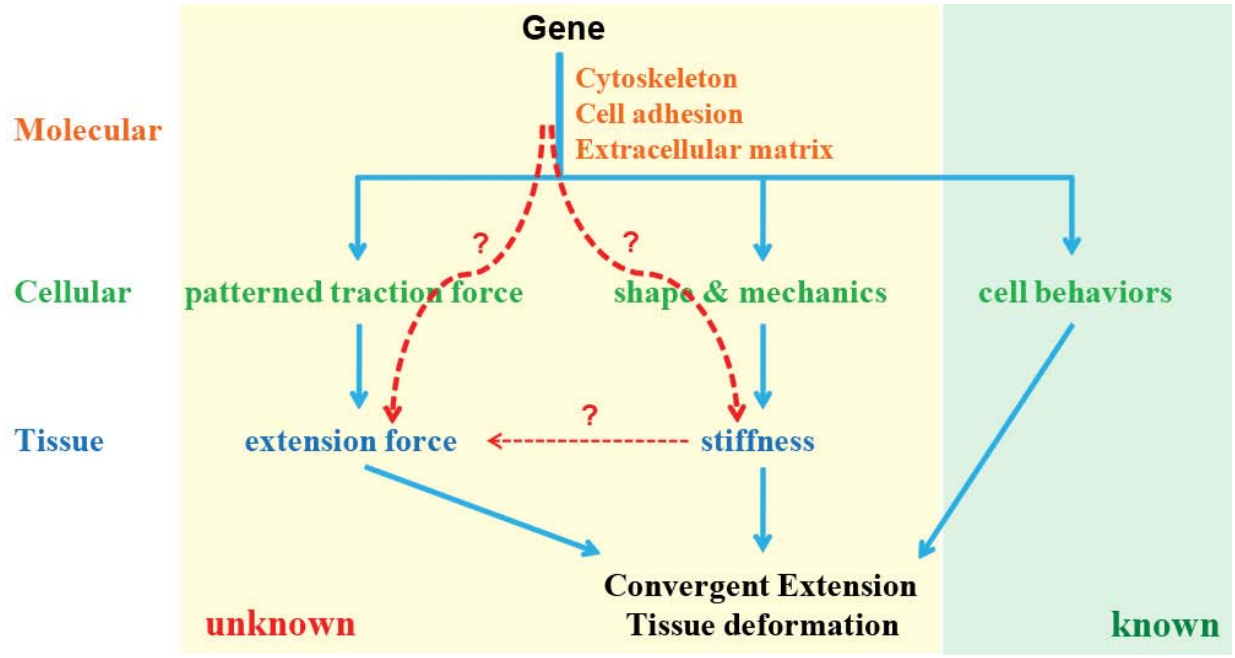

Figure 3. PCP pathway directs convergent extension through cytoskeletal effectors which patterns the cellular traction forces and cell stiffness.

1.2 DEVELOPMENTAL BIOMECHANICS

Embryonic development is fundamentally a mechanical process, and the change of the tissue shapes must be governed by basic physical principles. For instance, the degree of the tissue deformation (or cell deformation) must be proportional to active forces, which drive the deformation, and must be inversely proportional to passive tissue mechanical properties (or cellular mechanics) such as stiffness, which resist the deformation.

From a microscopic perspective, the tissue deformation is driven by the intercalating cells. During mediolateral cell intercalation, multiple arrays of polarized cells exert traction forces on their neighbors to pull them toward midline, rearrange their positions, and increase the

number of cells in the mediolateral axis continuously (**Figure 2**). During the same time, the intercalating cells are changing their shapes. The cells become narrowed in the anterior-posterior axis as they are stretched in the mediolateral direction due to the mediolateral tension produced by the polarized protrusions. The net result is tissue extension along the anterior-posterior direction with more and more deformed cells (**Figure 2**). During the process, molecular forces such as actomyosin contractility convert into cellular traction forces to rearrange the cells and maintain the tension in cells to determine their deformability (Gardel et al., 2006; Wang et al., 2002).

From a macroscopic view, dorsal isolates actively extend over 10% per hour along their anterior-posterior axis by the internally generated forces. The anterior-posterior elongating forces are converted from and thus dependent on mediolateral cellular traction forces. The extending forces not only deform the tissue itself, but also drive the surrounding tissues to deform as the whole embryo elongates, while the magnitude and rate of tissue deformation is also determined by the passive tissue mechanical properties, which are dependent on the mechanics of cells and extracellular matrix (Keller et al., 2000b). Lastly, the passive mechanical properties of the embryo such as stiffness affect the ability of cells to resist deformation induced by traction forces, transmit forces between cells and absorb energy to avoid tissue bending.

The active forces and passive mechanical properties not only physically construct the three-dimensional tissue structures, but may also provide feedback to remodel embryonic cells, their extracellular matrix, and cellular adhesions. For instance, substrates could mechanically affect cell motility. Embryonic tissues serve as substrates for cells in their neighboring tissues to migrate (Keller et al., 2000a). And cells increase their rates of motility and traction forces on stiffer substrates compared to flexible ones (Lo et al., 2000; Pelham and Wang, 1997; Peyton and

Putnam, 2005). Furthermore, the substrate could regulate multiple other cellular processes such as gene or protein expression and cell differentiation through signaling pathways (Desprat et al., 2008; Discher et al., 2005; Engler et al., 2006; Farge, 2003; Katsumi et al., 2002). Although active forces and passive mechanical properties at both cellular- and tissue-level are thought to play significant roles during tissue morphogenesis, very little is known about what these roles are and how they are regulated. To fill these gaps, we proposed to study the both active force production and passive tissue mechanical properties of embryonic tissues.

1.3 MULTI-SCALE TISSUE MECHANICS

Convergent extension provides a great opportunity for us to understand the role biomechanics plays in the formation of constituent tissues from individual cells, since it integrates active forces and passive mechanical properties at multiple scales ranging from the molecular- to the cellular-, and up to the tissue-level. For example, molecular forces such as actomyosin contractility are converted into cellular traction forces, which in turn are integrated to produce tissue elongation forces through direct cell-cell adhesion or indirect cell-ECM adhesion. Additionally, the mechanical properties of molecular structures such as actin or intermediate filaments determine the cellular mechanics, which in turn regulate the stiffness of embryonic tissues.

The mechanical response of a tissue to an external load is determined by the material and its architecture. Dorsal isolates contain three germ layers: ectoderm, endoderm and mesoderm; mesoderm can be further divided into notochord and pre-somitic tissues (**Figure 4**). Each tissue component is mainly composed of newly formed extracellular matrix (ECM) and densely packed cells which are inter-connected by cellular adhesions such as cadherin-mediated cell-cell

adhesion or integrin-based cell-ECM adhesion. The mechanical properties of embryonic cells are determined by their intracellular structural proteins such as nucleus (Lee et al., 2007; Philip and Dahl, 2008) and cytoskeleton (Gardel et al., 2008; Ingber, 2003; Trickey et al., 2004). The subcellular cytoskeletal structures include the actomyosin network, intermediate filaments and microtubule meshwork. They maintain cell shapes and mediate cellular functions such as cell motility, cell division and cell polarity.

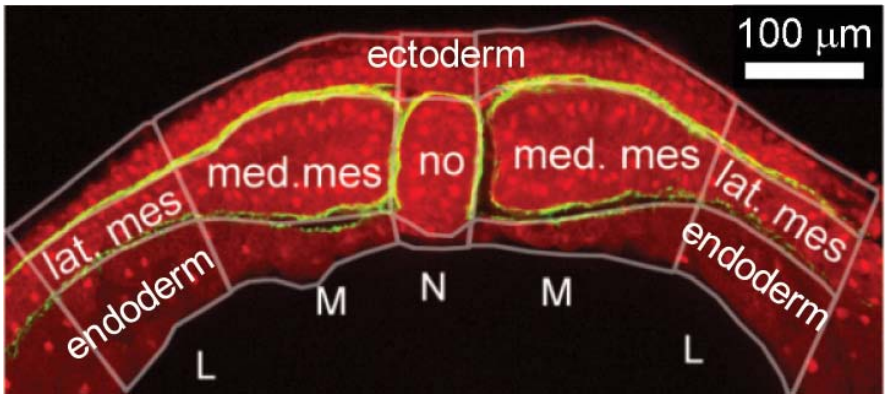

Figure 4. Basic structures of a dorsal axial tissue.

Individual components of a dorsal isolate shown with rhodamine-dextran (red) and fibrillar fibronectin matrix (green) include neural ectoderm, notochord (no), medial (or paraxial) somitic mesoderm (med.mes), lateral somitic medoserm (lat.mes) and endoderm. Lateral (L), Medial (M), and notochord (N).

1.3.1 Mechaical contribution of tissue-level structures

The basic tissue structure of dorsal isolates is composed of ectoderm, endoderm, notochord, and somitic mesoderm tissues (**Figure 4**). Each of these tissues may have distinct mechanical properties due to the differences in their cell types, cell sizes, cell shapes, or cellular behaviors. For example, both mesoderm and neural ectoderm cells actively converge and extend during gastrulation and neurulation stages (Keller and Shih, 1992; Keller et al., 1992b), while endoderm

cells do not. Moreover, in contrast to mesoderm cells which display bipolar protrusive activities along their mediolateral direction, cells from neural tissues converge using monopolar protrusions (Elul and Keller, 2000; Elul et al., 1997). In zebrafish, the cell-cortex tension of individual ectoderm cells measured by AFM is higher than that of mesoderm cells, and followed by endoderm cells, while the adhesive force between endoderm cells is smaller than that of mesoderm and ectoderm cells (Krieg et al., 2008).

The notochord is a midline axial structure in vertebrate embryos and plays both important signaling and mechanical roles in embryonic development. As a molecular signaling center, notochord induces surrounding tissues such as neural floor plate (Takaya, 1977). As a support structure, notochord has clear mechanical roles in both early and late developmental stages. In early-stage embryos (at the beginning of convergent extension or late gastrulation stages), notochord cells are the first groups of cells which adopt bipolar behaviors and thus become the driving forces for convergent extension (Keller, 2002; Shih and Keller, 1992). In late-stage embryos (tail-bud stages), notochord continues to elongate and starts to straighten by raising the internal pressure causing by swelling cells and increased density of collagen fiber sheath (Adams et al., 1990; Koehl et al., 1990). However, the mechanical role of notochord during axial elongation and neural tube closure stages is controversial. Notochord is thought to pattern morphogenetic movements and drive axial elongation. Evidence comes from several sources. For example, embryos had shortened dorsal axes when the notochord tissue was ablated by either microsurgery or gene mutation during axial elongation and neurulation (Jacobson and Gordon, 1976; Kitchin, 1949; Talbot et al., 1995). However, other studies challenged the results by showing that embryos, which is absent of notochord tissue by ultraviolet-irradiation, are normal in both axial elongation and neural tube closure (Malacinski and Youn, 1981; Youn and

Malacinski, 1981). The discrepancy between these results may be due to the early patterning function of notochord when the notochord was removed in very early stages, or due to the stage-dependencies of the mechanical function of notochord. Thus it is critical for us to determine the mechanical role of notochord during axial elongation and neurulation stages.

1.3.2 Mechaical contribution of cellular-level structures

Each tissue component such as notochord, somitic mesoderm, and endoderm is composed of cells connected by adhesions, for instance, cadherin-mediated cell-cell adhesion, or integrin-mediated cell-ECM adhesion. The degree of the cell-cell interactions or the physical properties of ECM such as fiber angle, fiber strength, and the structures of the fiber network may contribute to the tissue mechanics. For example, ECM such as collagen directly contributes to the mechanical properties of most adult biological tissues such as heart valve and blood vessels, late-stage embryonic notochord, and gastrulation stage sea urchin embryos (Adams et al., 1990; Davidson et al., 1999; Levental et al., 2007).

The major ECM components in gastrulating embryos include fibronectin, fibrillin, laminin, and their receptors such as integrin and syndecan-2 (Danker et al., 1993; Fey and Hausen, 1990; Kramer and Yost, 2002; Lee et al., 1984; Ramos et al., 1996; Skoglund et al., 2006). There is no collagen type II or elastin expressed in the early-stage embryos (data not shown). The ECM molecules form fibrils at boundaries of major components of dorsal isolates such as ectoderm, endoderm, notochord, and somitic mesoderm in the early frog embryos. For instance, fibrillin and laminin are both expressed at notochord and paraxial somite boundaries. Fibrillin is required for convergent extension (Skoglund et al., 2006; Skoglund and Keller, 2007), while the role of laminin in frog embryonic development is still not very clear (Fey and Hausen,

1990; Parsons et al., 2002). Fibronectin forms a fibrillar sheath at the boundaries between each of the three germ layers and between notochord and somitic tissues. Every mesoderm cell is directly connected with fibronectin through integrin α5β1 during late gastrulation and early neurulation stages (Davidson et al., 2004). Fibronectin plays an important signaling role during gastrulation and knockdown of fibronectin or its integrin α5β1 disrupts convergent extension (Davidson et al., 2004; Davidson et al., 2006; Marsden and DeSimone, 2001). However, evidence for a mechanical role for fibronectin is unclear. Some evidence suggests that ECM is unable to support compressive forces, for example, additional fibronectin polymerization does not increase the stiffness of cell-embedded collagen gels. However, additional fibronectin enhances the ultimate strength and toughness of the gels (Gildner et al., 2004). Fibrous ECM sheath may serve a structure role and reinforce the tissue stiffness by increasing the internal tension of encompassed tissue columns such as notochord and somitic tissues (Adams et al., 1990). Furthermore, ECM may indirectly contribute to the tissue mechanics by regulating cellular contractility (Brooke et al., 2003; Engler et al., 2008; Pelham and Wang, 1997; Peyton and Putnam, 2005). For example, cells exert forces on their surrounding ECM substrates to build internal cytoskeletal tension and thus raising the elastic modulus of substrates may increase tissue stiffness through molecular signaling pathways, such as Rho GTPase (Arthur et al., 2002; Paszek et al., 2005). Lastly, ECM may enhance the actin assembly through their integrin, which could recruit additional cytoskeletal components such as the Arp2/3 complex and formins (Blystone, 2004).

Cadherin mediated cell-cell adhesion is important to maintain tissue integrity and to transmit traction forces between cells to integrate forces at tissue level. C-cadherin is the most prominent cell-cell adhesion molecules in early frog embryos (Heasman et al., 1994; Lee and

Gumbiner, 1995). Both extra- and intra-cellular domains of C-cadherin are required for gastrulation: extracellular domains may mediate both hemophilic and heterophilic binding between cells, while intracellular domains interact with the actin cytoskeleton through proteins such as β-catenin and p120-catenin (Gumbiner, 2005; Noren et al., 2000; Yamada et al., 2005). Overexpression or disruption of these domains perturbs convergent extension (Lee and Gumbiner, 1995; Zhong et al., 1999).

1.3.3 Mechaical contribution of subcellular-level structures

How does internal cytoskeletal mechanics regulate cellular mechanics? According to the tensegrity model, cellular mechanical properties are dominated by compressed microtubules, a tension-bearing actomyosin network, and stretched radial intermediate filaments, thus modification of any of the structures would potentially affect the overall cellular mechanics (Ingber, 2003a; Ingber, 2003b).

Actin cytoskeleton is formed by cross-linked flexible actin filaments (Alberts et al., 2008), and pre-stressed by myosin II mediated contraction forces. The actin cytoskeleton transmits contraction forces from the interior cell to the extracellular matrix and neighboring cells. This cytoskeleton allows cells to generate traction forces and to sense the substrate stiffness through integrin to provide information about the cells' environment (Discher et al., 2005; Engler et al., 2008; Engler et al., 2006; Lo et al., 2000; Pelham and Wang, 1997; Peyton and Putnam, 2005; Schwarz et al., 2002). Both cellular stiffness and traction forces have been demonstrated to require an actin cytoskeleton (Elson, 1988). Disruption of the actin network decreases the elastic modulus of living cells (Ananthakrishnan et al., 2006; Kidoaki et al., 2006; Wakatsuki et al., 2000; Wakatsuki et al., 2001). Purified actin gels have similar viscoelastic properties to living

cells and the stiffness of the actin gels has been shown to be determined by physical mechanism of polymer networks (Gardel et al., 2006; Gardel et al., 2004; Valentine et al., 2005). Actin network has already been demonstrated to support the architecture and rigidity of the early blastula embryo (Kofron et al., 2002). Although the contribution of the actin network to the mechanical properties in cell culture, purified gels or early blastula embryonic cells has been demonstrated, their quantitative contribution to embryonic tissue mechanics remains unknown.

Myosin II motors can both cross-link and contract the antiparallel actin filaments and thus are essential to the traction forces and cell stiffness (Bhadriraju and Hansen, 2002). Myosin II contains two heavy chains and four light chains (Lodish, 2007). To activate myosin II, its regulatory light chain (RLC) has to be phosphorylated by either myosin light chain kinase (MLCK) or Rho kinase (ROCK) (Amano et al., 1996; Tan et al., 1992). The RLC can be dephosphorylated by myosin light chain phosphatase (MLCPase), which inactivates myosin II (Brozovich, 2002). Thus, the state of actomyosin contractility can be regulated by Rho family small GTPases such as Rho, Rac and Cdc42, while the Rho activity is activated and inactivated by guanine nucleotide exchange factors (GEFs) and GTPase-activated proteins (GAPs), respectively (Ridley, 2006). Activation of Rho increases stress fiber assembly and actomyosin contraction force through ROCK and diaphanous-related formin, mDia1 (Pellegrin and Mellor, 2007). The level of the pre-stress, the isometric tension maintained by myosin II contraction force inside cells, has been shown to correlate with cell stiffness (Stamenovic, 2005a). Decreasing myosin II activity by inhibiting Rho-associated kinase (ROCK) decreased traction force (Beningo et al., 2006) and cortical stiffness (Pasternak et al., 1989), while increasing myosin activity increased cortical stiffness (Obara et al., 1995).

Microtubules are long, but rigid hollow cylinders (Alberts et al., 2008). The role of microtubules in determining tissue stiffness is controversial because of previously reported experimental results. Disruption of microtubules may increase (Stamenovic et al., 2002; Wu et al., 2000), decrease (Potard et al., 1997; Sato et al., 1990), or have no effects on cellular stiffness (Collinsworth et al., 2002; Rotsch and Radmacher, 2000; Takai et al., 2005; Trickey et al., 2004). Furthermore, microtubules can also regulate actin organization and myosin II contractility (Danowski, 1989). Thus, there are at least two models proposed to explain the effects of microtubule on tissue stiffness. The tensegrity model or the mechanical model proposes that stiff microtubules are compressed by contraction forces generated by actomyosin network and that the reduction of the resistive force after breaking microtubules allows increased actomyosin contractility (Wang et al., 2001). Alternatively, microtubules may regulate actomyosin contractility through molecular signaling pathways. For example, microtubules in interphase cells physically bind and inactivate the Rho guanine nucleotide exchange factor, GEF-H1. When microtubules are depolymerized during mitosis or in response to nocodozale, GEF-H1 is released and induces RhoA activation. Once activated by GEF-H1, RhoA acitivates Rho kinase, which in turn phosphorylates the MLC and may down regulate myosin II phosphatase (Chang et al., 2008).

Intermediate filaments (IF) represent another major cytoskeletal component. IFs are thought to be stress absorbers due to their abilities to be extensively stretched (Herrmann et al., 2007). Thus IFs could maintain cell integrity when tissues are exposed to large deformations in both IF gels and living cells (Coulombe et al., 2000; Hutton et al., 1998; Janmey et al., 1991; Klymkowsky, 1995; Wang and Stamenovic, 2000). Intermediate filaments have been shown to interact with actomyosin (Esue et al., 2006; Tint et al., 1991) and microtubule network (Chang and Goldman, 2004), which suggests that they may play a signaling role as well. During

gastrulation stages, frog embryos express at least two intermediate filament subtypes, cytokeratin and vimentin (Klymkowsky et al., 1987; Torpey et al., 1990). Both of them are required to maintain tissue integrity during morphogenetic movements (Klymkowsky et al., 1992) and knock-out cytokeratin induced gastrulation defects possibly due to the loss of cellular adhesion (Torpey et al., 1992).

The actomyosin cortex, microtubules, and intermediate filaments may independently contribute to the tissue mechanics, but may be also physically and biochemically integrated into a network. Together with adhesions, the network forms a mechanically integrated structure potentially capable of mechanosensing and mechanotransduction.

1.4 TECHNIQUES TO MEASURE THE TISSUES MECHANICS

Frog embryonic tissues are extremely soft (3-100 Pascal), very small in size (~1 millimeter), and only able to produce as much as half microNewton elongating force during early stages, such as gastrulation and neurulation (Davidson and Keller, 2007; Moore, 1994; Moore et al., 1995). It is very challenging to measure either passive or active mechanical properties of embryonic tissue since no commercial force sensors could be directly used to report the small forces produced by the tiny frangible tissues.

1.4.1 Techniques measuring passive embryonic tissue mechanics

Passive mechanical properties are very important physical parameters to determine how a tissue deforms or resists externally applied or internally generated forces. There are several mechanical testing techniques custom designed to measure the important properties of embryonic tissue (Davidson et al., 2009a). For example, a three-point bending test was employed to measure the flexural stiffness of late-stage notochord tissues (Adams et al., 1990). A uniaxial stretch device composed of two parallel wires was designed to report the tissue stiffness of epithelial tissues (Wiebe and Brodland, 2005). Uniaxial compression devices with two plates have been used to evaluate the tissue stiffness in sea urchin blastula (Davidson et al., 1999), or reconstituted cell aggregates from chicken (Forgacs et al., 1998) and isolated tissues from *Xenopus laevis* (Moore, 1994; Moore et al., 1995). Instead of measuring the average stiffness across the whole tissue, more local mechanical information could be obtained by micro-indentation tests for chick embryonic heart tissues (Zamir and Taber, 2004a; Zamir and Taber, 2004b) or by micro-aspiration tests for *Xenopus laevis* embryonic tissues (von Dassow and Davidson, 2009). Each technique has its advantages and disadvantages. For example, it is very challenging to grip embryonic tissues due to the frangibility of the tissues for stretch devices. For tissue measurements requiring stretch, compression, or bending can directly measure the tissue mechanics, but require invasively isolating tissues from embryos. On the other hand, indentation and aspiration tests can be used noninvasively to estimate the mechanics of embryos, allowing intact embryos to develop further. However, these noninvasive tests have difficulties to define geometry and boundary conditions of the measuring tissues within an embryo, thus they are most dependent on structural models to extract the mechanical parameters from force-displacement relationships.

In Chapter 2, we used a nano-Newton force measurement device based on an early design (Davidson and Keller, 2007; Moore et al., 1995) to measure the bulk tissue mechanical properties by applying an unconfined uniaxial compression protocol. We use an invasive stress-relaxation approach but one that works with more intact tissues. Using this device, we revealed the contribution of molecular-, cellular-, and tissue-level structures to the passive tissue mechanical properties.

1.4.2 Techniques measuring active force production of embryonic tissues

Several techniques have been used to evaluate the bulk tissue-generated forces during amphibian morphogenesis. For example, a fiber optic system was demonstrated that could measure the extending force of a Keller sandwich explant made from *Xenopus laevis* frog dorsal marginal zone tissues (Moore, 1994). Another study used a pair of parallel wires glued to the superficial ectoderm to measure tension forces within early neurula stage amphibian *Ambystoma mexicanum* embryos (Benko and Brodland, 2007). The forces needed to stall neural fold closure in two amphibian species, *Triturus alpestris* and *Ambystoma mexicanum*, have been estimated with magnetically manipulated steel "dumb-bells" (Selman, 1955; Selman, 1958). All of these biophysical approaches require dedication of specialized equipment, optical fiber or thin wire force transducers or magnetically controlled dumb-bells, to measure force production within a single embryo or tissue explant for extended periods of time. Such approaches provide insights into the physical constraints of morphogenesis but are not well suited to complex analyses of mechanosensing or the molecular and mechanical coordination of morphogenesis.

In Chapter 3, we developed a reliable, high throughput technique to measure force-production by converging and extending dorsal isolates microsurgically explanted from

gastrulating *Xenopus laevis* embryos and use this technique to reveal otherwise cryptic changes in force production that balance altered tissue stiffness, allowing for robust convergent extension movements.

1.5 GOALS AND SPECIFIC AIMS

The goal of this study is to evaluate the passive mechanical properties and active force generation capacities of *Xenopus laevis* frog embryonic tissues. Embryonic development is a dynamic mechanical process. Embryos construct complicated three-dimensional structures through massive cellular movements. The dramatic extension of the early frog embryo in the anterior-posterior direction is driven by polarized cell intercalation. How those individual cellular protrusive forces integrate to generate the bulk force at the tissue level remains unknown. Furthermore, the embryo is shaped not only by active forces, but also by the mechanical properties such as the viscoelastic properties of constituent tissues. Although rapid progresses have been made to identify the genes or proteins involved in this process, there is much less known about the biomechanics of the development. Here, we combine standard mechanical tests with physical, chemical and molecular biological methods to study the mechanical properties of developing embryos at molecular-, cellular- and tissue-level and to understand how the tissue extending forces are generated and regulated.

Three aims are designed to investigate the mechanical processes of embryonic development. The first two aims evaluate the contribution of tissue architecture and cellular structures to passive loading-response properties of the tissues (Chapter 2), while the third aim provides information of the magnitude and the regulation of tissue extending forces (Chapter 3).

This work along with other research projects being carried out in our lab, such as cellular and/or tissue traction forces measured by traction force microscopy techniques, the dynamics of F-actin, and the regulation of cellular behavior and cell shapes during convergent extension will further our understanding of how embryos are shaped.

Aim 1: Characterize the temporal and spatial variation of tissue stiffness in dorsal isolates. Embryos consist of multiple tissue types and those tissues remodel themselves over time. To reveal the variation of tissue mechanical properties in time and space, we use a nano-Newton force measurement device to evaluate the stiffness (or residual elastic modulus) of dorsal embryonic tissues while manipulating its architecture by molecular and physical approaches. The aim will provide information of how various types of tissue are integrated during axial elongation of vertebrate embryos.

Aim 2: Evaluate the contribution of subcellular and cellular structures to embryonic tissue stiffness. Cells, extracellular matrix (ECM) and their interactions determine tissue mechanics. Molecular pathways direct tissue development by regulating cytoskeletal effectors which modify cellular and ECM mechanics. However, nothing is known yet about the contribution of subcellular and cellular structures to the mechanical properties of embryonic tissues. To understand the roles of cell structures in determining tissue stiffness, we use the same force measurement device to measure the stiffness of dorsal isolates while modulating their subcellular structures such as actomyosin cortex, intermediate filaments and microtubule network, and cellular structures such as cadherin mediated cell to cell adhesion and fibronectin mediated cell to extracellular matrix adhesion.

Aim 3: Investigate how mechanical environment affects forces generated by dorsal isolates. One unique property of embryonic tissues is their abilities to grow new tissues and

construct new structures continuously. The tissue formation is driven by forces internally produced by patterned cellular intercalation in the tissue. However, it is challenging to estimate how much force embryonic tissues generate and to understand what regulates the force production. In this sub aim, we develop a gel force reporting sensor based on high-resolution imaging techniques and finite element models to estimate the active extension forces of dorsal isolates while modifying their internal and external mechanical environment.

The success of these aims will reveal the roles of biomechanics in linking the tissue architecture, genetic and molecular functions in cells to three-dimensional tissue deformation that builds the form of the early embryo and shapes later organs.

1.6 SIGNIFICANCE

According to Centers for Disease Control and Prevention (CDC), birth defects occur in more than 3% of infants and are a major source of infant mortality and loss for their families. Morphogenesis is an essential period during early vertebrate life and mechanical abnormalities in embryonic development can lead to significant birth defects (**Figure 5**) such as spina bifida and anencephaly (Kibar et al., 2007). For example, an unexpected increase in tissue stiffness of axially extending dorsal isolates may induce defects in closing neural tubes which are the precursors to the central nervous system. Our work is a fundamental step towards learning how to prevent birth defects by providing in-depth understanding of the biomechanical process in tissue development, investigating the molecular sources of tissue mechanics which cause the developmental failures, and developing novel tools to further study the process.

Developmental biomechanics follow the same physical principles as traditional biomechanics, but they are distinct in that tissues dramatically undergo growth or rearrangement, processes shared with tumor growth and tissue engineering. For instance, tissue engineering and developmental biology share many of the same physical principles to construct tissues or organs from individual cells and their ECM. Mechanical rules revealed during embryonic development would potentially inspire tissue engineers to design better products for regenerative medicine (Ghosh and Ingber, 2007). For instance, our studies indicate that mechanical properties of embryonic tissues are spatially and temporally regulated as the embryo constructs organs, which suggests that tissue engineers should aim to design ECM scaffolds with both dynamic and anisotropic mechanical properties that mimic the physicochemical microenvironment of native tissues; more realistic materials may promote complex cell-cell and cell-matrix interactions appropriate to regenerate the target tissue.

Analysis of animal development from a mechanical perspective is not a new idea and there are many hypotheses about the mechanical process of embryonic development, however, these questions are still unresolved due to the lack of experimental studies. One reason for this is that it is challenging to quantitate the mechanical properties of embryonic tissues. Development of new mechanical tests and tools are essential to understand the interaction between genes or proteins, and cell- and tissue- mechanics that drive morphogenesis. We combine biochemistry, molecular biology, mechanical testing, image analysis, and finite element models to seek the links between genetic functions and tissue mechanics to answer several questions about biomechanical development.

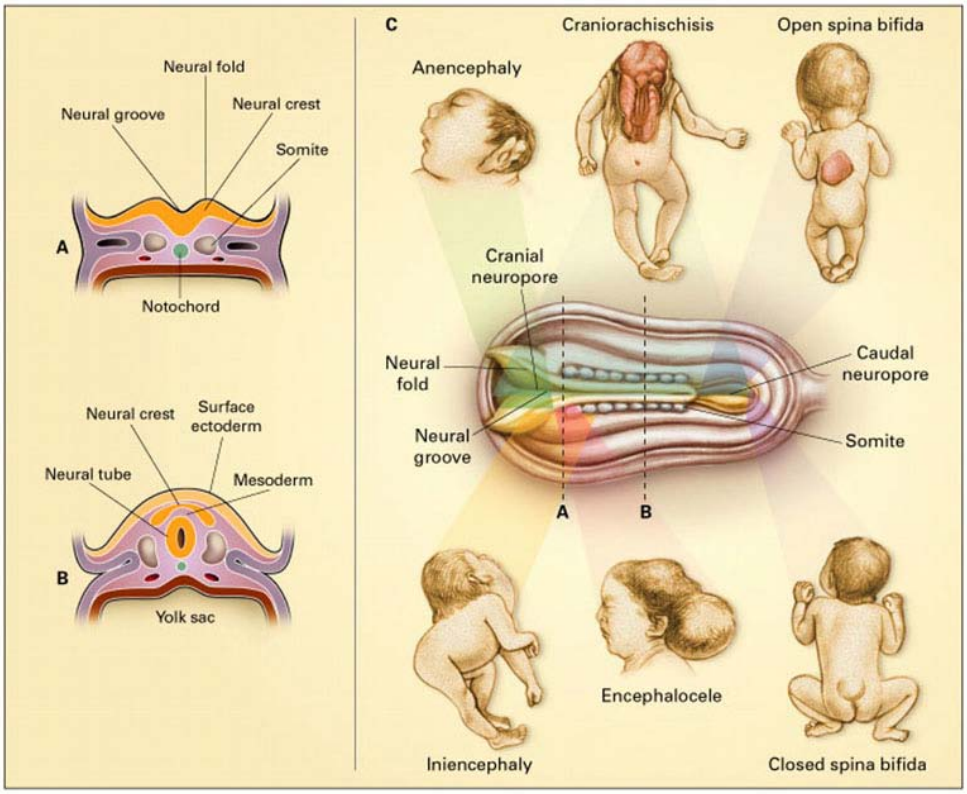

Figure 5. Normal neural-tube development in early (A) and late (B) stage and Neural-Tube Defects (C), from (Botto et al., 1999).

2.0 PASSIVE MECHANICAL PROPERTIES OF EMBRYONIC TISSUES

Although embryogenesis is a dynamical biomechanical process and numerous fundamental questions have been raised over years, such as how molecules and proteins generate and regulate force, how cellular traction forces are integrated to generate bulk tissue extension forces, and what determine the force production and mechanical properties of the tissues. Due to the technical difficulties in measuring the passive mechanical properties of small embryonic tissues, there is very limited information available to understand the biomechanical aspect of development process. To close this “information-gap”, we upgrade a nano-Newton force measurement device which was designed to test the embryonic tissue stiffness. In this chapter, we investigated the contribution of tissue-level structures such as notochord, somitic mesoderm, endoderm, and neural plates, cellular-level structures such as ECM and cadherin, and molecular-level components such as actin, myosin II, microtubules to the passive mechanical properties of dorsal isolates.

2.1 EXPERIMENTAL METHODS

2.1.1 Embryos and Microsurgery

Embryos are obtained from *Xenopus laevis* frogs (Kay and Peng, 1991), fertilized in vitro, dejellied in 2% cysteine and cultured at 14.5 - 21ºC to stage (Nieuwkoop and Faber, 1967) in 1/3X MBS (Sive et al., 2000). For microinjection, embryos are placed in 1X MBS containing 3% Ficoll. Before making explants, vitelline membranes of embryos are removed with forceps (Fine Science Tools Inc., Foster City CA) and transferred in DFA media (Danichik's For Amy; (Sater et al., 1993)). Dorsal isolates are microsurgically dissected from embryos using hair loops and hair knives (**Figure 6A**). Microsurgically isolated dorsal isolate contains consistent configuration of tissues that represent the organization of three germ layers in an intact whole embryo (**Figure 6B and 6C**).

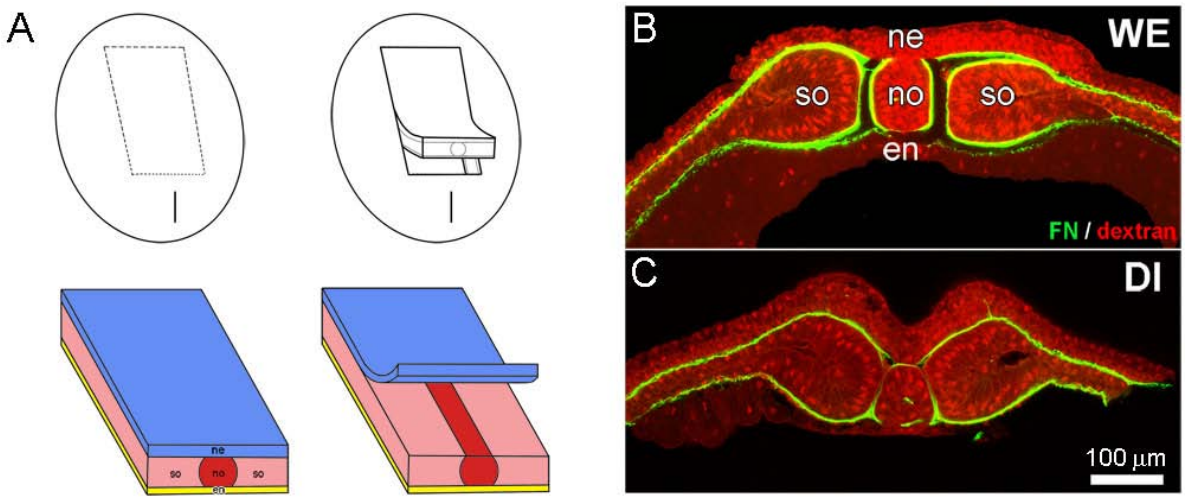

Figure 6. Microsurgery isolates dorsal isolates.

(A) Schematic of microsurgery for creating dorsal isolates (From Dr. Lance Davidson). (B) A microsurgically isolated dorsal isolate (DI) and dorsal tissues within a whole embryo (WE), shown with rhodamine-dextran (red) and fibrillar fibronectin matrix (green).

2.1.2 Histology, Immunocytochechistry and Confocal Microscopy

Fibronectin staining is used to outline the tissue architecture of dorsal isolates (**Figure 6C**) and to demonstrate the reduction of fibronectin fibrils in fibronectin antisense morpholinos injected embryos. To stain fibronectin, explants or whole embryo are fixed in 3% TCA in 1X PBS (Davidson et al., 2004). Fibronectin fibrils are recognized with primary antibody mAb 4H2 (Ramos and DeSimone, 1996) against *Xenopus* fibronectin (1:500) and visualized with a rhodamine conjugated goat anti-mouse IgG antibody (1:200, Jackson ImmunoResearch Laboratory, West Grove PA). After staining, the dorsal isolates are dehydrated in methanol and cleared in Murray's clear (Davidson et al., 2004). Fibrillin, laminin and collagen II can be fixed and stained following the same protocol as fibronectin, but instead are recognized with primary antibody mAb JB3 (1:500; Developmental Studies Hybridoma Bank; Iowa City, IA), anti-Laminin (1:100; Sigma, St. Louis, MO) and 11-116B3 (1:200; Developmental Studies Hybridoma Bank; Iowa City, IA), respectively. Single optical sections and z-series of explants are collected with a confocal laser scan head (SP5, Leica Microsystems, Inc.) mounted on an inverted compound microscope (DMI6000, Leica Microsystems, Inc.) using image acquisition software (LASAF, Leica Microsystems, Inc.). Three-dimensional reconstruction includes maximal projection and reslicing of z-series stacks is carried with an image processing software (ImageJ v. 1.38, Wayne Rasband, NIH).

2.1.3 nano-Newton Force Measurement Device

The nano-Newton force measurement device (nNFMD) is used to conduct unconfined uniaxial compressive stress-relaxation tests to measure the time-dependent viscoelastic properties of frog

embryonic tissues (Davidson and Keller, 2007; Moore et al., 1995). The standardized stress-relaxation tests provide a measure of tissue residual stiffness which is independent of the sample shape and thus could be compared with data from other studies. The details of nNFMD has been described previously (Davidson and Keller, 2007). Briefly, the device (**Figure 7A**) uses an optical fiber as a force transducer and the force is calculated according to the Hooke's law:

$$\boldsymbol{F = -k * d} \quad \textbf{(2-1)}$$

where $\boldsymbol{k}$ is the pre-calibrated spring constant of the optical fiber and $\boldsymbol{d}$ is the deflection of the fiber and is recorded by a laser-quadrant detector (UDT Instruments, Baltumore, MD). The relative position of the laser in x- or y-axis is determined from the quadrant detector by the ratio of photocurrent outputted from the four segments (**Figure 7B**) of the detector according to the following equations:

$$X = \frac{(A+D)-(B+C)}{A+B+C+D} \quad \textbf{(2-2)}$$

$$Y = \frac{(A+B)-(D+C)}{A+B+C+D} \quad \textbf{(2-3)}$$

where $\boldsymbol{X}$ and $\boldsymbol{Y}$ are voltages outputted from the detector representing laser positions in x- and y-axis, respectively, and $\boldsymbol{A, B, C, D}$ are the photocurrents on the four segments. The voltages are then converted into displacements by pre-calibrated linear voltage-displacement curve, which is obtained by using a closed-loop DC servo micropositioner with encoder (US Eurotek, Lakeview, California) to push in dicrete steps (1 μm for each step) agaist the tip of the optical fiber. The device was designed to measure the elastic modulus of regular blocks of tissues (Moore et al., 1995), and to obtain regular shaped tissues, we cut dorsal isolates into a uniform size roughly 600 μm long and 400 μm wide. Tissues are then positioned against the micropositioner-controlled backstage and brought into contact with the force probe (**Figure 7A**).

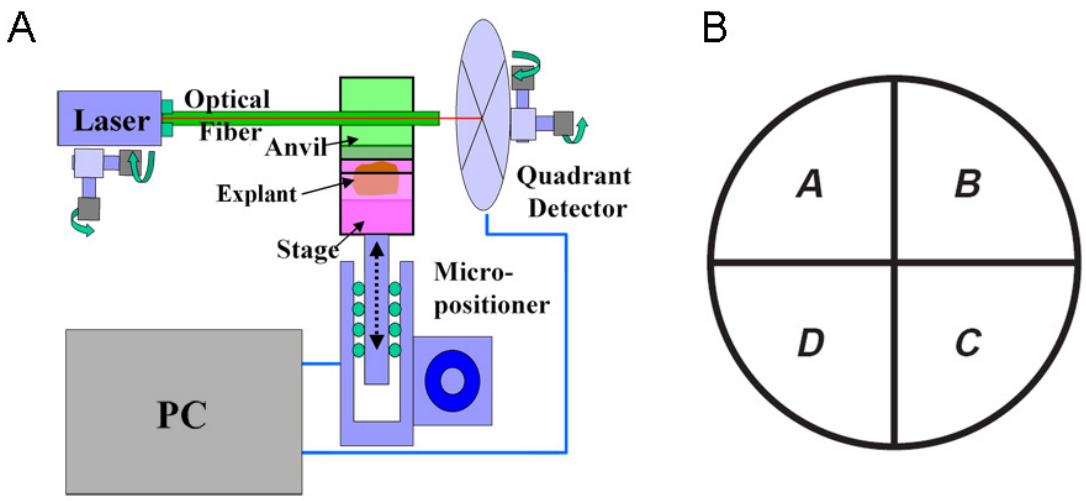

Figure 7. nano-Newton Force Measurement Device.

(A) nNFMD measures resistive forces generated by the explant in response to compression by a computer controlled optical fiber. (B) Four photosensitive segments of the quadrant detector.

2.1.4 Stress-relaxation protocol

To measure the viscoelastic properties of embryonic tissues, we use a 180-second stress-relaxation test (**Figure 8**). At the start of the test the sample is compressed by 20% of its original length along its anterior-posterior axis. The resistive force of the tissue is collected by the force probe. The time changing strain of each sample is calculated from its original and final lengths measured from a time-lapse sequence of the tissue recorded with a CCD camera mounted on a stereo microscope. Immediately after each test, the sample is fixed in MEMFA solution (Sive et al., 2000). The transverse cross-sectional area is measured from the fixed explants photographed and digitized using ImageJ (v.1.38, Wayne Rasband, NIH). With measured values of the resistive force, cross-sectional area and strain of the sample, the Young's modulus is calculated by:

$$E = \frac{stress}{strain} = \frac{\sigma}{\varepsilon} = \frac{F/A0}{\Delta L/L0} \quad \textbf{(2-4)}$$

where $\boldsymbol{E}$ is the time dependent elastic modulus, $\boldsymbol{F}$ is the resistive force measured during the stress-relaxation test, $\boldsymbol{A_0}$ is the cross-sectional area, $\boldsymbol{L_0}$ is the length of samples before compression and $\boldsymbol{\Delta L(= L_0 - L_{180})}$ is the change of length due to the compression.

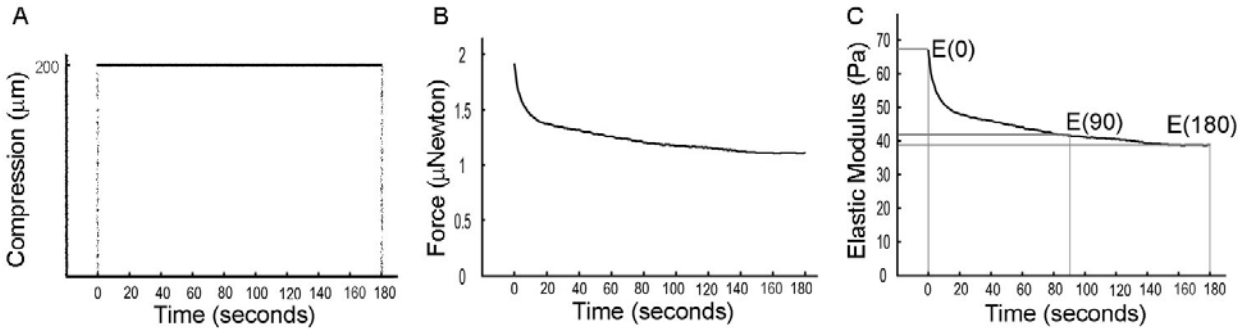

Figure 8. Stress-relaxation test measures time-dependent elastic modulus.

(A) Tissues are first compressed 200 μm along their anterior-posterior axis. (B) The resistive force of the tissue then is collected by a force probe. (C) Elastic modulus is calculated according to the equation (2-4).

2.1.5 Verification of the nano-Newton Force Measurement Device

To validate the nNFMD we first tested assumptions underlying the stress-relaxation test. One assumption we made in equation (2-4) is that the applied strain is constant. However, due to the flexibility of the optical fiber, the assumption is acceptable for the last 60 seconds during 180-second stress-relaxation tests, but the true strain is 10-30% off from the assumed constant strain for the first hundred seconds (**Figure 9**). In order to estimate the errors produced by the assumption, we calculated the elastic modulus by fitting the stress data resulting from variable strain (or true strain).

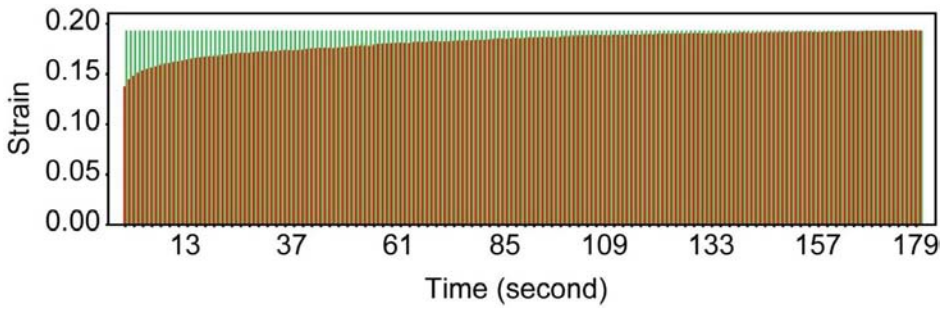

Figure 9. The measured time varying strain (red) and assumed constant strain (blue) of dorsal isolates during 180-second stress relaxation tests.

According to Boltzmann superposition theory (Findley et al., 1989), for any linear viscoelastic material, the stress responses to successive deformations are additive, from which the constitutive equation of a linear viscoelastic material is derived:

$$\sigma(t) = \int_0^t E(t-\tau) \cdot \frac{d}{d\tau}\varepsilon(\tau)d\tau \quad \textbf{(2-5)}$$

where $\boldsymbol{\sigma(t)}, \boldsymbol{E(t)}, \boldsymbol{\varepsilon(t)}$ are the time-dependent stress, elastic modulus and strain, respectively. We assume that the embryonic tissues exhibit linear viscoelastic behavior and that their elastic modulus is represented by a Standard Linear Solid (SLS) model (Findley et al., 1989):

$$E(t) = k_1 + k_2 * e^{-t/h} \quad \textbf{(2-6)}$$

where $\boldsymbol{k_1}, \boldsymbol{k_2}, \boldsymbol{h}$ represent a spring in parallel to a spring and dashpot in series, respectively. First, we fitted the strain data from experiments using a strain function, which includes a step strain plus an exponential curve:

$$\varepsilon(t) = a * H(t) + b * (1 - e^{-t/c}) \quad \textbf{(2-7)}$$

where $\boldsymbol{H(t)}$ is a step function and $\boldsymbol{a}, \boldsymbol{b}, \boldsymbol{c}$ are constants. By substituting the equation (2-7) and equation (2-8) into equation (2-6), we get the following equation:

$$\sigma(t) = b * e^{-t/c} * \left(-k_1 + h * \frac{k_2}{c-h}\right) - b * \left(-k_1 + h * e^{-t/h} * \frac{k_2}{c-h}\right) + a * (k_1 + k_2 * e^{-t/h})$$

(2-8)

Then, we estimated the parameters for the SLS model (time-dependent elastic modulus) by fitting the stress data from experiments using equation (2-9). Last, we compared elastic modulus estimated from variable strain to the elastic modulus calculated by our method. The elastic modulus from the two methods is very close, especially for the elastic modulus at 180 seconds (**Figure 10**), which we used for statistic analysis.

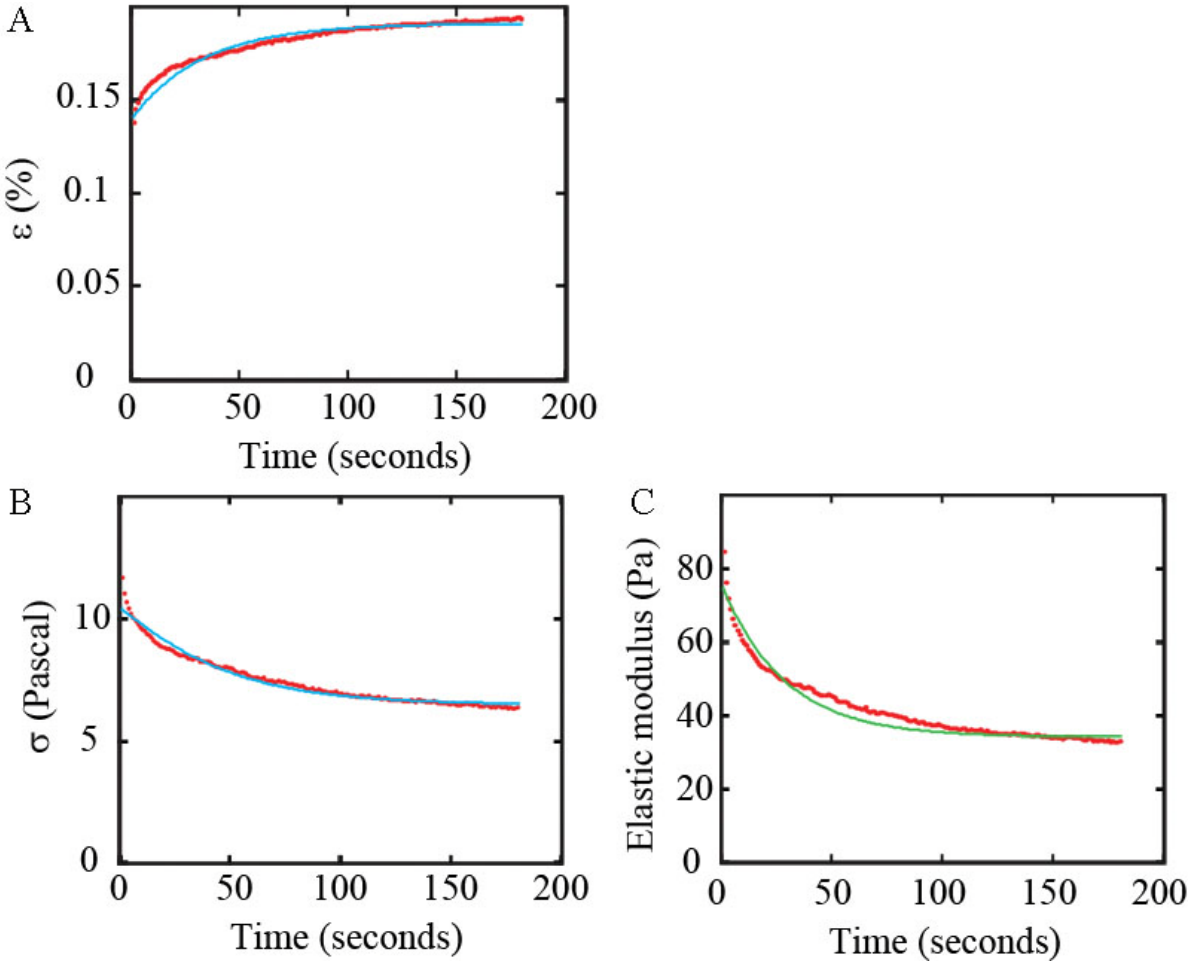

Figure 10. Experimentally measured and fitted strain ε, stress σ, and elastic modulus E.

(A) Experimentally measured (red) strain ε was fitted using a strain function including a step strain plus an exponential curve (Equation 2-8). (B) Experimentally measured (red) stress σ was fitted using (Equation 2-9). (C) Elastic modulus computed with real time-changing strain (red) was compared to elastic modulus calculated with assumed constant strain.

To further validate the ability of our nano-Newton force measurement device to measure viscoelastic properties, we measured the stiffness of a block of a known material, agarose gel, whose elastic modulus has been measured by frequency sweep shear tests using a rheometer (AR2000, TA Instruments). The stiffness of the 0.6% agarose gel (weight-volume percentage, 0.6 g per 100ml distilled H_2O) is around 30 Pascal from both measurements (**Figure 11 and Figure 37**). Thus, our device is able to accurately report the tissue stiffness in the range of very soft materials.

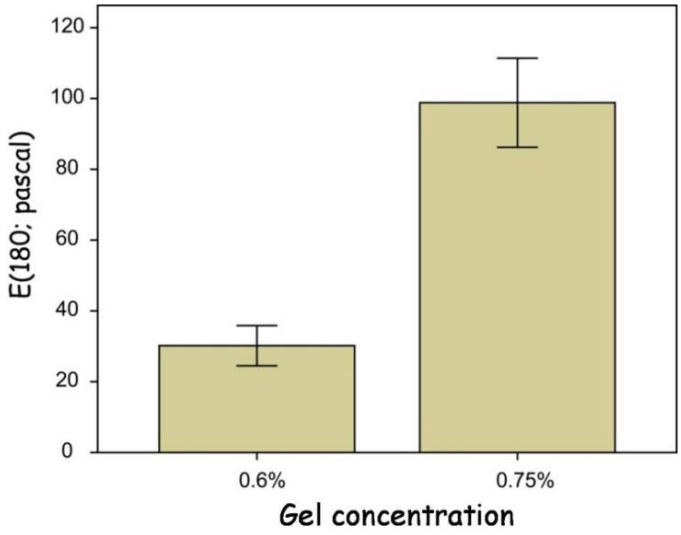

Figure 11. Residual stiffness at 180 seconds of agarose gels in different concentration measured by nNFMD.

2.1.6 Data analysis

In preliminary studies, we found clutch-to-clutch variation in the mechanical properties of embryonic frog tissues (von Dassow and Davidson, 2009). To compensate for this variance, we typically measure and compare the tissue stiffness with control and treated explants within the same clutch. Statistical tests of significance are carried out either with the non-parametric Mann-

Whitney U-test (Sokal and Rohlf, 1994) within each clutch or with two way ANOVA with treatment as a fixed factor and clutch as a random factor among multiple clutches using commercial software SPSS (v. 15, Chicago, IL). A p-value less than 0.05 is considered as statistically significant.

2.2 RESULTS

2.2.1 Characterize the temporal and spatial variation of stiffness in dorsal isolates

The early gastrulation movements divide dorsal isolates into three germ layers: ectoderm, endoderm and mesoderm, which can be further divided into notochord and somitic tissues. These tissue components are tightly coupled and undergo dramatic convergent extension, which is driven by internal generated forces and is also determined by mechanical resistance of the tissues, during later gastrulation and early neurulation stages. Thus, the mechanical properties of dorsal isolates are essential to understand the developmental process. For instance, embryonic cells use neighboring cells and possibly ECM as their substrates in each type of tissues. In order to allow other cells to move on their surfaces, tissues must be stiff enough to resist the shear forces exerted on them (Keller et al., 2003). The substrates not only support cell rearrangement, but may also provide important microenvironment cues for cells and regulate their functions (Ghosh and Ingber, 2007; Paszek et al., 2005; Schwartz and DeSimone, 2008). However, nothing is known about the mechanical properties of ECM substrates in frog embryos. To understand the mechanical principles for designing frog embryos, we first need investigate the variation of

mechanical properties both in time and space. To estimate the stiffness of dorsal isolates, we apply a stress-relaxation protocol to measure the elastic modulus of the tissues along their anterior-posterior axis over the course of 180 seconds long enough for resistive forces to reach a steady state. We then investigate the temporal variation of tissue stiffness by measuring the stiffness of same embryonic tissues from different developmental stages and determine the spatial variation in tissue mechanics by measuring the stiffness of dorsal isolates whose architecture is microsurgically or molecularly modified.

2.2.1.1 Mechanical properties of embryonic tissues

Preliminary studies showed that tissues behaved like passive viscoelastic material. In order to understand how active biological processes played a role in regulating the viscoelastic properties, we needed to characterize several mechanical phenomena known to modulate biomechanical properties of living tissues. For instance, embryonic tissues may be hardened by pre-strain or may become viscous when experienced a long-term compressive force. And there may be active responses triggered by mechanical compressions during stress-relaxation tests.

(a) Pre-strain in embryo

Since a previous study showed that pre-strain can affect the mechanical properties measured in chick embryonic heart tissues (Zamir and Taber, 2004b), we first evaluated the pre-strain presenting in dorsal isolates from frog embryos. Briefly, we selected pigment cells on the epithelial surface of the embryos as landmarks (**Figure 12A and B**). By comparing the position of these cells on the epithelium of the dorsal isolates before and immediately (within 60 seconds) after they were microsurgically removed (**Figure 12A' and B'**), we found that dorsal isolates

contracted around 10% isometrically (**Figure 12D**). Thus, the pre-strain in frog dorsal isolates is much smaller than that in embryonic chick heart tissues and is unlikely to play a major role in determining the passive mechanical properties of dorsal isolates. Such contractions may be the immediate consequence of microsurgery (Joshi et al., 2009). Wound healing did not significantly change the shape of the tissue and only affected the geometry around the corners of the isolate (**Figure 12C and C'**) over the next 5 and 10 minutes.

(b) Long-term residual stiffness

Previous studies indicated that dorsal involuting marginal zone tissues in early gastrulation stages reached a residual elastic modulus within 180 seconds (Moore et al., 1995). To validate that the tissue was not continuing to deform as a liquid, we applied a 540-second uniaxial compression test on dorsal isolates from late gastrulation and early neurulation stages and confirmed that the 180-second protocol was sufficient to reveal the long-term elastic response (**Figure 13B and C**). Since we computed the elastic modulus using uniaxial compression test, we referred to the long-term elastic modulus as stiffness for the rest of the dissertation.

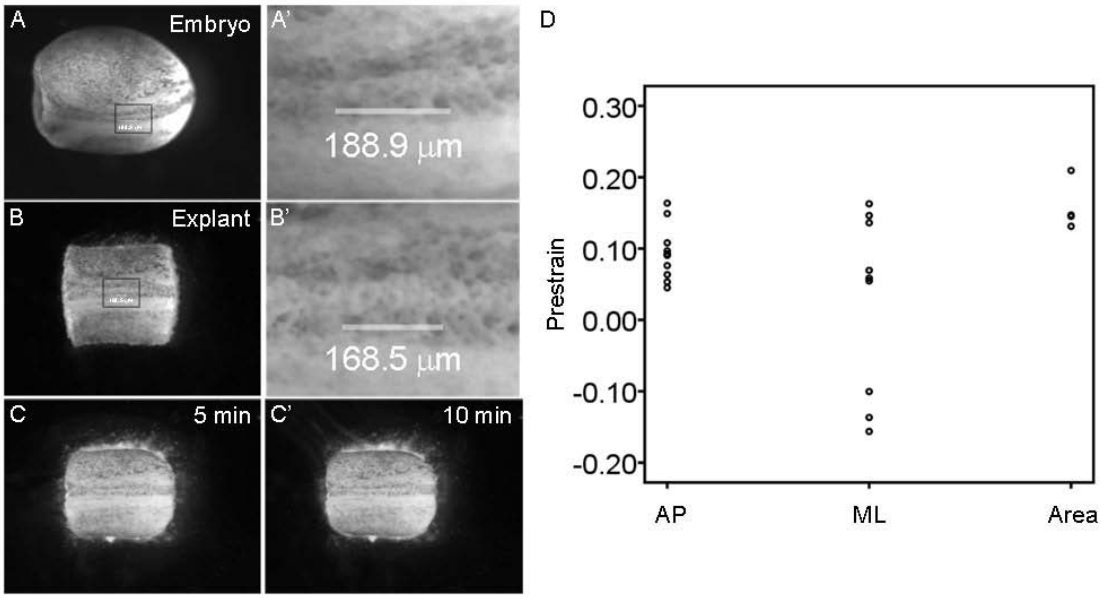

Figure 12. Pre-strain in frog embryonic tissues.

(A) Markers on dorsal epithelium of an intact embryo. (B) Markers on a dorsal isolate from the embryo in (A) within 60 seconds after microsurgery. (C) Effects of wound healing on the strain of dorsal tissues. (D) Measured pre-strain along anterior-posterior (AP), medial-lateral (ML) directions and area changes in the epithelium (data from 5 embryos and 1-3 measurements for each embryo).

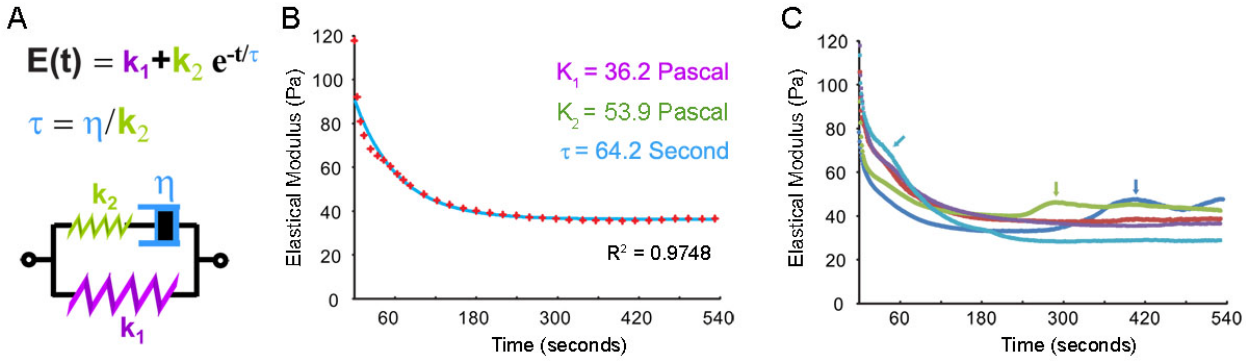

Figure 13. Long-term resistance response of dorsal isolates.

(A) Standard Linear Solid (SLS) model consists of a spring (k1) in parallel to a spring (k2) and dashpot (η) in series. (B) Elastic modulus collected over 540 seconds (red) is fitted with the SLS model (blue). (C) Five examples of dorsal axial tissues undergo 540-second stress relaxation tests and three of them have transient active contractions (arrows).

(c) Embryonic tissues maintain viscoelastic behaviors under various loads

From the stress-relaxation tests, we found that dorsal isolates behaved like a viscoelastic material, with a time independent elastic component and a time dependent viscous component (**Figure 13B**). This viscoelastic response can be modeled as a Standard Linear Solid (SLS) model (Findley et al., 1989), which uses a spring (elasticity ***k1***) to represent the elastic component, a spring (elasticity ***k2***) and dashpot (viscosity $\boldsymbol{\eta}$) in series to represent the viscous component, and combines the two systems in parallel to model the behavior of the viscoelastic material (**Figure 13A and B**). The time-dependent elastic modulus of the SLS model is:

$$E(t) = k1 + k2 * exp(-t/\tau) \quad \textbf{(2-9)}$$

where $\boldsymbol{\tau}(=\boldsymbol{\eta}/\boldsymbol{k2})$ is the relaxation time. The three parameters (***k1***, ***k2*** *and* $\boldsymbol{\eta}$) are obtained by fitting the SLS model to experimental data using nonlinear regression techniques (NLREG version 3.2; Brentwood TN). However, in the course of these analyses, we found spontaneous mechanical contractions lasting 60 to 90 seconds (**Figure 13C**). Spontaneous contractions have been noted in other studies in our lab (von Dassow and Davidson, 2009) and are thought to reflect rapid epithelial contractions (Joshi et al., 2009). The presence of these contractions compromised the fitting curves and often produced inconsistent errors in the fitted parameters, so we decided to use the long-term residual tissue stiffness, E(180), instead of fitted SLS parameters to compare the mechanical properties and to compute the statistical significance between control and treated groups.

Since embryonic tissues have been proposed to be mechanosensitive (Ingber, 2006), it has been suggested that embryonic tissues may deviate from viscoelastic behaviors after repeated compressions or under different strains. In order to test the mechanical behavior of dorsal isolates in various mechanical loadings, we first applied five repeated 180-second compressions with

identical 20% strain to the tissues (**Figure 14A**) and found that tissues became slightly stiffer under repeated compressions, but still remained viscoelastic (**Figure 14B**). We then applied 60-second uniaxial compression test with a step increasing strain (**Figure 15A**) and found that, although tissues increased elastic modulus under larger strain, they still behaved like a viscoelastic material (**Figure 15B and C**). We did not find evidence of an active cellular or tissue response to these differing strain protocols.

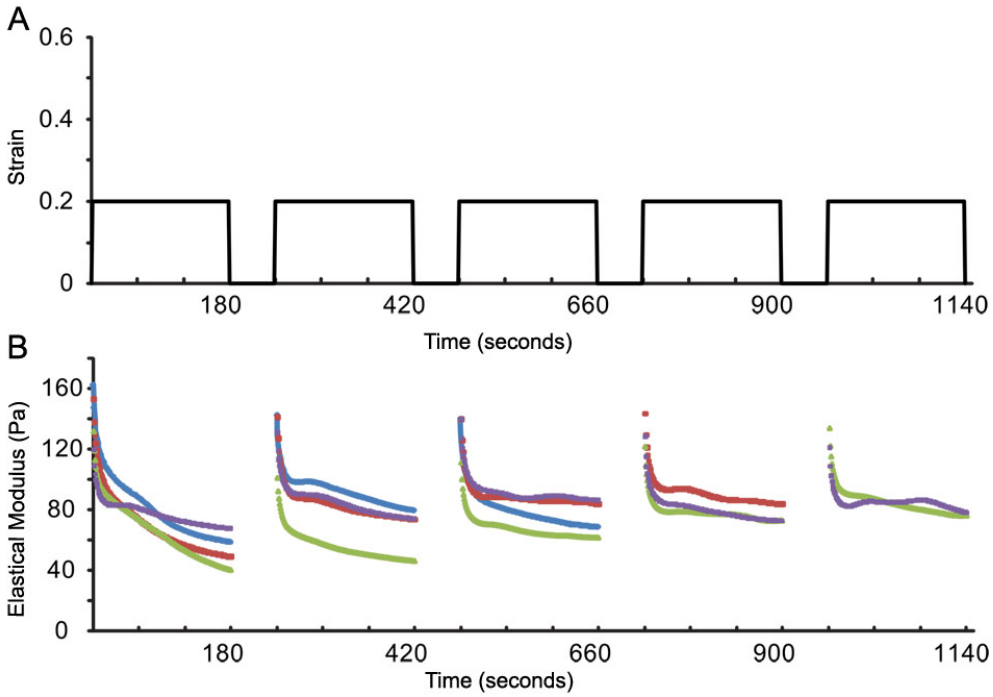

Figure 14. Dorsal isolates maintain viscoelastic under repeated compressions.

(A) Repeatedly applied strain. (B) Four examples of dorsal isolates became slightly stiffer, but remained viscoelastic under repeated compression.

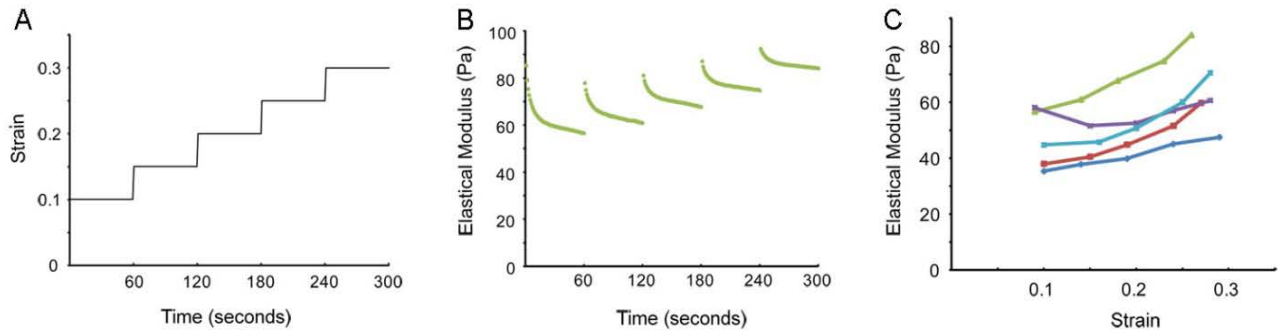

Figure 15. Dorsal isolates maintain viscoelastic under step-increasing strain.

(A) A step increasing strain with 60-second interval. (B) Elastic modulus under increasing strain. (C) Five examples of strain-stress curves of dorsal isolates.

2.2.1.2 Dorsal axial tissues stiffen during axial elongation

The 3D architecture of dorsal isolates is significantly remodeled during convergent extension. However, it is unknown whether the structure remodeling would result in the changes of their mechanical properties. A previous study (Moore et al., 1995), which focused on two specific time points during early gastrulation, has shown that involuting marginal zone tissue (stage 10+) became stiffer after moving around the blastopore lip (stage 11.5). To determine whether dorsal isolates continue to increase their stiffness as they elongate and begin neural tube closure. We measured the stiffness of dorsal isolates at several stages from mid gastrulation (stage 11) to early neurulation (stage 21). The stiffness of dorsal isolates from the same clutches, groups of eggs produced from the same female, were compared, since large variance in tissue stiffness had been found between clutches (von Dassow and Davidson, 2009). By comparing the tissue stiffness of different developmental stages, we found that dorsal isolates increased their stiffness 6- to 8-fold over as little as 8 hours (**Figure 16A**). However, even though stiffness of *Xenopus* embryonic tissues increases, it remains very compliant in comparison to most adult tissues (**Figure 16B**).

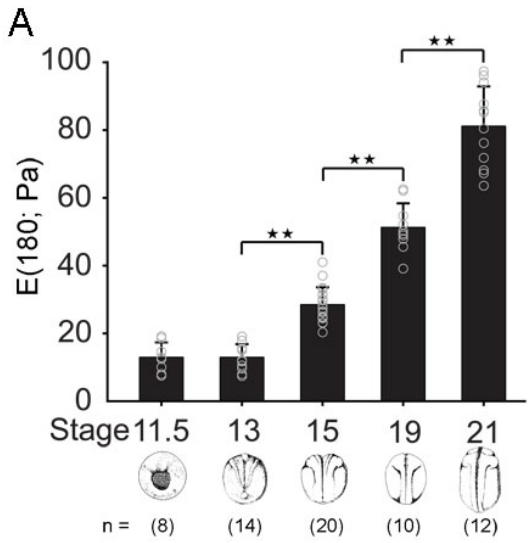

B

Tissue type	Testing method	Elastic modulus
Achilles' tendon	Tension	310 Mpa
Articular cartilage	Compression	950 kPa
Carotid artery	Perfusion	90 kPa
Lung	Tension	5–6 kPa
Brain	Indentation	260–490 Pa
Fat	Indentation	17 Pa

Figure 16. Dorsal isolates stiffen during axial elongation.

(A) Stiffness increases as dorsal axis tissues elongate. (B) Frog embryonic tissues are compliant compared to most adult tissues (Table from Levental et al., 2007).

2.2.1.3 Notochord does not contribute to the stiffness of dorsal isolates

Notochord is thought to play a major role in convergent extension in the early gastrula and straightening of the embryo at the tail-bud stage. Additionally, a stiff notochord has been proposed to support the embryo during axial elongation. To determine the contribution of notochord to the stiffness of dorsal isolates during axial elongation, we measured the stiffness of dorsal explants containing different amounts of notochord. We were able to microsurgically create explants lacking the notochord as well as explants with two or more notochords. To make the explants without a notochord, we cut the notochord from the tissue along the midline of dorsal explants by hair-knives. Then the left and right half tissues healed together to form a single explant (**Figure 17**). To make the explants with two notochords, we recombined two half explants, each of which contained one notochord (**Figure 17**). To rule out the possibility that microsurgery changed the tissue stiffness, ‘sham-operated’ control explants were prepared by

splitting intact dorsal axial tissue near the midline axis and allowing the two parts to heal together. Sham control explants, explants with two-notochord and explants without notochord were still able to elongate at similar rates as intact control explants (**Figure 18A and B**). To further confirm the success of our microsurgeries and assess the tissue structure, we stained fibronectin fibrils, which locate at the boundaries of notochord and other major germ layers in dorsal isolates. Fibronectin outlined the architecture of these explants and showed our microsurgeries were successful.

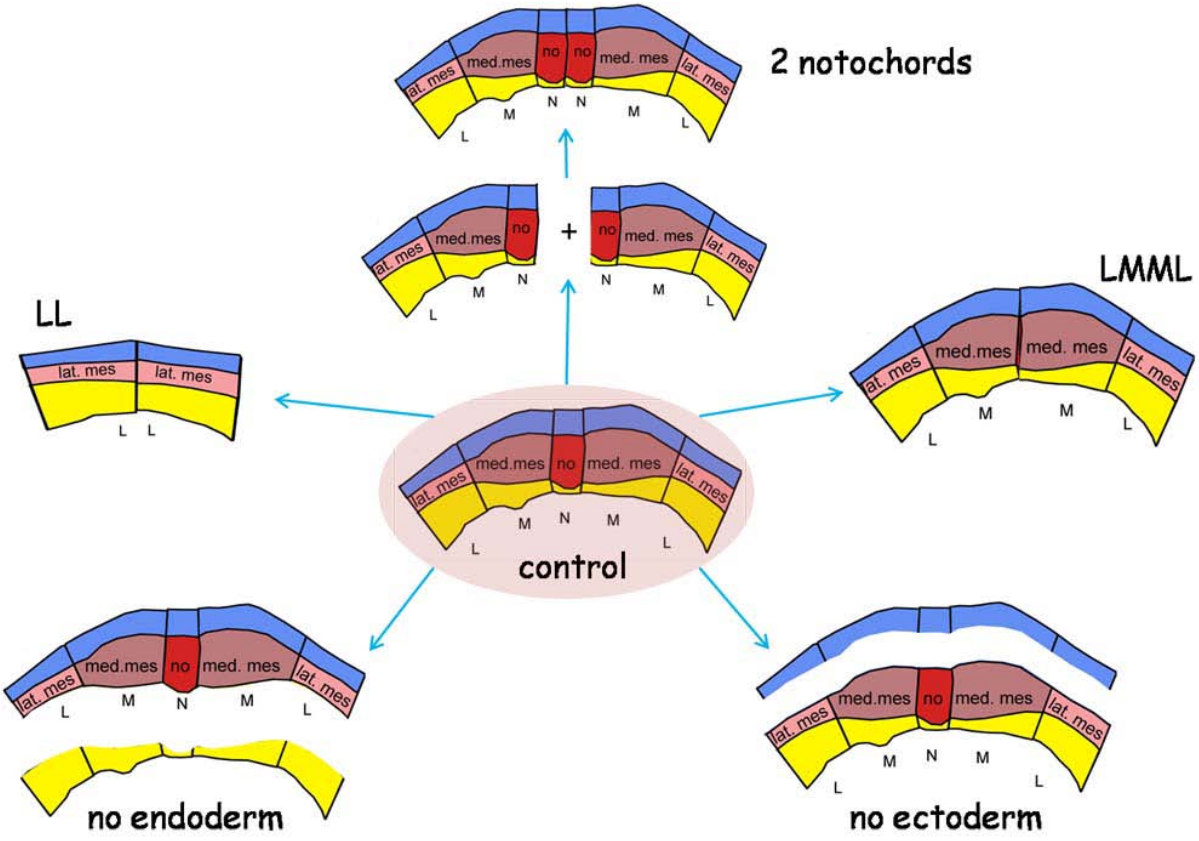

Figure 17. Microsurgically create explants containing various tissues.

Figure shows how to create explants with two notochords (2 notochords), explants only contain lateral mesoderm (LL), explants contain both lateral and medial mesoderm (LMML), explants without endoderm (no endoderm), and explants without neural plate (no ectoderm) from intact dorsal isolates (control).

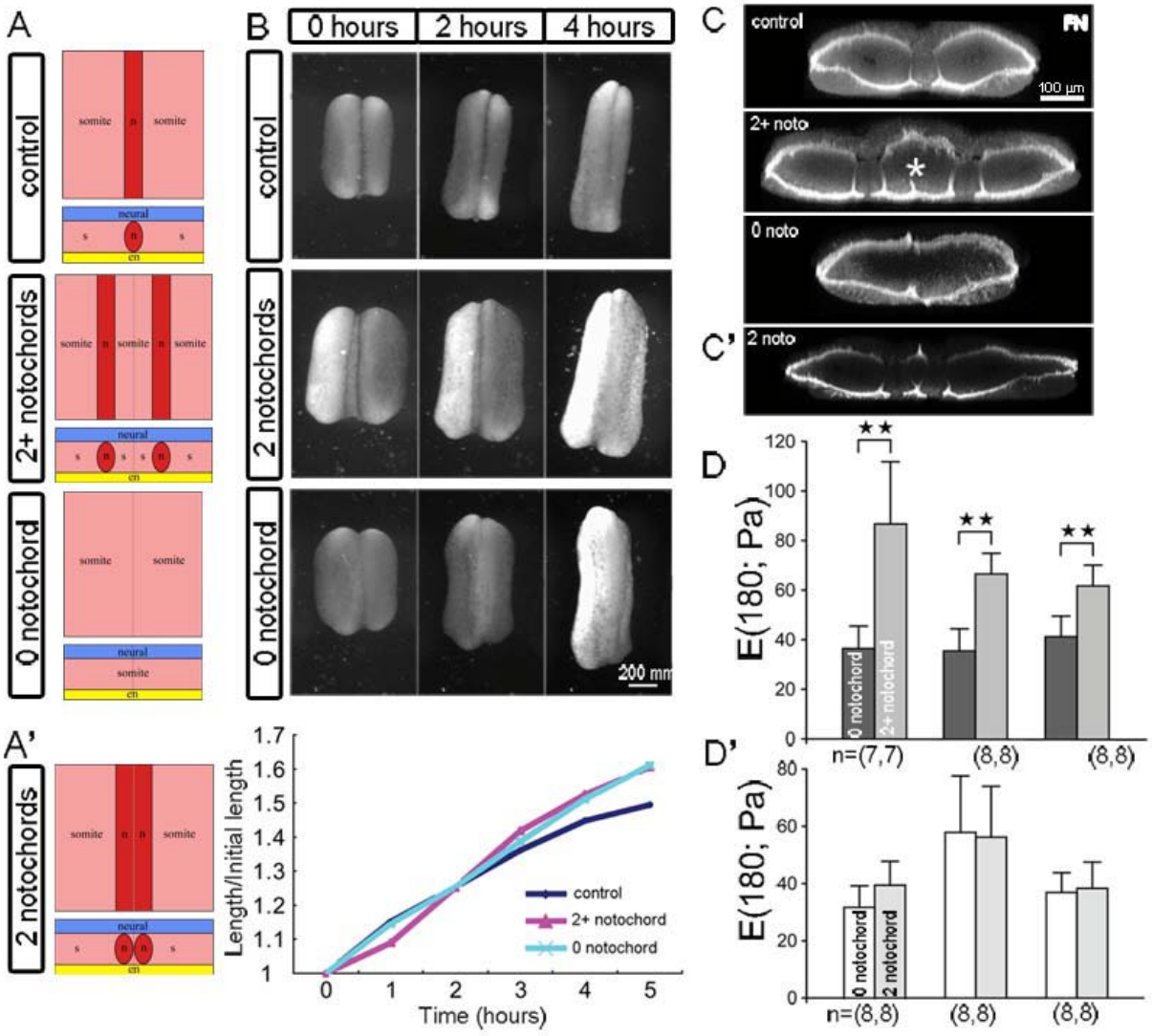

Figure 18. Mechanics of the notochord.

(A) Schematic of explants with various amount of notochord. (B) Explants with two-plus and zero-notochord elongate the same as control explants. (C) Maximum projection of confocal sections of fibronectin fibrils illustrates the transverse architecture of tested explants (note: dorsal is up). (D) The stiffness of explants with zero-notochord is compared to either the stiffness of explants with two-plus notochord or the stiffness of explants with two-notochord (D').

To determine the mechanical role of notochord, we first measured the stiffness of explants with different amount of notochord and found that ‘explants with two notochords’ (later we figured out that they were in fact explants with two-plus notochords) were at least two-fold stiffer than explants without notochord (or zero-notochord, **Figure 18D**). However, by closely checking the structures of these explants staining fibronectin fibril, we found that ‘explants with two notochords’ contained an extra fragment of notochord-adjacent medial paraxial mesoderm (**Figure 18C**), and we referred these explants as explants with “2+” (or “two-plus”) notochords. To make the explants which contain only two notochords, we again prepared two-notochord explants by using extra fine hair-knives which allow us to isolate the notochord at the precise boundary between the notochord and paraxial mesoderm. Subsequent fibronectin fibril staining confirmed that we completely removed the central fragment of paraxial mesoderm found in the “2+” notochords case. We referred these explants as explants with two notochords below (**Figure 18C**). In contrast to the results with “2+” notochords, we found no significant difference in the tissue stiffness between explants with two notochords and explants without notochord (**Figure 18D’**), which suggested that the notochord was not a major contributor to the tissue stiffness.

To confirm the surprising results, we used an alternative method to create explants containing extra notochord tissue by ruling out the effects of microsurgical recombination. The alternative strategy (**Figure 19A**) to increase the size of the notochord is to molecularly induce additional notochord tissue by treating explants with lithium chloride (LiCl), which is commonly used to alter the early patterning of embryonic cells and to dorsalize the embryos to generate larger field of notochord tissue (Kao et al., 1986). The degree of dorsalization was scored according to the Dorsal-Anterior Index (Stewart and Gerhart, 1990). By controlling the timing of 0.3 M LiCl treatment, we were able to consistently induce DAI 7/8 embryos (**Figure 19B**),

which contain doubled amounts of notochord tissue compared to control explants. The amount of the notochord was first estimated by using fibronectin fibril staining to outline the notochord boundary (**Figure 19D**) and was then confirmed by the gene expression of chordin (**Figure 19C**), a specific marker for notochord tissues, using RNA in situ hybridization. Both of the methods showed that dorsalized embryos contain almost two-fold larger notochord tissues (**Figure 19C and D**). Neither dorsalized embryos nor dorsal explants from these embryos could elongate as control embryos or explants (data not shown). We measured the stiffness of explants containing larger notochord tissue and found that there was no significant difference in tissue stiffness between dorsolized and control explants (**Figure 19E**), which confirms that notochord is not a major contributor to dorsal tissue stiffness in gastrula and neurula stage embryos.

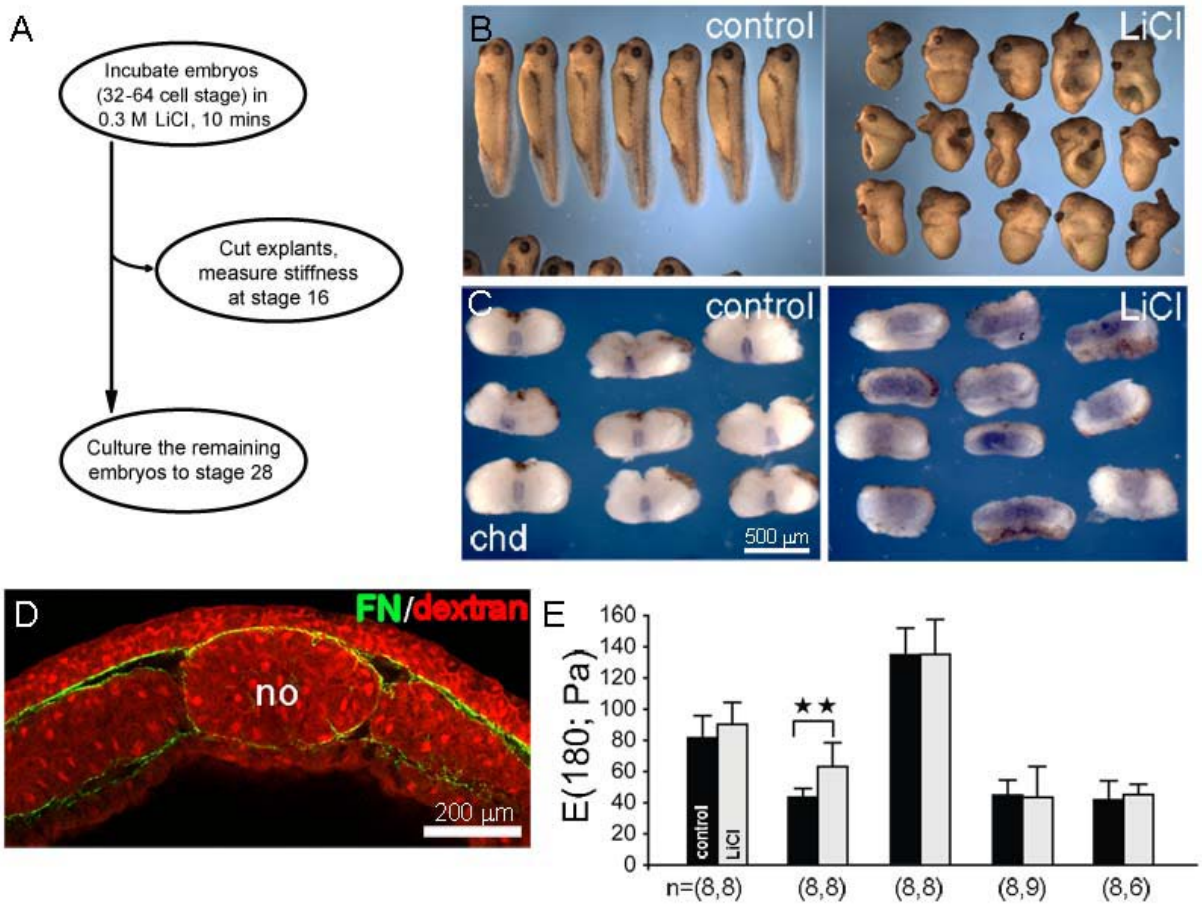

Figure 19. Confirmation of the mechanical contribution of notochord.

(A) LiCl generates super-large notochords in dorsal explants as shown in (B). (C) Chordin RNA in situ showing increased notochord within dorsal isolates made from DAI 7 to 8 embryos. (D) Transverse confocal section of a rhodamine dextran-labeled (red) and fibrillar fibronectin labeled (green) dorsalized embryo reveals enlarged notochord (no). (E) Comparison of stiffness of dorsal isolates with LiCl to dorsal isolates made from untreated control explants reveals no significant difference.

2.2.1.4 Paraxial mesoderm contributes to the stiffness of dorsal isolates

Since both physical and molecular methods revealed that notochord did not make significant contribution to tissue stiffness in late gastrulation, while explants with two-plus notochords were significantly stiffer than explants without notochords (**Figure 18D'**), we suspected that the paraxial somitic mesoderm might make a large contribution to the dorsal tissue stiffness. To directly test the contribution of paraxial somitic mesoderm to the tissue stiffness, we compared the stiffness of explants containing only lateral mesoderm (LL, Lateral-Lateral dorsal isolates) to explants containing only medial mesoderm (MM, Medial-Medial dorsal isolates). To make the LL and MM explants, we first used fine hair knives to remove the notochord from dorsal isolates at both the left and right notochord-somitic boundary, and then split the remaining two Lateral-Medial tissues (left side and right side of the dorsal isolates) into lateral and medial alone fragments. Last, we recombined the two lateral fragments to form LL and the two medial fragments to form MM explants (**Figure 16**). The structures of the LL and MM explants were confirmed by fibronectin fibril staining, which showed that MM explants had much thicker mesoderm, but much less endoderm tissues than LL explants (**Figure 20A and B**). The medial identity of MM explants were further confirmed by the expression of a prospective muscle marker XmyoD (Hopwood et al., 1989), which is only expressed in medial mesoderm, but not in lateral mesoderm (**Figure 20C**). The LL and LMML (containing both lateral and medial tissues) were still able to elongate at the similar rate as intact control dorsal isolates (**Figure 20D**). By measuring the stiffness of LL and MM explants, we found that the MM explants were significantly stiffer than LL explants (**Figure 20E**), which suggested that paraxial somitic mesoderm was much stiffer than other tissues in dorsal isolates.

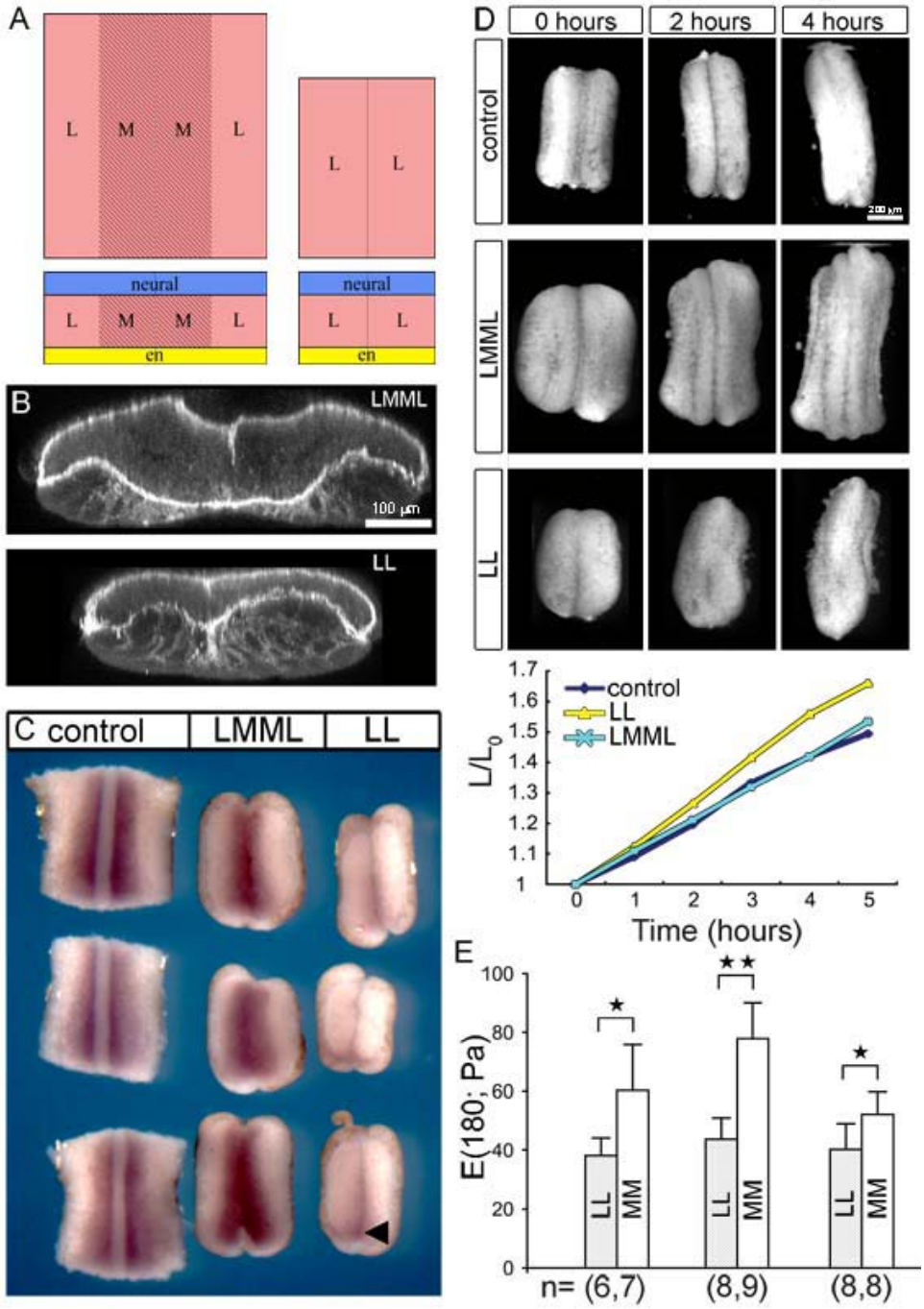

Figure 20. Mechanics of paraxial pre-somitic tissues.

(A) Schematic explants with paraxial tissues (LMML) and with only paraxial lateral tissues (LL). (B) Fibronectin staining of LMML and LL in transverse sections. (C) XmyoD expression in paraxial-medial (red). (D) LMML and LL elongate to the same degree as control explants. (E) MM explants are significantly stiffer than LL explants.

2.2.1.5 Different germ layers have different stiffness

Since germ layer cells demonstrate different cell behavior and possible different cellular mechanics (Keller et al., 2000a; Krieg et al., 2008), we strongly expected that the tissue mechanics may also be different. Furthermore, LL and MM explants contain not only different amounts of lateral and medial mesoderm, but also different amounts of neural and endoderm tissues (**Figure 21B**). To evaluate the contribution of neural and endoderm tissues to the stiffness of LL and MM explants, we also need to evaluate the stiffness of these tissues. Since each single germ layer is too thin to test using our nNFMD, we measured explants lacking one specific layer. To determine the mechanical contribution of the endoderm and neural plate layers, we measured the tissue stiffness of explants whose endoderm and neural plate is removed, respectively, and compared their stiffness to the intact control dorsal isolates. The architecture of the no-endoderm and no-neural-plate explants was confirmed by rhodamine dextran labeling, which labeled the cells and showed that these explants either lack endoderm or neural plate (**Figure 22A**). By comparing the no-neural-plate explants to control dorsal isolates, we found the stiffness of explants lacking a neural plate were not significantly different from control explants (**Figure 22B**). In a parallel set of experiments, we removed endoderm and compared the stiffness of no-endoderm explants to control dorsal isolates. We found that no-endoderm explants were significantly stiffer than control intact explants (**Figure 22C**), which suggested that endoderm was much more compliant than other tissues.

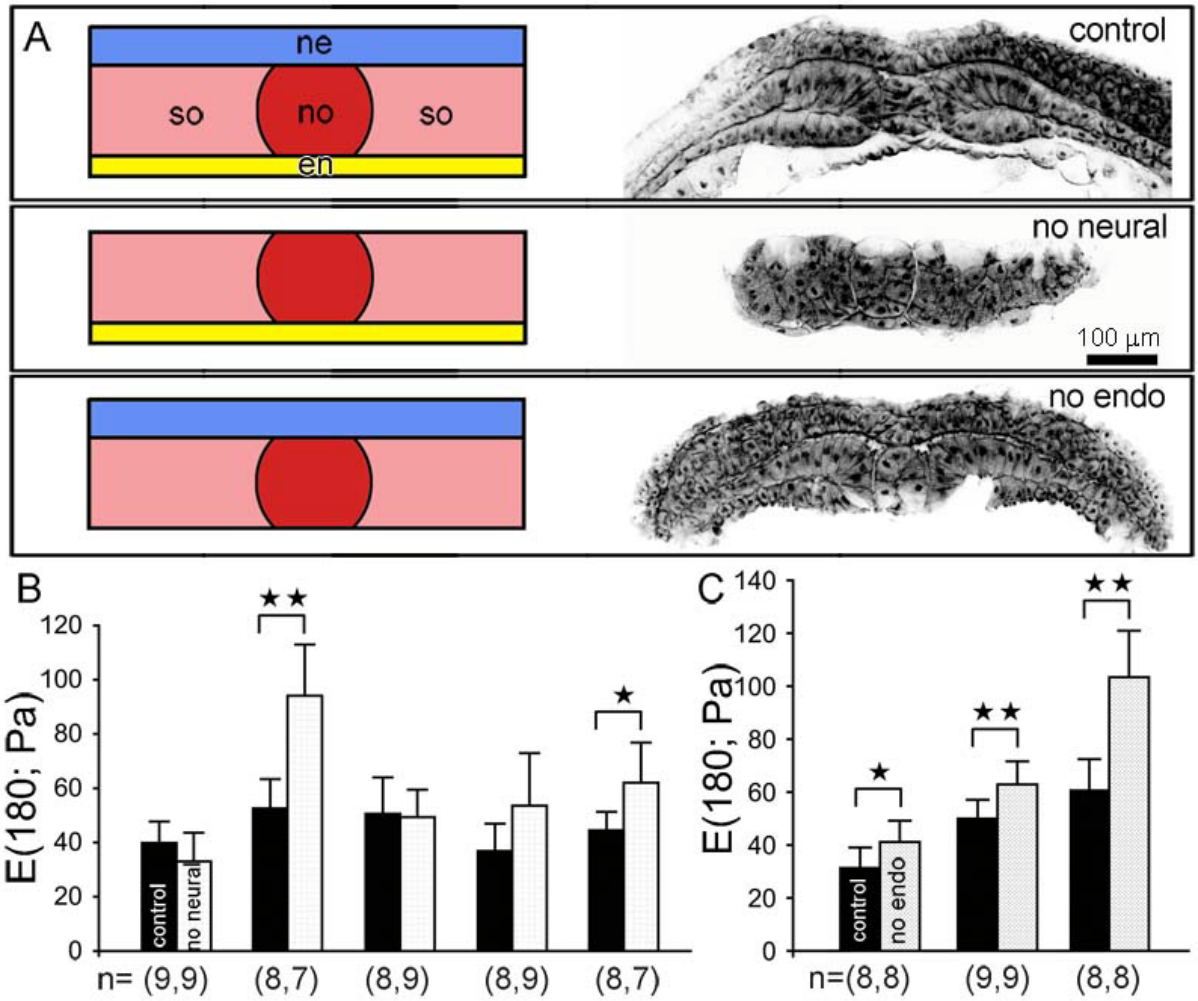

Figure 21. Contribution of endoderm and neural plate to dorsal tissue stiffness.

(A) Transverse sections of schematic (left) and rhodamine dextran-labeled explants (right) of no-endoderm and no-neural plate. (B) Explants without neural plate are not significantly different from control explants. (C) Explants without endoderm is much stiffer than control explants.

2.2.1.6 Composite model estimates the contributions of individual tissue components

Due to the design limitations of our current nano-Newton force measurement device, the uniaxial stress relaxation tests require samples to have regular shapes and to reach certain width and thickness. We could not test any individually isolated components such as notochord, endoderm and mesoderm alone, so we instead iteratively tested explants with one type of tissues removed. In the previous section, we qualitatively evaluated the stiffness of particular component by applying the following rules: if a soft tissue is removed, then the remaining explants would be stiffer; if a stiff tissue is removed, then the remaining explants would be softer; if a component which has similar stiffness to the mean value of others, then the remaining explants would be no change. In order to get more quantitative evaluation of the stiffness of each component, we applied a mechanical model which is based on superposition principles of composite structures (Christensen, 1991). In this model, each tissue is modeled as a spring and the total dorsal isolate is represented by the sum of parallel springs (**Figure 22B**). The total force (product of cross-section area and the elastic modulus) is evenly distributed on each component:

$$E_{DI}A_{DI} = E_{noto}A_{noto} + E_{somite}A_{somite} + E_{endo}A_{endo} + E_{ecto}A_{ecto} \quad \textbf{(2-10)}$$

where $\mathbf{E_{DI}}$ is the total stiffness of dorsal isolate, $\mathbf{A_{DI}}$ is the total area of the dorsal isolate, $\mathbf{E_{noto}}$, $\mathbf{E_{somite}}$, $\mathbf{E_{endo}}$ and $\mathbf{E_{ecto}}$ are the stiffness of notochord, somite, endoderm and ectoderm tissue, respectively. $\mathbf{A_{noto}}$, $\mathbf{A_{somite}}$, $\mathbf{A_{endo}}$ and $\mathbf{A_{ecto}}$ are the area of notochord, somite, endoderm and ectoderm tissue, respectively. Two examples are shown to estimate the stiffness of endoderm and notochord, respectively (**Figure 22C and D**). To estimate the $\mathbf{E_{endo}}$ (**Figure 22C**), we have:

$$E_{no.endo}A_{no.endo} = E_{DI}A_{DI} - E_{endo}A_{endo} \quad \textbf{(2-11)}$$

where $\mathbf{E_{no\cdot endo}}$ and $\mathbf{A_{no,endo}}$ are the stiffness and area of the explants without endoderm tissue, respectively. By rearranging the equation (2-11), we have:

$$E_{endo} = (E_{DI}A_{DI} - E_{no.endo}A_{no.endo}) / A_{endo} \quad \textbf{(2-12)}$$

Both $\mathbf{E_{DI}}$ and $\mathbf{E_{no.endo}}$ were directly measured in our experiments and the area of each tissue component in dorsal tissues was measured in fibronectin fibril stained confocal sections (**Figure 22A**).

With the both qualitative and semi-quantitative methods, we found that there was large spatial variation in tissue stiffness. We estimate that endoderm is the softest tissue with stiffness 2 to 11 Pa and ranges from 6 to 22% stiffness of the intact dorsal isolates. The paraxial mesoderm is the stiffest tissue with stiffness 70 to 140 Pa and typically ranges from 140 to 170% stiffness of the intact dorsal isolates. The notochord and neural plate lay between endoderm and mesoderm with stiffness 40 to 60 Pa, which is similar to the stiffness of intact dorsal isolates. More advanced devices, which could directly measure smaller or thinner fragments of dorsal tissues, are required to more accurately evaluate the spatial variation in tissue stiffness.

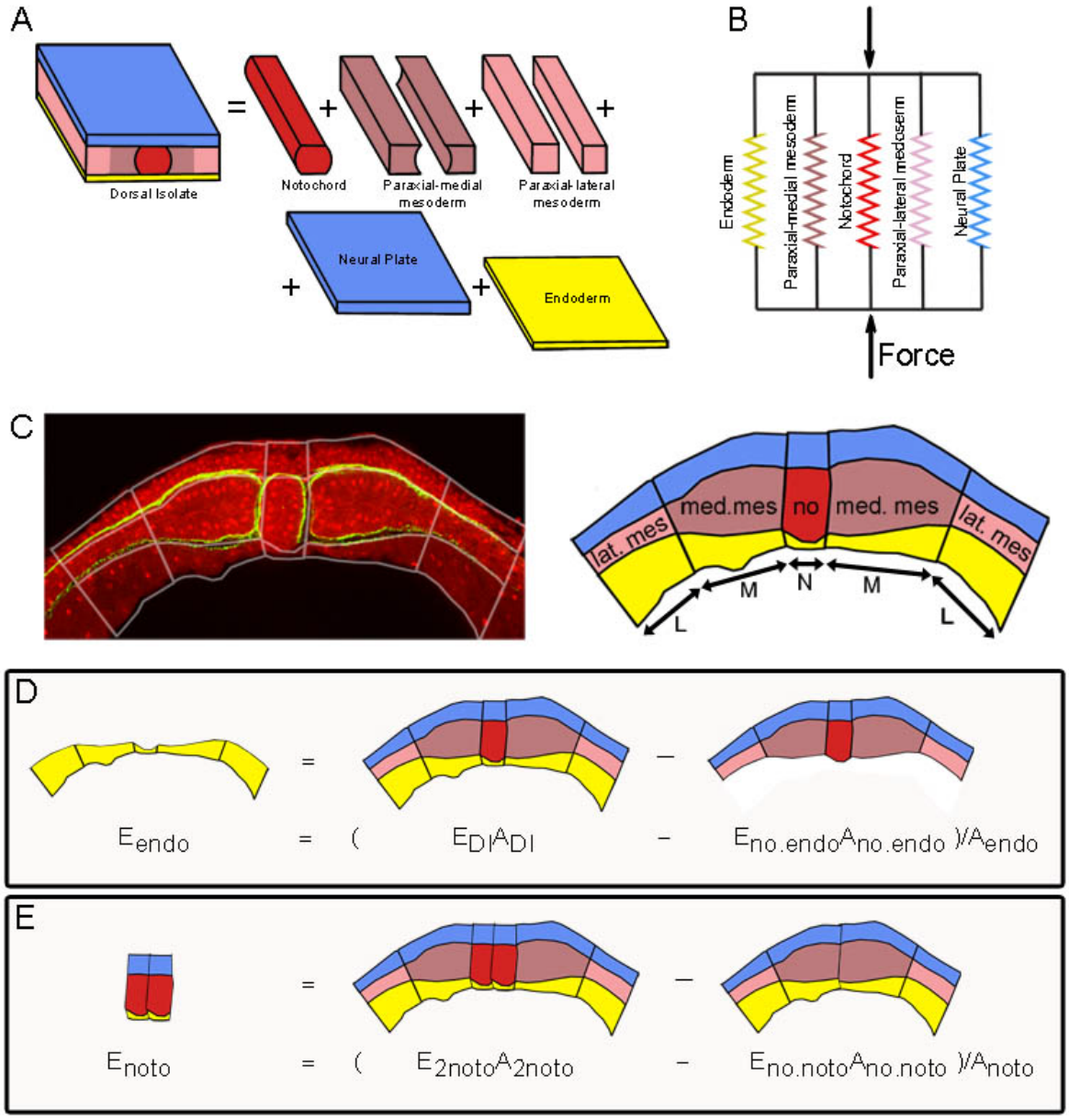

Figure 22. Quantitative evaluation of the stiffness of each component.

(A) The dorsal isolate is composed of notochord (no), paraxial-medial mesoderm (med.mes), paraxial-lateral mesoderm (lat.mes), neural plate and endoderm. (B) The relative area contributions of these five tissues are measured from transverse confocal optical sections from rhodamine-dextran-labeled cells (red) and fibronectin fibril-labeled tissue boundaries (green). The gray line overlay indicates the boundaries between these regions. The schematic on the right highlights the structural elements present in this confocal section. (C) Force applied on explants is distributed to each component. (D) Equations to estimate the stiffness of endoderm or notochord (E).

2.2.2 Evaluate the contribution of cellular structures to tissue stiffness

Cells, extracellular matrix, cell adhesions are the basic building blocks of dorsal tissues and their interactions are likely to determine the responses of tissues to external loads. In our working model, solid-like cells contribute to the stiffness of whole tissues; ECM mechanics affects the tissue stiffness; and cadherin-based cell-cell adhesion contributes to the tissue stiffness by working as “glue” to stick cells together. Since ECM and cadherin are inter-connected via the actomyosin network through integrin-based cell-ECM adhesion and cadherin-based cell-cell adhesion, they may also play important signaling roles in coordinating mechanical support. For example, fibronectin can modulate cadherin mediated adhesive activity through integrins (Marsden and DeSimone, 2003). Additionally, cell-cell and cell-ECM adhesion may be coupled together through a cortical actin network (Skoglund et al., 2008). Actomyosin is regulated by multiple pathways, such as PCP signaling, microtubule network and C-cadherin (Habas et al., 2003; Kwan and Kirschner, 2005; Tao et al., 2007). Both cell-cell and cell-matrix adhesion may regulate cytoskeletal effectors through Rho family GTPases (Arthur et al., 2002).

Upstream signaling pathways such as planar cell polarity (PCP) pathway may pattern the cellular stiffness and traction forces through cytoskeletal effectors to drive the tissue deformation, so it is important to study how the cytoskeletal effectors affect tissue stiffness. The studies are also an essential step to reveal the molecular mechanism underlying spatial and temporal variation present in tissue stiffness. In order to reveal the roles that cells, extracellular matrix, and cell adhesions play in determining tissue mechanics, we investigated the contribution of molecular and cellular structures to tissue stiffness by measuring the stiffness of dorsal isolates whose subcellular or cellular structures had been biochemically or molecularly modified. Live-cell imaging techniques or whole embryo histology were used to assess the specific effects of the

small molecule inhibitors or anti-sense treatment of cytoskeletal effectors such as actin, microtubules, and intermediate filaments, C-cadherin, or ECM such as fibronectin, laminin, and fibrillin.

2.2.2.1 Extracellular matrix does not contribute to the stiffness of dorsal isolates

ECM has been shown to dominate the mechanical properties of most adult tissues and to play a significant signaling role in convergent extension (Davidson et al., 2004; Davidson et al., 2006; Marsden and DeSimone, 2001; Skoglund et al., 2006; Skoglund and Keller, 2007). To determine the mechanical role of fibronectin in contributing to the tissue stiffness, we measured the stiffness of the dorsal tissues with reduced levels of fibronectin fibrils and compared their stiffness to that of control explants. To knock down the levels of fibronectin fibrils assembled in dorsal tissues, we injected one-cell stage embryos with a mix of two antisense morpholino oligonucleotides (FNMO, 6μM each embryo) directed against the 5' start of the two fibronectin pseudoalleles. Morpholinos are an antisense technology that works by blocking small sequences of RNA, so no protein is synthesized from the RNA. The reduction of fibronectin fibril levels in FNMO injected embryos was confirmed by staining the fibronectin fibrils with antibody 4H2 and comparing their expression levels to MO control explants, which were obtained from embryos injected with standard control morpholino (Gene Tools, LLC, Philomath, OR). The dose of FNMO used has been shown to reduce fibronectin synthesis and assembly, while allowing the injected embryos to gastrulate and develop through neurulation stages with a short dorsal trunk (Davidson et al., 2006).

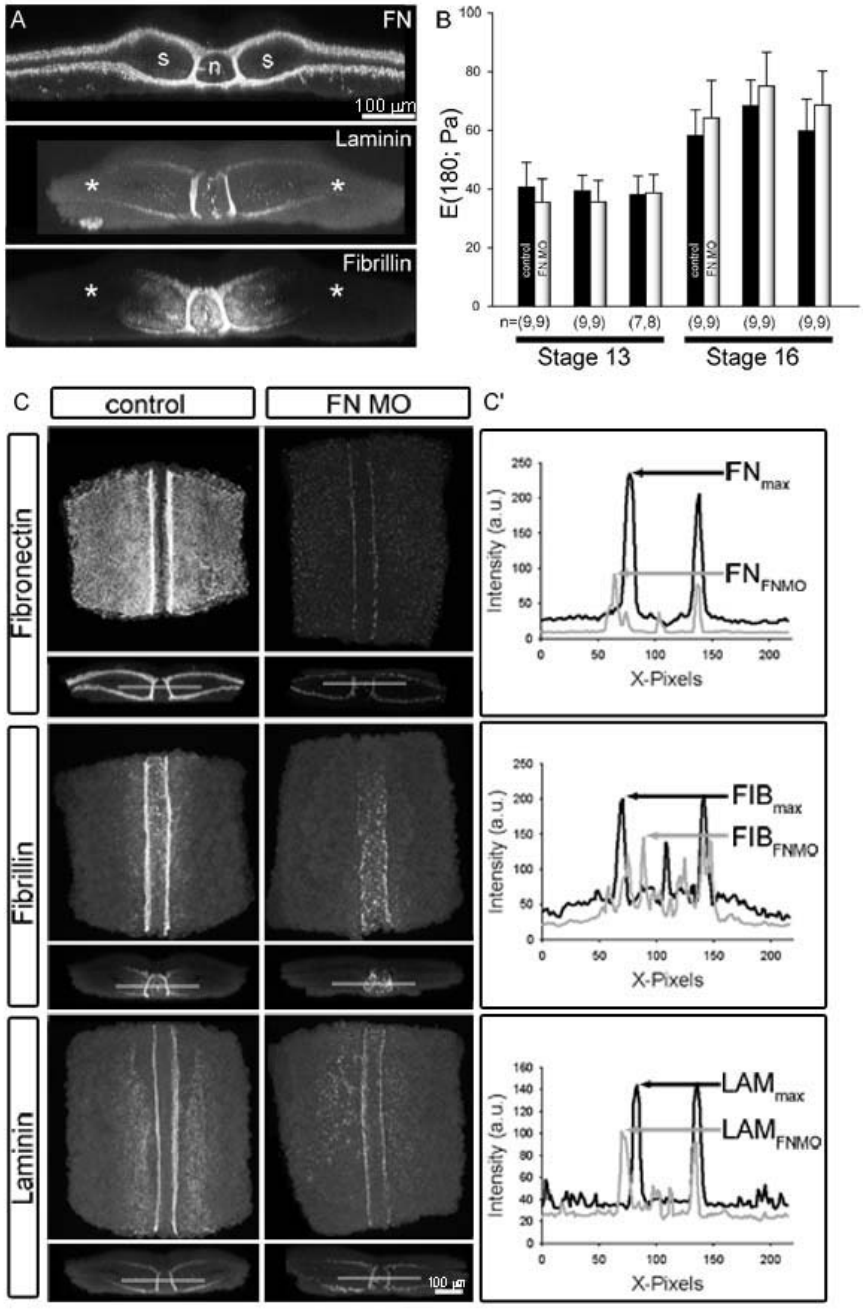

Figure 23. Role of ECM in tissue stiffness.

(A) Transverse sections of fibronectin (FN), laminin, and fibrillin (notochord, n; somitic mesoderm, s). (B) The stiffness of FNMO does not differ from uninjected explants at either stage 13 or at stage 16. (C) Maximum projections and intensity profiles (C') of FNMO show severe reduction in fibronectin fibrils and defects in assembly of fibrillin and laminin compared with control explants sectioned with identical confocal settings. Intensity profiles collected mediolaterally across the midline (transparent line in C).

There are three types of ECM assembled in *Xenopus* embryos during late gastrulation and early neurulation. Transverse sections of fibronectin (FN), laminin (LAM), and fibrillin (FIB) showed that FN surrounded both notochord, paraxial-medial, and paraxial-lateral mesoderm, while LAM and FIB were only beginning to be assembled around notochord and paraxial-medial mesoderm (**Figure 23A**). Maximum projections of FN, LAM, and FIB of FNMO-injected dorsal isolates demonstrated that injecting FNMO not only reduced the level of fibronetin assembly, but also decreased the levels of fibrillin and laminin in comparison to uninjected control explants sectioned with identical confocal settings (**Figure 23C**). To quantitate the reduction of the matrix, intensity profiles were collected mediolaterally across the midline of notochord and paraxial-medial mesoderm (**Figure 23C**). We found that injecting FNMO reduced the level of fibrillar fibronetin by 60%, fibrillin by 22% and laminin by 29% (**Figure 23C'**).

However, reducing the level of ECM did not change the tissue stiffness in late gastrula dorsal tissues (stage 13, **Figure 23B**). To confirm the surprising results, we compared the stiffness between control and FNMO-injected explants in stage 16 embryos, which belong to early neurulation stages and contain more assembled FN. Again, we did not find any significant difference between control and FNMO-injected dorsal isolates in stage 16 dorsal isolates (**Figure 23B**). From these tests we conclude that ECM is not a major contributor to the stiffness of early embryonic tissues. This result might have been expected since medial tissues such as notochord, which contains the bulk of ECM accumulatd at these stages, does not contribute strongly to the tissue stiffness (see **Section 2.2.1.3**).

2.2.2.2 Role of Cadherin in regulating the stiffness of dorsal isolates

C-cadherin is the major cadherin type in *Xenopus* embryos during late gastrulation and early neurulation and is essential to maintain tissue integrity either by directly connecting cells or by indirectly regulating the cortical actin cytoskeleton through p120 catenin (Tao et al., 2007). Mutant cadherin proteins containing only Catenin-Binding Region (CBR) showed a decrease in the cell-cell adhesion and even caused cell dissociation at high levels (Espeseth et al., 1998; Kintner, 1992; Riehl et al., 1996). The challenge of studying C-cadherin is that both dominant negative mutant and overexpression of C-cadherin disrupt convergent extension at very early stages (Lee and Gumbiner, 1995). To overcome this early lethal effect, we developed a hormone inducible system which fuses CBR to a ligand binding domain of the human glucocorticoid receptor (CBR-GR). The fusion protein keeps the dominant negative cadherin in an inactive state by complex formation with hsp90 and can be rapidly activated by dissociation of hsp90 induced by dexamethasone (DEX) (Kolm and Sive, 1995; Scherrer et al., 1993; Tsai and O'Malley, 1994; Wheeler et al., 2000). Theoretically, this technique could allow us to inject inactive dominant negative cadherin into embryos at one cell stage and activate the mutant construct at later stages by adding DEX.

We injected CBR-GR in one-cell stage embryos, added DEX at stage 13, and measured the stiffness of dorsal isolates from the injected embryos at stage 16. We found that CBR-GR injected dorsal isolates were less stiff than control uninjected explants (8 treated and 8 control explants from one clutch, **Appendix A**). However, we only detected the reduction in tissue stiffness of treated explants in one single case. In most clutches, the same doses of CBR-GR could not induce similar phenotype in frog embryos. The reason for the unstable effects of CBR-GR may be because the construct could not disrupt enough C-cadherin since it was initially

designed to change the levels of transcription factors, but not structure proteins like cadherin, which are present in higher amounts in cells than transcription factors. We also found that CBR-GR produced similar phenotypes of embryos in the absence of DEX (**Figure 24**), which suggested that the GR domain may be "leaky" and allow function of the CBR even without DEX. Continued efforts are needed to refine this technique or to adapt new methods to acutely control cell-cell adhesion.

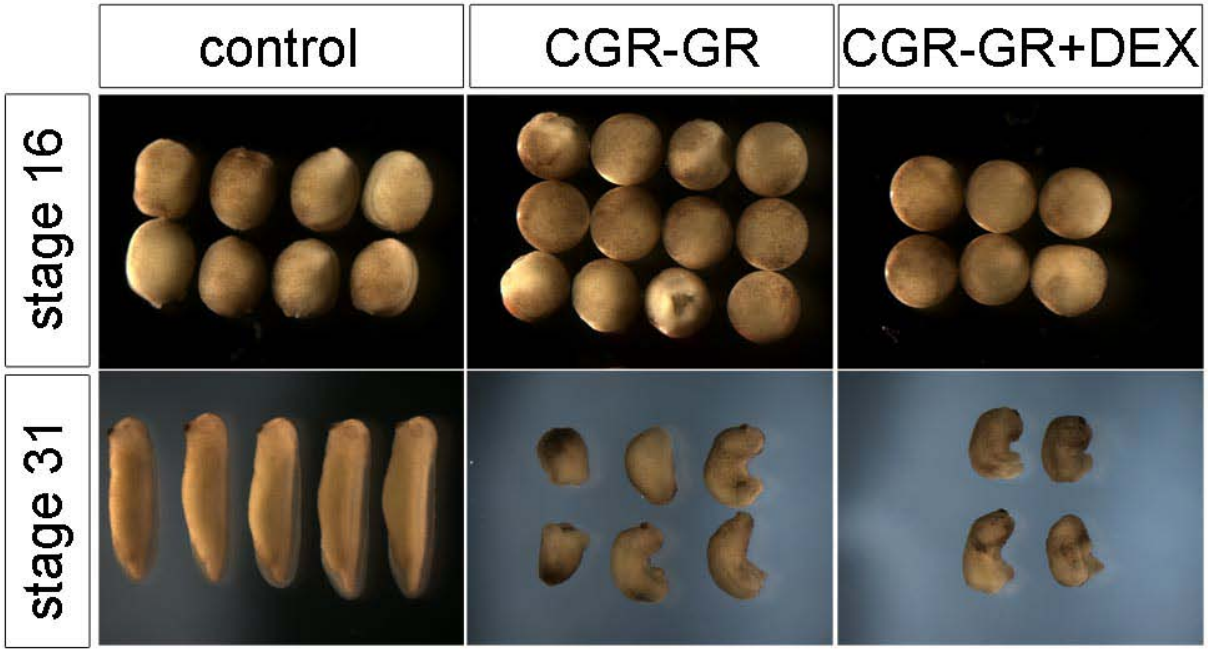

Figure 24. Effects of CBR-GR on embryos.

2.2.3 The contribution of the cytoskeleton to tissue stiffness

It is postulated that the tissue stiffness is largely dependent on the stiffness of individual constituent cells (Gibson and Ashby, 1988; Gibson and Ashby, 1997). Furthermore, cadherin-mediated cellular adhesive force has been shown to be much larger than the force needed to

deform the individual cells, which indicates that the stiffness at tissue level mainly represents the stiffness of individual cells (Keller et al., 2003; Moore et al., 1995). The mechanical properties of the cells are regulated by structural networks such as actin cytoskeleton (Elson.,1988), actomyosin contractility (Martens and Radmacher, 2008), microtubule (Rodriguez et al., 2003), intermediate filaments (Wang and Stamenovic, 2000), and associated proteins. Many signaling pathways, such as the PCP pathway, are thought to pattern the tissue mechanics by modulating the cytoskeletal effectors through small GTPase molecules such as Rho, Rac and cdc42 (Habas et al., 2003; Tahinci and Symes, 2003). To investigate the contribution of cytoskeletal proteins to the stiffness of dorsal isolates, we altered the subcellular structures using acutely acting inhibitors and studied the dosage-response of stiffness to these inhibitors.

2.2.3.1 Actin cytoskeleton dominates the stiffness of dorsal isolates

As the mechanical properties of both living cells and early blastula embryos are dominated by the actin cytoskeleton (Ananthakrishnan et al., 2006; Valentine et al., 2005; Wakatsuki et al., 2001), we first tested the role of F-actin in determining tissue mechanics. To evaluate the contribution of F-actin to tissue stiffness, we measured the stiffness of dorsal tissues whose actin cytoskeleton network was decreased by incubating 20 minutes in 0.3, 0.6, and 1.2 μM latrunculin B (LatB), which depolymerizes F-actin and has previously been shown to decrease the cell stiffness *in vitro* (Wakatsuki et al., 2001). We found that 20-minute LatB treatment decreased tissue stiffness up to 70% in a dose-dependent manner demonstrated by the ratio between the stiffness of treated explants and that of control explants (**Figure 25**). The results suggested that F-actin regulated the tissue stiffness in embryonic tissues. Although an alternative explanation to the results would be that disruption of actin cytoskeleton reduces the tissue stiffness by

decreasing the assembly of ECM (Davidson et al., 2008). However, since our previous results indicated that reducing fibronectin fibrils did not change the tissue stiffness, we concluded that it was reduced levels of F-actin, but not fibronectin fibrils that reduced tissue stiffness.

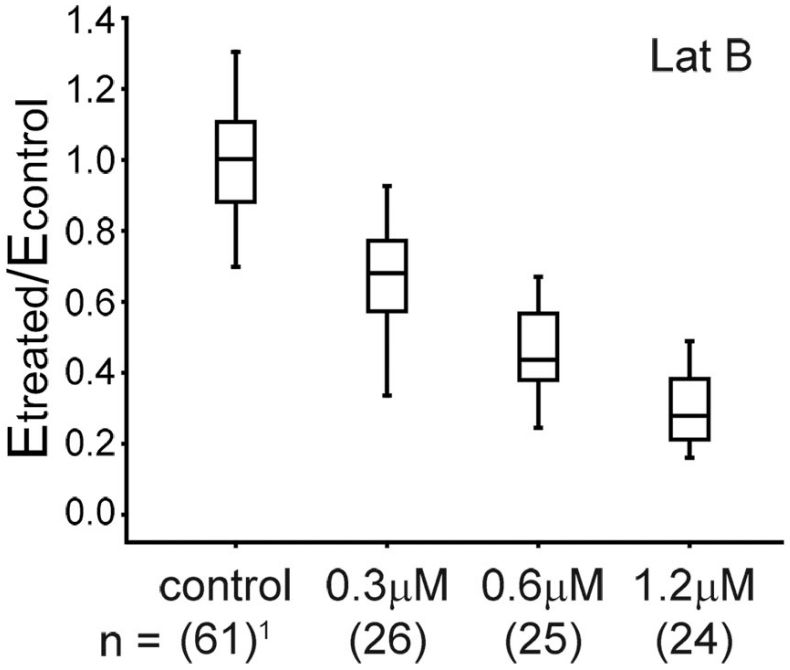

Figure 25. Treatment of explants with latB reduced tissue stiffness in a dose-dependent manner.

To test the reversibility of LatB treatment on dorsal isolates, we repeatedly measured the stiffness of the same tissue before treatment (E_0), immediately after 20 minutes 0.6μM LatB treatment, and every half hour in next three hours after LatB was washed out. We found that the stiffness of the dorsal isolates did not fully recover after LatB treatment (**Figure 26A**) which suggested that, when dorsal isolates were treated with LatB, the treatment on tissue stiffness was not reversible.

Since LatB treatment on actin assembly and actin dymanics was found to be reversible in whole embryos (Personal communication with Hye Young Kim), we tested the reversibility of LatB treatment on tissue stiffness in whole embryos by comparing the stiffness of dorsal isolates

between control and LatB-treated embryos after LatB was washed out. We found that there was no significant difference in the stiffness between control explants and explants cut from embryos, who were transiently treated with LatB for 20 minutes and allowed to recover for 1, 4, and 6 hours (**Figure 26B**). The results suggested that, when whole embryos were treated with LatB, the treatment was reversible. The live imaging of F-actin confirmed that the LatB treatment on actin network was irreversible when LatB was applied to dorsal explants, but was reversible when LatB was applied to whole embryos (work by Hey Young Kim). It is not clear what factors are responsible for the discrepancy of reversibility between tissues and embryos.

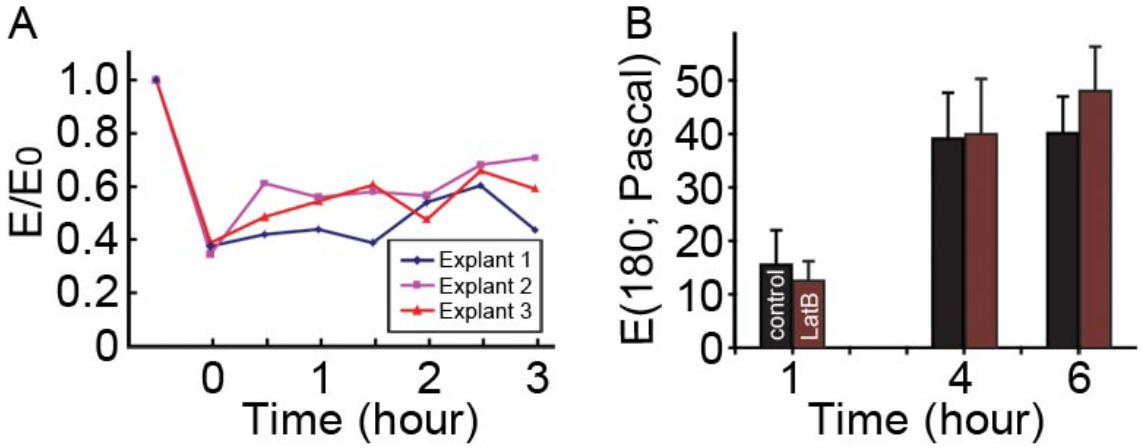

Figure 26. Recovery of LatB treatment.

(A) Tissue stiffness did not recover when LatB treated on isolated dorsal isolates demonstrated by the ratio of tissue stiffness before and after LatB treatment. (B) Tissue stiffness recovered when LatB treated on whole embryos (8 control and 8 treated explants for each measurement, all explants from single clutch embryos).

Since reduction in F-actin decreased tissue stiffness, we suspected that increase in F-actin would increase tissue stiffness. In order to elevate the F-actin density, we treated dorsal tissues with Jasplakinolide, which is a potent inducer of actin polymerization and has been demonstrated to stabilize actin filaments (Bubb et al., 1994; Bubb et al., 2000). However, by testing 33 treated

and 34 control untreated explants from 4 clutch embryos, we found that polymerization of actin cytoskeleton by 1-3 μM Jasplakinolide for 60 minutes did not increase the tissue stiffness and may decrease the stiffness at very high concentration (10 μM for 40 minutes, **Appendix A**). Interestingly, combined treatment of Jasplakinolide and LatB showed that Jasplakinolide increased the stiffness of dorsal isolates, whose actin cytoskeleton was first decreased by LatB (8 explants treated with LatB alone, 9 explants treated with Jasplakinolide and LatB, all explants from one clutch embryos, **Appendix A**).

2.2.3.2 Myosin II contractility regulates the stiffness of dorsal isolates

Since myosin II contractility plays a key role in cell mechanics (Nagayama et al., 2004; Stamenovic, 2005a) and is thought to regulate the convergent extension movements and neural tube closure (Rolo et al., 2009; Skoglund et al., 2008), we tested the role of myosin II contractility in tissue mechanics by comparing the stiffness of control explants to the dorsal isolates treated with 60 minutes Y27632. Y27632 inhibits myosin II contractility by inhibiting Rho kinase (ROCK) through phosphorylation of regulatory light chains (Uehata et al., 1997). We found that treatment of tissues with Y27632 reduced tissue stiffness in a dose-dependent manner (**Figure 27C**), which suggested that myosin II contractility regulated the tissue stiffness. Interestingly, although Y27632 reduced tissue stiffness up to 50%, the treated dorsal isolates were still able to elongate at the same rates as control explants. Moreover, we did not detect any defects in Y27632-treated embryos until very late stages (**Figure 27A and B**), which suggested that reducing the tissue stiffness by Y27632 did not disrupt the morphogenetic movements of early embryos.

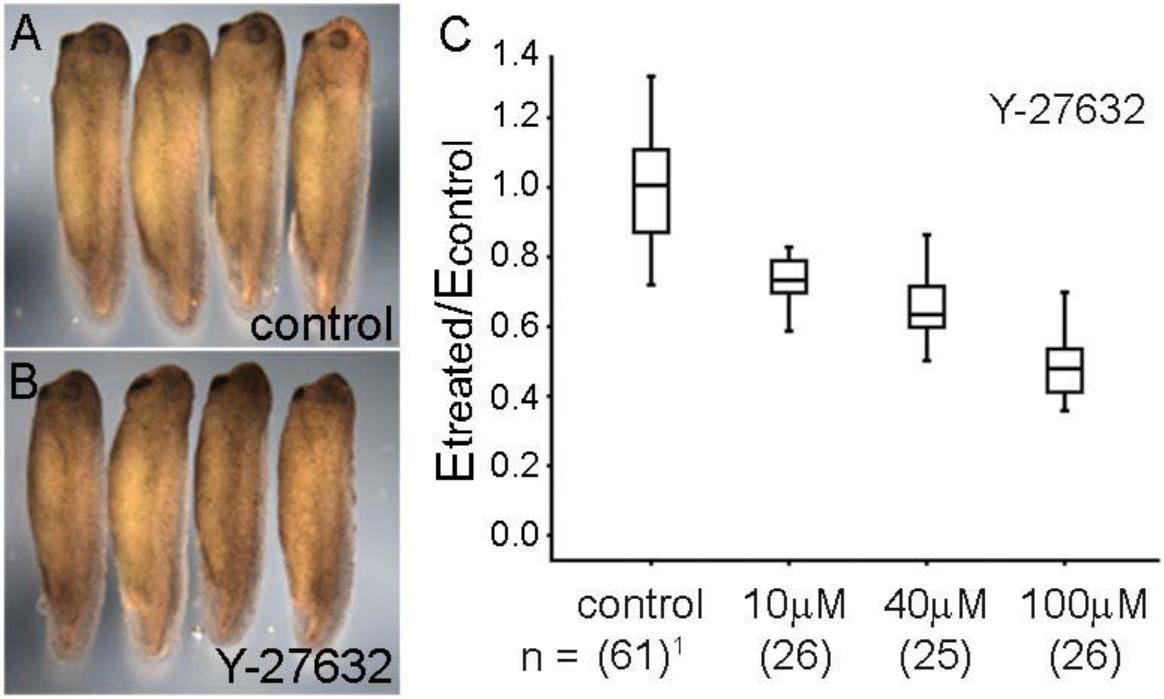

Figure 27. Contribution of myosin II contractility to tissue stiffness.

(A) Control untreated embryos and embryos treated with Y27632 since late gastrula (B) showed that Y27632 did not affect morphogenetic movements. (C) Y27632 reduced tissue stiffness in a dose-dependent manner.

Since decreasing actin cytoskeleton or myosin II contractility by LatB and Y27632, respectively, both reduced tissue stiffness, we then tested which component dominated the tissue mechanics. By combining the treatment of LatB and Y27632 together, we found that LatB further significantly decreased the stiffness of Y27632 pre-treated dorsal tissues, while Y27632 only slightly reduced the stiffness of LatB pre-treated tissues (**Figure 28**). The results suggested that actin cytoskeleton dominated the tissue stiffness and that an intact F-actin network was a pre-requisite for myosin function.

Since reduction in myosin II contractility decreased tissue stiffness, we suspected that we could increase the tissue stiffness by increasing myosin II contractility. However, treatment of dorsal isolates with 20-30 minutes 40 nM calyculin A, which activates the myosin II contractility

by inhibiting myosin light chain phosphatase (Ishihara et al., 1989), failed to increase the tissue stiffness (9 treated explants and 8 control untreated explants from one clutch embryos, **Appendix A**). Again, combined treatment of calyculin A and Y27632 showed that calyculin A slightly increased the stiffness of dorsal isolates, whose myosin II contractility was first decreased by Y27632 (18 explants treated with Y27632 alone, 18 explants treated with calyculin A and Y27632, explants from two clutch embryos, **Appendix A**).

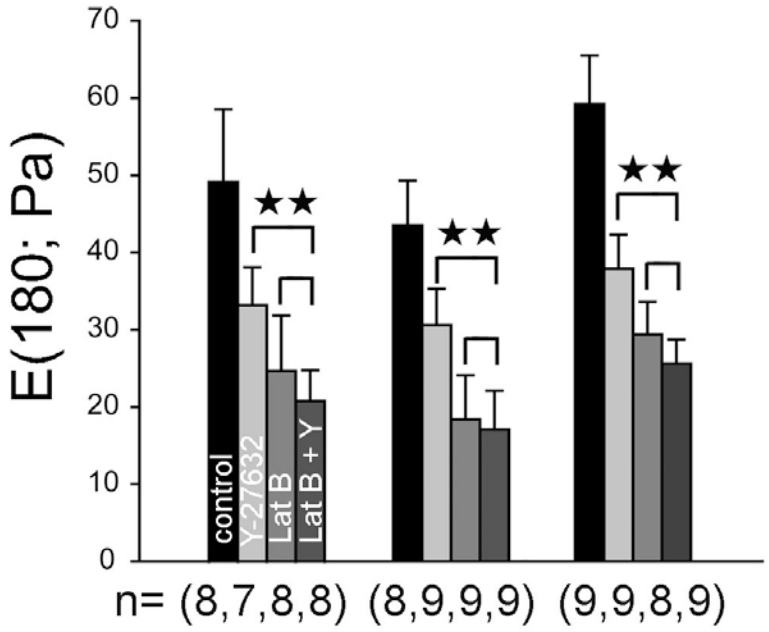

Figure 28. Actin cytoskeleton dominated the tissue stiffness.

2.2.3.3 <u>Depolymerizing microtubules increases the stiffness of dorsal isolates</u>

Microtubules have been shown to regulate the convergent extension in *Xenopus* embryos (Kwan and Kirschner, 2005; Lane and Keller, 1997), but their role in determining cellular mechanics is still not clear (Stamenovic, 2005b), so we decided to test the affects of microtubules on tissue

mechanics. To investigate the contribution of microtubules to the tissue stiffness, we measured the stiffness of dorsal isolates treated with 40 minutes 50 μM nocodazole, which depolymerize the microtubules (Keller et al., 1984; Tomasek and Hay, 1984), and compared their stiffness to that of control explants. It was very surprising that dorsal isolates treated with nocodazole dramatically increased stiffness up to 2 to 3 folds (**Figure 29A**). However, we found that taxol, which stabilizes the microtubules (Danowski, 1989; Schiff and Horwitz, 1980), did not significantly change the tissue stiffness (**Figure 29B**).

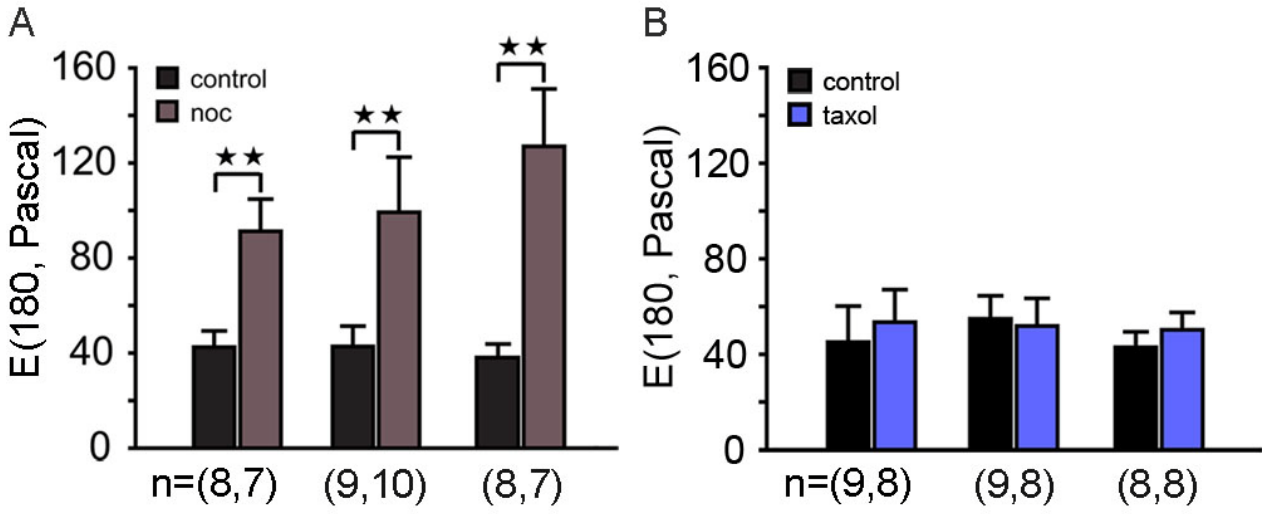

Figure 29. Contribution of microtubules to tissue stiffness.

(A) Depolymerizing microtubules with 50 μM nocodazole (noc) dramatically increased tissue stiffness. (B) Stabilizing microtubules with 23 μM taxol did not significantly change tissue stiffness.

2.2.4 Mechanism underlying the regulation of actomyosin contractility by microtubules

Previous studies have shown that disruption of microtubules increased the actin assembly and myosin II contractility (Danowski, 1989; Enomoto, 1996). However, there are at least two models proposed to explain how microtubules and actomyosin contractility interact (Danowski, 1989). Disruption of microtubules may increase the actomyosin contractility through a mechanical model (Wang et al., 2001) or through factors bound to microtubules (Danowski, 1989).

2.2.4.1 GEF-H1 is necessary to increase tissue stiffness

To determine the mechanism underlying nocodazole-mediated increase in tissue stiffness, we first molecularly de-coupled signaling from the microtubules to actomyosin network by blocking the function of Xlfc, which is a *Xenopus laevis* homolog to Rho GEF-H1 and a molecular linker between microtubules and actomyosin network (Krendel et al., 2002). Xlfc contains a C1/zinc-binding region, a Dbl-homology domain, a pleckstrin-homology domain, and a coiled-coil region (Kwan and Kirschner, 2005). The C1/zinc-binding region and the Dbl-homology domain are responsible for binding the microtubule and for exchanging guanine nucleotide to activate Rho-family GTPases, respectively (Krendel et al., 2002; Kwan and Kirschner, 2005). Xlfc had already been cloned to study its role in gastrulation. Anti-sense Xlfc morpholinos (Xlfc-MO) has been demonstrated to knock-down Xlfc in *Xenopus* (Kwan and Kirschner, 2005). We found that Xlfc-MO completely blocked nocodazole-induced stiffening (**Figure 30A**), suggesting that the tissue-scale mechanical consequences of nocodazole are due to signaling rather than the mechanical properties of microtubules. Decreasing the levels of Xlfc by injecting Xlfc-MO did

not change the tissue stiffness as demonstrated by comparing the stiffness between Xlfc-MO injected and control morpholino injected dorsal isolates (**Figure 30B**).

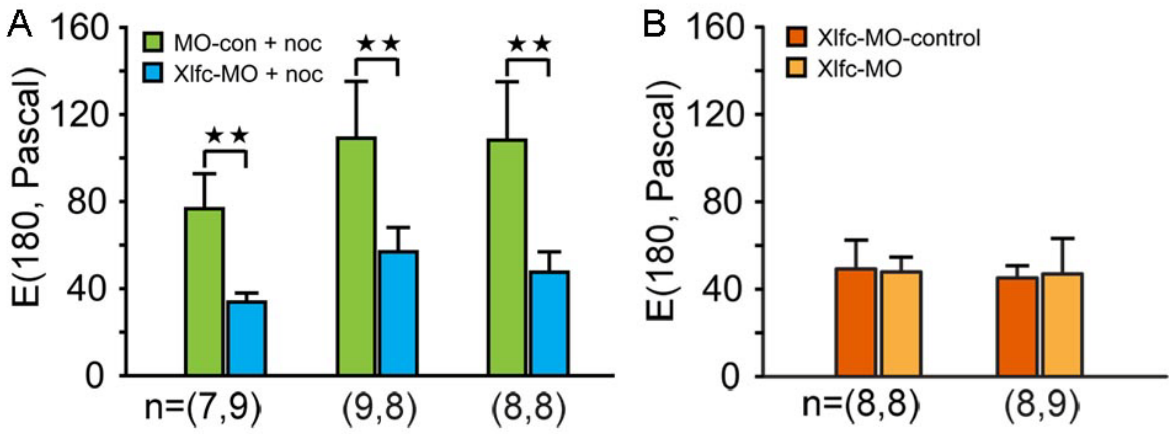

Figure 30. GEF-H1 is necessary to increase tissue stiffness.

(A) Xlfc morpholinos (Xlfc-MO) blocked nocodazole-induced tissue stiffening. (B) Xlfc-MO itself had no effects on tissue stiffness.

2.2.4.2 GEF-H1 is sufficient to increase tissue stiffness

To test whether Xlfc is sufficient to increase tissue stiffness, we compared the tissue stiffness between control explants and dorsal isolates injected with C55R, which is a constitutively active form of Xlfc lacking the nucleotide exchange activity due to a mutation in C1/zinc-binding region (Kwan and Kirschner, 2005). It is difficult to isolate dorsal isolates from high doses (250 pg C55R mRNA per embryo) of C55R injected embryos, which showed severe gastrulation defects, so we reduced the amount of C55R mRNA to 175 pg per embryo to allow us to reliably obtain dorsal isolates from embryos with less severe defects (**Figure 31A**). We found that C55R injected dorsal isolates were 2- to 3-fold stiffer than control un-injected explants in absence of nocodazole (**Figure 31B**), which suggested that Xlfc was sufficient to increase tissue stiffness.

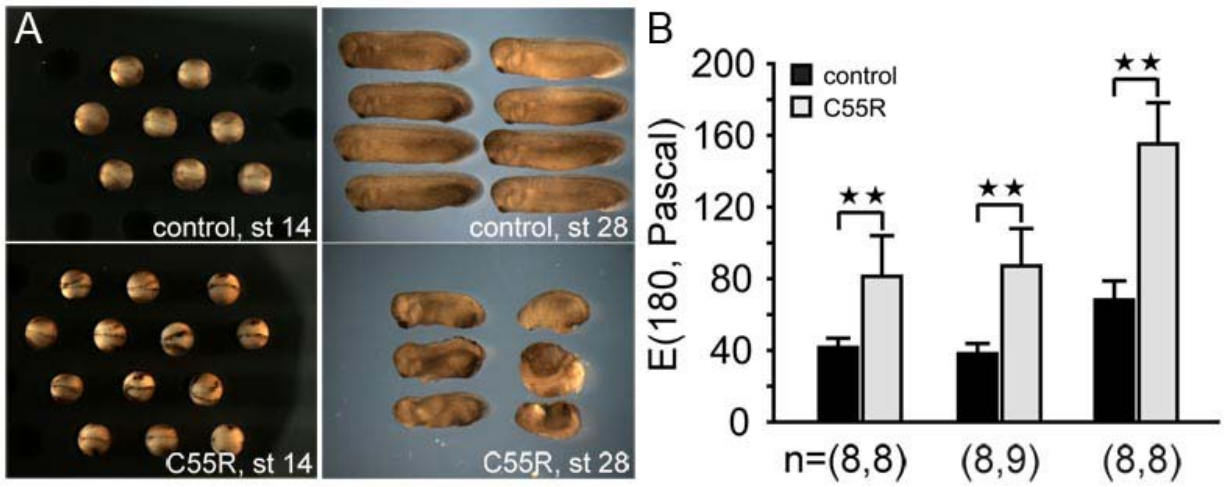

Figure 31. GEF-H1 is sufficient to increase tissue stiffness.

(A) Low-dose C55R induced minor defects. (B) C55R significantly increased the tissue stiffness in the absence of nocodazole.

2.2.4.3 Microtubules do not mechanically contribute to tissue stiffness

While Xlfc mediates nocodazole-induced tissue stiffening, it is still unknown whether microtubules mechanically contribute to the tissue stiffness, since microtubules could both mechanically and molecularly regulate the tissue stiffness. To determine the mechanical role of microtubules, we tested the effects of nocodazole on dorsal isolates whose Xlfc function was completely blocked by Xlfe-MO. We found that nocodazole did not increase the stiffness of Xlfc-MO injected tissues (**Figure 32**), which demonstrates that depolymerization of microtubules alone does not change tissue stiffness. Therefore, the mechanical consequences of nocodazole are not due to the mechanical function of microtubules, but to their role in sequestering a signaling factor, Rho GEF-H1.

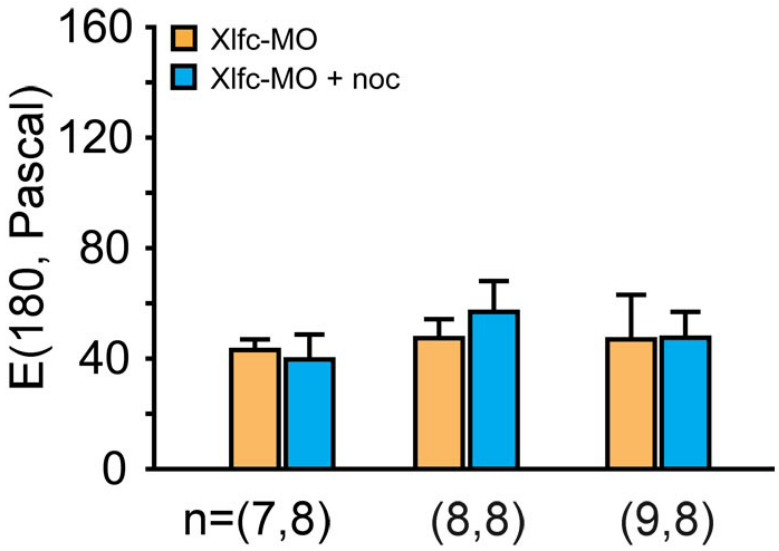

Figure 32. Disruption of microtubules did not increase tissue stiffness in Xlfc-MO injected embryos.

2.2.4.4 Rho-GEF regulates tissue stiffness through myosin II contractility

RhoGTPase could regulate actomyosin contractility through several pathways, such as altering actin polymerization, bundling of actin filaments, or myosin II contractility (Machesky and Hall, 1997; Millard et al., 2004; Somlyo and Somlyo, 2000; Watanabe et al., 1999). To determine how Rho-GEF modulates the tissue mechanics, we compared the stiffness of tissues treated with nocodazole alone to tissues treated with nocodazole and Y27632, which has been shown to block the myosin II contractility in cultured cells (Nagayama et al., 2004; Uehata et al., 1997) and reduced the tissue stiffness (**Section 2.2.3.2**). We found that tissues treated with both nocodazole and Y27632 had similar stiffness as control untreated tissues and were significantly less stiff than

tissues treated with nocodazole alone (**Figure 33**). While this result suggests that GEF-H1 increases tissue stiffness through myosin II contractility, we also found that tissues treated with nocodazole and Y27632 were slightly, but significantly stiffer than tissues treated with Y27632 alone (**Figure 33**). This suggests that blocking myosin II contractility could not completely inhibit the tissue stiffening caused by nocodazole. Additionally, we found that tissues treated with nocodazole alone were significantly stiffer than tissues treated with nocodazole and LatB (8 explants treated with nocodazole alone, 7 explants treated with nocodazole and LatB, explants from one clutch embryos, **Appendix A**). Thus, we conclude that Rho-GEF increases tissue stiffness primarily by activating myosin II contractility, but may also act by stimulating actin assembly or F-actin cross-linking.

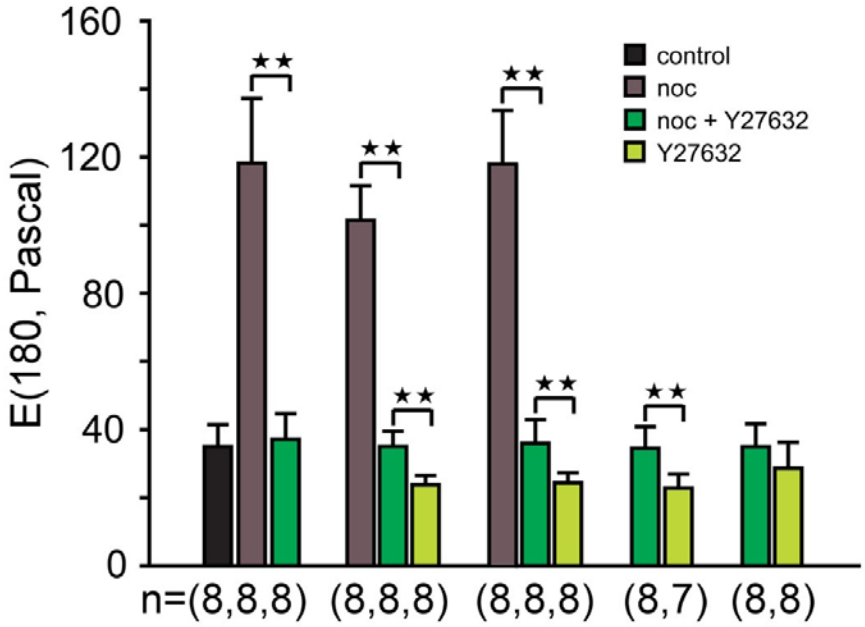

Figure 33. Y27632 suppressed the nocodazole-induced tissue stiffening.

2.2.4.5 Mechanical rescue of axial elongation caused by nocodazole

Disruption of microtubules by nocodazole induced severe defects in whole embryos (**Figure 34A and B**) and reduced the elongation rate of dorsal isolates (**Figure 35A and B**). We wondered whether these defects were due to mechanical or signaling defects. If the defects were due to mechanical stiffening we reasoned we could rescue the defective phenotype by inhibiting stiffening. To test whether we could mechanically rescue the phenotypes, we used both Xlfc-MO and Y27632 to reduce the nocodazole-induced tissue stiffening. Xlfc-MO and Y27632 decrease RhoGEF activity and myosin II contractility, respectively, and both of them had no effects on normal morphogenetic movements. However, we found that neither Xlfc-MO nor Y27632 could significantly rescue the defects caused by microtubule disruption in late gastrulation and early neurulation embryos (**Figure 34A and B**). Thus, the severe defects induced by disrupting microtubules are likely due to signaling, rather than mechanical stiffening.

Since a previous study has demonstrated that Xlfc-MO and Y27632 could rescue the convergent extension movements of Keller sandwich explants in early gastrulation embryos (Kwan and Kirschner, 2005), we then tested the mechanical rescue of axial elongation of dorsal isolates from late gastrulation and early neurulation embryos. We found that nocodazole treatment reduced the tissue elongation by 30 to 40% and Xlfc-MO significantly rescued the axial elongation (p= 0.027 < 0.05). However, 40μM Y27632 did not rescue the axial elongation. By decreasing Y27632 concentration to 10μM, we found slight, but not significant increase in the axial elongation rate (**Figure 35B**). The results suggested that rescuing the tissue stiffness by blocking GEF function could significantly increase axial elongation, while rescuing the tissue mechanics by blocking myosin II contractility did not. This suggests that disruption of microtubules affects other cell functions in addition to tissue stiffening.

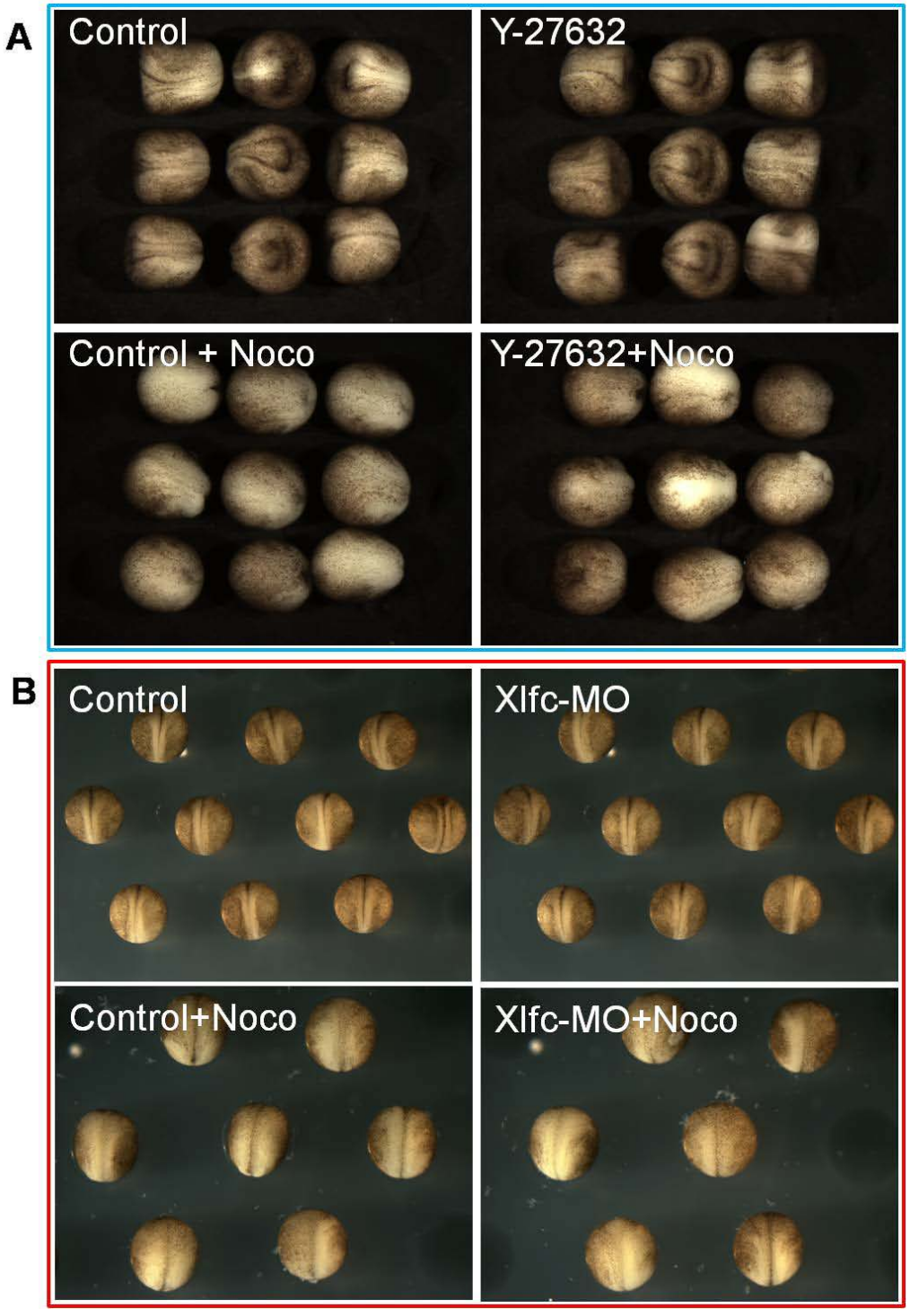

Figure 34. Mechanical rescue of defects induced by microtubule disruption.

(A) Mechanical rescue the nocodazole (50 μM) induced developmental defects using Y27632 (40 μM) , treatment started at stage 11. (B) Mechanical rescue the nocodazole (50 μM) induced developmental defects using Xlfc Morpholino (Xlfc-MO), nocodazole treatment started at stage 16.

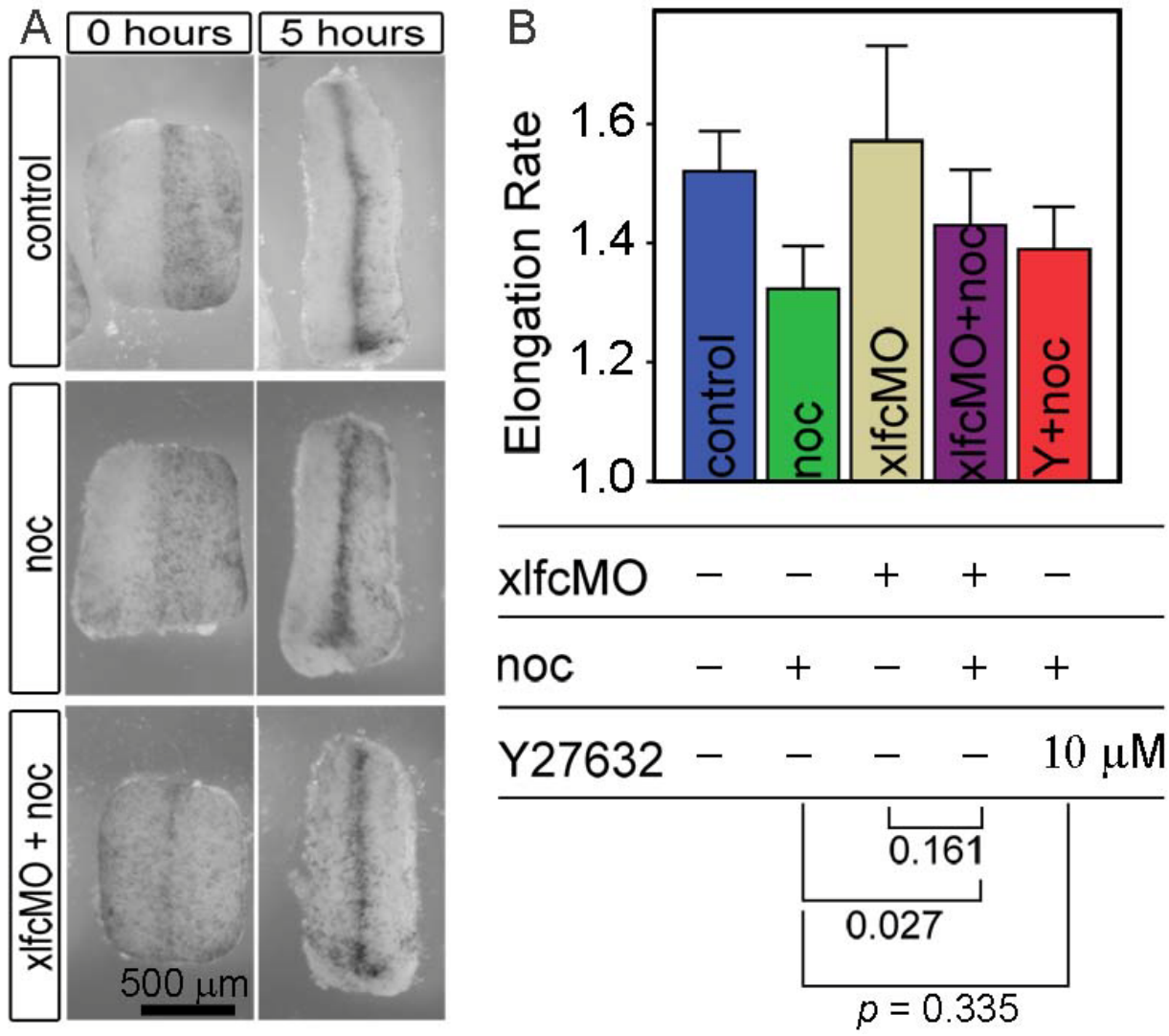

Figure 35. Mechanical rescue of axial elongation.

(A) Elongation of dorsal isolates over 5 hours in DMSO (control), nocodazole (noc) or noc and Xlfc Morpholino (xlfcMO). (B) Axial elongation rate of nocodazole treated dorsal isolates was rescued by Y27632 (Y) or XlfcMO. $p<0.05$ was considered significantly different.

2.3 DISCUSSION

By measuring the passive tissue mechanics of early frog embryonic tissues, we revealed for the first time complex spatial and temporal patterns of mechanical regulation during embryonic development. By investigating the contribution of subcellular-, cellular-, and tissue-level structures to the tissue mechanical properties, we found that, on the tissue-level, the stiffness of dorsal isolates was largely dependent on paraxial mesoderm tissues, while notochord tissue, which has been proposed to support the early embryos, was not a major contributor to the tissue mechanics. On the cellular-level, the mechanical properties of dorsal isolates were largely dependent on cells, but not ECM. On the subcellular-level, the mechanical properties of the embryonic cells were determined by actin and myosin II contractility, while MT indirectly controlled the tissue stiffness by regulating actomyosin network through a Rho-GEF mediated signaling pathway (**Figure 36**).

2.3.1 Developmental regulation of tissue stiffness

At the start of life, early embryonic tissues are extremely deformable (Moore et al., 1995), which may be necessary to allow the dynamic cell rearrangement or massive tissue movements in early morphogenesis. Once established, most adult tissues are very stiff (Levental et al., 2007). Our results connect the two ends by showing that embryonic tissues gradually increase their stiffness as they develop into next stages. And the rate of the tissue stiffening is significant as they increase 8- to 10-fold in less than 8 hours. The results also suggest that tissue mechanics like other morphogenetic movements such as cell motility and differentiation is genetically regulated.

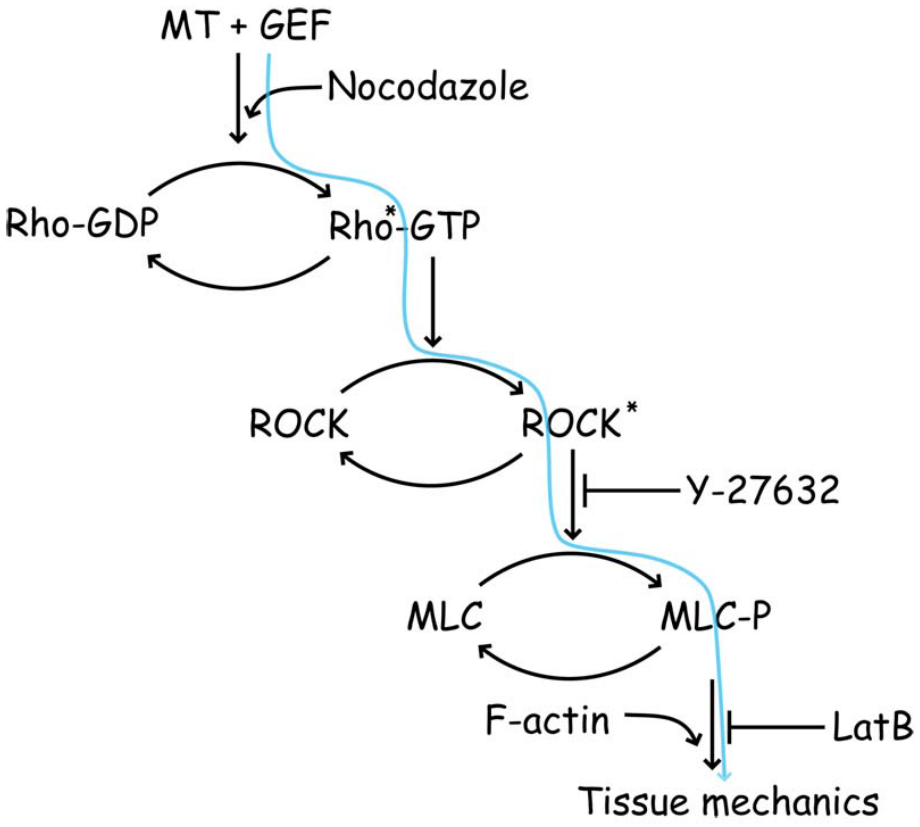

Figure 36. Molecular regulation of tissue stiffness.

2.3.2 Spatial variation in tissue stiffness

In this study, we investigated the spatiotemporal variation of tissue stiffness in early embryos. Because each component in dorsal tissues is too small or too thin to measure directly, we measured the stiffness of various explants, which contain extra components or missing some tissues, and compared their stiffness. We found that explants with two notochords were not stiffer than the explants without a notochord and explants with LiCl-enlarged notochords had similar stiffness as control explants, which indicated that notochord was not a major contributor to the tissue stiffness. We also found that explants with two notochords trapping a small amount

of paraxial-medial mesoderm between them, explants containing only medial-mesoderm, and explants without endoderm were significantly stiffer than explants without a notochord, explants containing only lateral-mesoderm and control explants, respectively. In addition, explants without neural plates were not stiffer than control explants. To estimate the stiffness of each component, we used a simple mechanical model based on the superposition of composite materials (Christensen, 1991) and found that there was large spatial variance in tissue stiffness. Endoderm is the softest tissue and is one tenth the stiffness of paraxial mesoderm tissues, the stiffest tissues, whereas notochord and neural plate tissues have similar stiffness as control dorsal tissues. The variance in tissue stiffness suggests that not only gene expression, but also mechanical properties in early embryos are spatiotemporally patterned. It is also possible that the spatiotemporal variation of tissue stiffness was caused by patterned gene expression and future studies are needed to investigate the relationship between gene expression and protein activation, and stiffness patterning. The patterned tissue stiffness may facilitate the early massive tissue rearrangement, since soft tissues are easier to be deformed.

Endoderm cells are yolk-rich cells carrying nutritive granules for other cells (Stern, 2004). During late gastrula to early neurula stages, the stiffness of endoderm tissues (around 2-10 Pascal) is very low compared to the stiffness of dorsal involuting marginal zone tissues (between 3.9 and 14.2 Pascal) in early gastrula stages (Moore et al., 1995), which indicates that endoderm tissues do not increase their stiffness during late gastrulaton and early neurulation stages. The results suggest that tissue stiffening is not a default program during development, but is more likely temporally regulated. For example, endoderm tissues undergo convergent extension in later neurulation and tail-bud stages (Larkin and Danilchik, 1999) and we suspect that the stiffness of endoderm tissues will increase during these stages.

Our results showed that notochord was not a major contributor to the tissue stiffness or late phases of convergent extension movements. We found explants without notochord could elongate at the same rate as control explants during late gastrula to early neurula stages. The results are consistent with the previous studies which demonstrated that embryos without notochord had normal morphogenetic movements and axial elongation (Malacinski and Youn, 1981; Youn and Malacinski, 1981). Thus we concluded that notochord did not play a significant mechanical role during late gastrula to early neurula stages. However, notochord was essential for early developmental movements, during which notochord cells adopt polarized protrusions and initiate convergent extension movements (Keller et al., 1989; Shih and Keller, 1992). The notochord is also essential for late embryonic development, during which the notochord stiffens and straightens to elongate the early tail-bud stage embryos (Adams et al., 1990; Koehl et al., 2000). The heterogeneity in tissue stiffness may provide positional information to embryonic cells. For examples, somite is making developmental decisions during gastrula and neurula stages, directing cells to different fates based on positional cues (Brand-Saberi and Christ, 2000; Keller, 2000). Similar to the cultured mesenchymal stem cells, which could differentiate into neurons or osteoblasts when they were attached to soft or stiff substrate, respectively, embryonic cells such as outer-layer pre-somitic cells facing stiff neural plate could develop into myotome, while inner-layer pre-somitic cells facing soft endoderm tissues could grow into sclerotome.

The spatial variation in tissue stiffness may also modulate the cellular behaviors through intracellular signaling. For example, the cortical tension, which determines the cell contractility and motility, is regulated by the stiffness of their underneath substrates (Paszek et al., 2005) and embryonic cells in stiff substrates such as mesoderm and ectoderm may have high internal tension, which in turn increase the cellular adhesion or cell motility (Levental et al., 2009).

2.3.3 ECM does not affect the tissue stiffness

Since the mechanical properties of most adult tissues such as skin, heart valves, and blood vessels are dominated by their extracellular matrix (Brooke et al., 2003; Liao et al., 2007), ECM such as collagen, fibronectin, fibrillin and laminin have been proposed to contribute to the tissue mechanics in addition to their signaling roles (Keller et al., 2003). However, we found that reducing fibronectin did not change the tissue stiffness in late gastrula stage (stage 13) and in early neurula stages (stage 16), which contain more fibronectin fibrils. The conclusion that ECM does not contribute to the stiffness of early *Xenopus* embryonic tissues is supported by several lines of evidence. First, decreasing the fibronectin fibrils reduced the assembly of fibrillin and laminin, which may be due to the dependence of fibrillin deposition and laminin polymerization on fibronectin assembly (Colognato and Yurchenco, 2000; Kinsey et al., 2008). Second, direct disruption of fibrillin by injecting fibrillin MO did not alter the tissue stiffness (8 treated and 8 control explants from one clutch embryos, **Appendix A**). Third, fibronectin, laminin and fibrillin are initially assembled and colocalize with the boundary between notochord and pre-somitic mesoderm tissues, and the physical removal of the notochord along with the ECM did not decrease the tissue stiffness. It should be noticed that there is no collagen or elastin in early *Xenopus* embryos.

One reason why ECM remains compliant may be in anticipation of the ECM remodeling during early stages (Davidson et al., 2008). Within several hours of formation, the fibrillar fibronectin matrix is constantly remodeled by cell protrusions to increase matrix density and complexity and it may be challenging for cells to pull the matrix if it were stiff. So in the early frog embryo, the dominant role of matrix is signaling, rather than mechanically supportive.

2.3.4 Actomyosin contractility regulates the tissue stiffness

Our results demonstrate that inhibition of either actin polymerization or myosin II contractility decreased tissue stiffness in a dose-dependent manner, which is consistent with the previous studies that actomyosin contractility regulates the cellular mechanics (Janmey and McCulloch, 2007) as well as the mechanics of purified gels (Gardel et al., 2006). It is possible that disruption of the actin network may affect extracellular matrix, however, since depletion of ECM did not change the tissue stiffness we conclude that tissue stiffness is directly regulated by actomyosin contractility. However, one possibility remains that decreasing actin network would potentially reduce cadherin-mediated cell-cell adhesion, which would in turn reduce the tissue stiffness. Future studies will be needed to investigate the role of cell-cell adhesion in determining tissue stiffness.

Even the highest dose of latruculin B only reduced the tissue stiffness to 30 to 40 %, which suggested that there were other cytoskeletal structures supporting the cells, such as intermediate filaments, while microtubules did not mechanically support tissue stiffness. We suspected that, since actin and myosin II determined the tissue stiffness, they may be responsible to the spatiotemporal variation in tissue mechanics. Staining of F-actin with phallacidin demonstrated that F-actin was spatially organized and there was less F-actin in endoderm than that in adjacent tissues (Zhou et al., 2009). However, staining of F-acitn and staining of phosphorylated serine of the myosin regulator light chain (pMLC) with its antibodies showed that there were no significant changes of F-actin and pMLC between different stages (Zhou et al., 2009). The results suggested that the f-actin and myosin II may account for the partial changes in spatiotemporal variation in tissue stiffness.

The complex role of actomyosin in mechanics can be further broken down. Although both reducing myosin II contractility by Y27632 and inhibiting F-actin by LatB decreased the tissue stiffness, they had distinct effects on embryonic development. Disruption of myosin II did not induce any defects in embryos, while decreasing tissue stiffness by inhibiting F-actin assembly did. The results suggested that reduction in tissue stiffness may not be necessary to disrupt normal embryonic development and indicated that tissue stiffness may not be important to the development. Alternatively, embryonic development may be robust to the tissue stiffness. For example, reducing myosin II contractility by Y27632 may affect other cellular or tissue processes such as cellular traction forces to compensate for the decreasing in tissue stiffness to allow the robust convergent extension movements.

2.3.5 MT indirectly regulates tissue stiffness through actomyosin

Earlier studies have demonstrated that microtubule depolymerization increased cellular traction forces (Danowski, 1989) and enhanced the assembly of actin stress fibers through a RhoGTPase mediated signaling pathway in culture cells (Chang et al., 2008). We extended the previous work (Kwan and Kirschner, 2005) by showing that depolymerizing microtubules by nocodazole activated GEF-H1, which elevated the Rho activity, increased actomyosin contractility, and thus increased the tissue stiffness in frog embryonic tissues. In the course of this study, we were able to rule out the mechanical role of microtubules by showing that microtubules did not mechanically contribute to the tissue stiffness. It is interesting to note that drugs such as calyculin A and jasplakinolide, which have been shown to stabilize F-actin or induce myosin II contractility, respectively, failed to increase the tissue stiffness of developing embryonic tissues,

while depolymerization of microtubules did. The results highlight that microtubules serve as a potent regulatory rather than structural components in controlling tissue mechanics.

Microtubules and their modulation of Rho GEF-H1 are reported to affect several other cellular processes. For example, they regulate the cell polarity (Kwan and Kirschner, 2005), mediate the transendothelial electrical resistance in endothelial cells (Verin et al., 2001), and control mitotic kinases during metaphase and anaphase (Birkenfeld et al., 2007). Microtubules are commonly involved in embryonic development, such as blastopore closure and neurulation in frog (Karfunkel, 1971; Lane and Keller, 1997; Lee and Harland, 2007), epiboly in zebrafish (Solnica-Krezel and Driever, 1994), epithelial-mesenchymal transition and neurulation in chick (Karfunkel, 1972; Nakaya et al., 2008). However, in these studies, microtubules and actomyosin contractility were commonly considered as two separate factors, which regulate the morphogenetic movements independently. Our results along with others reveal the cross-talk between the two systems by showing that microtubules affected the tissue movements through actomyosin contractility. Earlier work, which suggests that microtubules mechanically regulate developmental movements, should be re-evaluated, since microtubule-induced defects in the movements may be caused by the actomyosin contractility and not directly by microtubules.

To determine whether developmental defects induced by disrupting microtubules is due to mechanical or signaling, we applied two strategies to mechanical rescue the microtubule-induced tissue stiffening by reducing actomyosin contractility using Y27632 and by inhibiting Xlfc using Xlfc-MO. We found that blocking GEF function could significantly increase axial elongation, but could not fully recover the axial elongation, while blocking myosin II contractility produced a minor effect on axial elongation. The results suggested that microtubules regulate multiple cellular processes in addition to the tissue stiffness. First, microtubules

themselves control cellular processes such as vesicle transport and mitosis (Schroer and Sheetz, 1991). Second, microtubules regulate other cellular functions, such as cell migration, cell polarization, cell division and cell adhesion, through Rho GEF-H1 (Birkenfeld et al., 2007; Chang et al., 2008; Chimini and Chavrier, 2000; Kaibuchi et al., 1999; Van Aelst and Symons, 2002). Blocking myosin II contractility rescued the tissue stiffness, but could not rescue the functions related to microtubules themselves and other functions related to RhoGTPase. However, inhibiting Xlfc rescued the tissue stiffness and other functions related to RhoGTPase, but could not rescue the functions directly related to microtubules. Our mechanical rescue results indicate that microtubules not only modulate the tissue mechanics, but also affect other cellular processes.

2.3.6 Limitation of the current study

Throughout this chapter we have applied mechanical tests to understand the embryonic developmental process. As a pioneer study in developmental biomechanics, our current work has several limitations. First, the mechanical tests of embryonic tissues are simple uni-axial unconfined compressive stress-relaxation tests, and we made several assumptions to facilitate the analysis, such as constant cross-section area of the tissues during 180-second compression tests and constant strain applied to the tissues. Second, our current version of nano-Newton force measurement device is not able to perform more complicated mechanical tests, such as bi-axial stretch tests due to the difficulties to grip the fragile tissues to apply forces. Third, our device is not able to directly measure the stiffness of each component in dorsal isolates such as notochord, endoderm, and ectoderm due to the difficulties to measure too small or too thin tissues. More

advanced devices are needed to be developed to perform more accurate mechanical tests to reveal the spatial patterns of tissue mechanics during embryonic development.

3.0 ACTIVE FORCE PRODUCTION OF EMBRYONIC TISSUES

Convergent extension (CE) is a major contributor to the morphogenetic movements that physically shape the early vertebrate embryo. During CE dorsal embryonic tissues progressively deform themselves and elongate the whole embryo along the anterior-posterior (AP) axis while narrowing in the medial-lateral (ML) direction (Keller et al., 2003). From a mechanical perspective, the degree of deformation must be proportional to active forces, which drive the tissue deformation, and must be inversely proportional to passive tissue mechanical properties such as stiffness, which resist deformation. Our previous studies (see **chapter 2**) indicated that the stiffness of the dorsal isolates increased eight- to ten-fold during CE, yet, these tissues maintain a nearly constant elongation rate over this same time period. Another finding from that same study revealed that both whole embryos and dorsal isolates cultured in a Rho Kinase inhibitor could also maintain constant elongation rates indistinguishable from controls. This suggests that the bulk tissue extension forces may be balanced to match the changes in tissue stiffness (Davidson et al., 2009b). How do tissues manage such robust and consistent morphogenesis in the face of environmental and genetic variations in real populations? The coordination of force-production with the local mechanical environment could be accomplished through a variety of mechanisms ranging from purely mechanical feedback to mechanosensing and signaling pathways (Schwartz and DeSimone, 2008). Alternatively, dorsal isolates may ignore signals from their external mechanical environment and generate the same amount of

force regardless of the stiffness of the rest of the embryo. However, no direct mechanical measurements of force production by embryonic tissues are available to test whether force-production is independent of the local microenvironment or whether mechanosensing and signaling operates. Thus, in order to understand how force and stiffness are coordinated in multicellular tissues we need to reliably control and measure these forces.

Measurements of force generation, like measurements of tissue stiffness, can be difficult to extend to the large numbers of samples needed to accommodate natural variations between embryos. First, embryonic tissues are small and generate forces as low as a microNewton over areas as large as 0.1 mm^2 (Moore, 1994). Second, the active elongation process continues for several hours during morphogenesis, which requires force sensors to have little or no drift over these time scales. Third, the elongating tissues are constantly changing their three-dimensional shapes, which make it hard to grip the tissues to apply or measure forces. Lastly, high throughput methods are essential in order to test the contribution of genes or proteins to the tissue extension forces. For these reasons we developed a new approach to measure tissue-scale force-production and investigate the mechanical control of robust elongation during convergent extension.

In this chapter we report here the development of a reliable, high throughput technique to measure force-production by converging and extending dorsal isolates microsurgically explanted from gastrulating *Xenopus laevis* embryos and use this technique to reveal otherwise cryptic changes in force production that balance altered tissue stiffness, allowing for robust convergent extension movements. Briefly, the new method is to embed dorsal isolates in agarose gel with fluorescent beads and use the agarose gel as a force sensor. When the tissues elongate along their anterior-posterior axis, they deform the surrounding gel. The deformation of the gel is detected by tracking the fluorescent beads. The mechanical properties of the agarose gel are measured

using a rheometer and then the extending force of dorsal isolate is computed using a finite element model based on the displacement and viscoelastic properties of the gel.

3.1 EXPERIMENTAL METHODS

3.1.1 Embryo and tissue preparation

Xenopus laevis embryos are obtained by standard methods (Kay and Peng, 1991), fertilized in vitro, dejellied in 2% cysteine and cultured in 1/3X MBS (Sive et al., 2000) at 14.5 - 21ºC to stage 16 (Nieuwkoop and Faber, 1967). Before making explants, vitelline membranes of embryos are removed with forceps (Fine Science Tools Inc., Foster City CA) and transferred in DFA media (Danichik's For Amy; (Sater et al., 1993)). Dorsal isolates and animal cap tissues are microsurgically dissected from embryos using hair loops and hair knives. The tissues can be harvested from mid-gastrulation (stage 11.5) to neural tube stages (stage 22) and beyond.

3.1.2 Histology, Immunocytochechistry and Confocal Microscopy

Fibronectin fibril staining is used to outline the tissue architecture of dorsal isolates. To stain fibronectin, explants embedded in agarose gel are fixed in 3% TCA in 1X PBS (Davidson et al., 2004). Fibronectin fibrils are recognized with primary antibody mAb 4H2 (Ramos and DeSimone, 1996) against *Xenopus* fibronectin (1:500) and visualized with a rhodamine conjugated goat anti-mouse IgG antibody (1:200, Jackson ImmunoResearch Laboratory, West Grove PA). After staining, the dorsal isolates are dehydrated in methanol and cleared in Murray's

clear (Davidson et al., 2004). Single optical sections and z-series of explants are collected with a confocal laser scan head (SP5, Leica Microsystems, Inc.) mounted on an inverted compound microscope (DMI6000, Leica Microsystems, Inc.) using image acquisition software (LASAF, Leica Microsystems, Inc.). Average projection and reslicing of z-series stacks is obtained with ImageJ (v. 1.38, Wayne Rasband, NIH).

3.1.3 Gel preparation

To measure the tissue extension forces, dorsal tissues are embedded in agarose gel. Briefly, low melting temperature agarose power (type IX-A; Sigma) is dissolved in DFA solution at 65 ºC and cast in a 13x10x6 mm confocal chamber. The mixture gel is cooled to room temperature (RT) and remains liquid. Red fluorescence beads (*580/605*; absorption/emission wavelength in nm, *Molecular Probes*, Eugene, OR, USA) are evenly dispersed in the liquid solution as markers to track the deformation of the gel. Dorsal tissues or animal cap tissues are prepared and allowed to heal for 20 minutes to clear debris and avoid wound healing effects. The explants are then transferred to the liquid gel at room temperature and the whole chamber is moved to a 14.5 ºC incubator to chill for 20-30 minutes. The solution is gelled in less than 15 minutes at 14.5 ºC and remains solid at RT. DFA solution are then added to the top of the gel to provide necessary media to culture the tissues.

3.1.4 Mechanical properties of agarose gel

The mechanical properties of agarose gel were measured to extract parameters needed to model gel deformation in finite element (FE) model. Since the maximum local strain induced by

extending dorsal isolates in gel domain was estimated to be less than 20% over 5 hours, the agarose gel was modeled as a linear viscoelastic material (Findley et al., 1989; Normand et al., 2000). The viscoelastic properties of the agarose gel are characterized by oscillatory shear flow tests using a rheometer (AR2000, TA Instruments). Briefly, molten agarose solution is cast between temperature-controlled plate and the rheometer geometry (40 mm diameter) at room temperature and then chilled to 14.5ºC for 20 minutes to allow the gelation of agarose. The gel is covered by light oil to prevent dehydration. The bulk elastic modulus *G'* (or storage modulus) and viscous modulus *G''* (or loss modulus) of agarose gel as a function of frequencies ranging from 0.1 to 100 rad/s have been measured in frequency sweep shear mode (**Figure 37A**). The elastic modulus is an order of magnitude larger than its viscous modulus, so the mechanical properties of agarose gel are dominated by its elastic response (**Figure 37B**). To estimate viscoelastic parameters needed for FE model, the measured elastic modulus over frequencies is fitted with a two-mode linear viscoelastic model using Mathcad (v14, PTC, MA), and then the extracted parameters (long-term elastic modulus, elastic modulus at each mode and its corresponding relaxation time) are used to build the Prony series to model the visoelastic material in FE model (Zeng et al., 2006). An example of the fitting curve and derived results including shear modulus and relaxation times are shown in (**Figure 37C**). The long-term elastic modulus is typically 26, 200 and 500 Pa for gel with concentration of 0.6%, 0.9% and 1.2%, respectively. The Poisson's ratio of the agarose gels is assumed to be 0.5 as measured in a previous study (Normand et al., 2000). During creep tests, agarose gels did not fully recover to zero strain after the load was removed (**Figure 37D**). To account for this possibility, we decided to compare null force bead map at time 0 to force load bead map after 4 hours to determine the gel deformation.

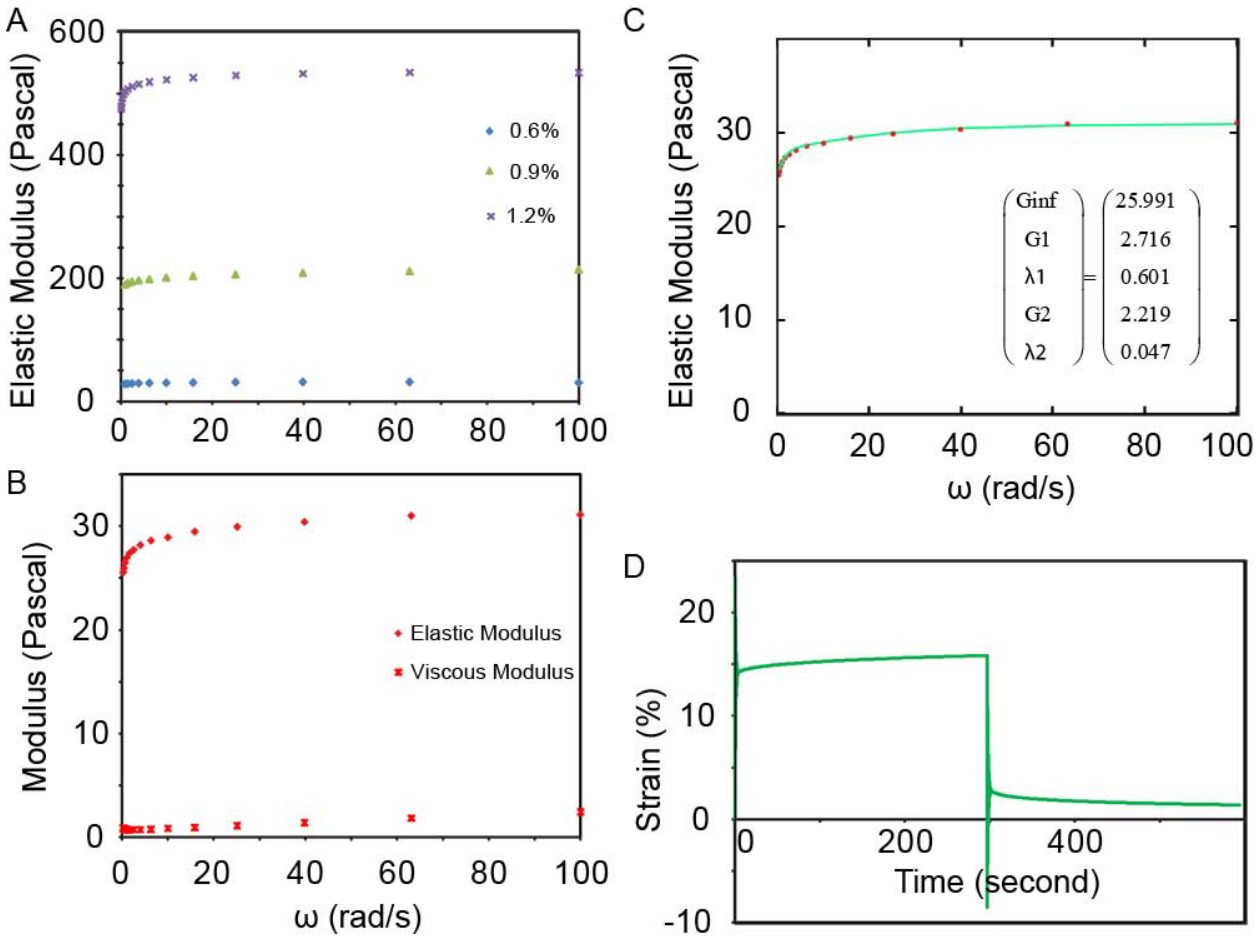

Figure 37. Mechanical properties of agarose gel.

(A) Elastic modulus of 0.6%, 0.9%, and 1.2% agarose gel at frequency between 0.1 and 100 rads/s. (B) An example of elastic and viscous modulus of 0.6% agarose gel. (C) Elastic modulus of 0.6% gel (red dots) is fitted with two-mode linear viscoelastic model (green line). (D) Creep tests of 0.6% agarose gel under 5 Pascal stress.

3.1.5 Confocal microscopy and image processing

Central to resolving force production is tracking gel deformation through the movement of beads embedded in the gel. We reported two methods to track the movement of fluorescence beads. The first method tracks individual beads in confocal time-lapse imaging, while the second method tracks groups of beads by registration of two images taken at different time points.

3.1.5.1 Detecting gel deformation by tracking individual beads

To determine the gel deformation, we first tracked the movement of each individual bead detected surrounding elongating dorsal isolates. Red fluorescence beads (1 μm) are embedded in agarose gel and scanned using 20X plan apo objective (n.a 0.70). XY confocal images at the middle plane in tissue's dorsal-ventral direction are acquired every 3 minutes in a time series using a confocal laser scan head (SP5, Leica Microsystems, Inc.) mounted on an inverted compound microscope (DMI6000, Leica Microsystems, Inc.) using image acquisition software (LASAF, Leica Microsystems, Inc.). To track the positions of each individual bead during tissue elongation, XY time (XYT) series are analyzed using a plugin for multiple particle detection and tracking (Sbalzarini and Koumoutsakos, 2005) with ImageJ (v. 1.38, Wayne Rasband, NIH). The algorithm assumes that fluorescent beads have limited speed and contains three steps. First, the background of each frame is subtracted by a boxcar average over a defined region. The noise is further reduced by adjusting intensity threshold. The second step is to detect beads in every frame. The rough location of beads is determined by local intensity maxima which are calculated by grayscale dilation. Then the sub-pixel resolution of bead position is achieved by calculating the geometric centre of the brightness-weighted centroid. The third step is to link the beads

detected in each frame by choosing the closest point in subsequent frames. Then the trajectory of each bead over multiple frames is computed. Nodal coordinates of each bead are obtained from its trajectory and the displacement of beads is calculated by subtracting its nodal coordinate at one time point from its coordinate at next time point.

3.1.5.2 Detecting gel deformation by image registration

To develop a high throughput method to track the deformation in gel domain, we adapted an image registration algorithm (bUnwarpJ, (Sorzano et al., 2005)), which registers two images by deforming one image to match the other. Briefly, three different sizes of red fluorescent beads (0.2 μm, 1 μm, and 15 μm) were suspended in gel and initially scanned using a 10X objective. The largest beads help us manually match the tissue position at different time points and the smallest beads provide contrast level of the gel which assists the algorithm to obtain better resolution. A confocal z-stack is collected around the middle plane of the tissue explant every 2 hours and maximal projection of each z-series stacks is obtained with ImageJ. Two maximal projection images of each explant at different time points are first aligned (TurboReg, (Thevenaz et al., 1998)). The resulting rigid-body alignment allows us to reduce potential drift between the two images. Subsequent steps of image registration identify in-plane strain rather than rotational or translational displacement.

3.1.6 Finite element model

To compute the stress field in the gel based on the displacement field and the viscoelastic properties of the gel, a two-dimensional finite element (FE) model was constructed. In the

following sections, we will describe the three steps, pre-processing, simulation, and post-processing, which are needed to build the FE model to estimate the stress produced by extending dorsal isolates.

3.1.6.1 Pre-processing

The pre-processing includes four steps: modeling of the geometry, meshing, modeling the material properties, and specification of boundary, initial and loading conditions. During the pre-processing, an input file is created to store the necessary information to construct the finite element models, such as FE mesh, extracted viscoelatic parameters of the agarose gel, initial conditions and displacement boundary conditions of the gel.

(a) Modelling of the geometry

In our FE model, the gel domain is assumed to be isotropic, since the gel is well mixed and is not subject to strain as it forms. We assume the gel domain is homogeneous and the material property of the gel is not direction-dependent. The gel domain is also assumed to be linear viscoelastic, since the agarose gel is compressed by the elongated tissue in our experiments and the strain in gel domain is estimated to be less than 20% based on the displacement of beads (Normand et al., 2000). Three-node linear two-dimensional plane stress triangle elements (CPS3) are used for simulations. The CPS3 element allows nonlinear relationships between stress and displacement from material nonlinearity, geometric nonlinearity, and boundary nonlinearity. To compensate the effect of geometric nonlinearities due to large deformation in the agarose gel, we turn on the NLGEOM option.

(b) Meshing

To represent the gel we generate a two-dimensional finite element mesh based on the position of each bead reported from a bead tracking algorithm (Sbalzarini and Koumoutsakos, 2005). Triangular elements are constructed and then refined to generate elements with same areas and to remove small or large angles by inserting extra nodes into the mesh with a free software TRIANGLE (version 1.6, CMU, Pittsburgh). To construct meshes based on the output from the image registration algorithm, we divide the whole displacement field in gel domain into small windows (32×32 pixels). The center of each window is calculated and the mean displacement of each window is computed. Using these windows the meshing algorithm produces triangular elements with identical area and optimal shapes.

(c) Modeling the material properties of agarose gel

To model the agarose gel as linear viscoelastic material, we use the following constitutive equation:

$$\boldsymbol{\sigma(t)} = \int_{-\infty}^{t} \boldsymbol{E(t-t')} * \frac{\boldsymbol{d}}{\boldsymbol{dt}} \boldsymbol{\varepsilon(t')dt'} \quad \textbf{(3-1)}$$

where $\boldsymbol{\sigma(t)}$ and $\frac{\boldsymbol{d}}{\boldsymbol{dt}}\boldsymbol{\varepsilon(t)}$ are the stress tensor and strain rate tensor, respectively, $\boldsymbol{E(t)}$ is the relaxation modulus:

$$\boldsymbol{E(t)} = \boldsymbol{E_{\infty}} + \sum_{j=1}^{N} \boldsymbol{E_j} * \boldsymbol{e^{-t/\tau_j}} \quad \textbf{(3-2)}$$

where $\boldsymbol{E_{\infty}}$ is the long-term elastic modulus, $\boldsymbol{E_j}$ and $\boldsymbol{\tau_j}$ is the elastic modulus and relaxation time, respectively, at each mode of relaxation. The above generalized Maxwell model contains infinite numbers of spring-dashpot Maxwell elements in parallel to accurately capture the viscous response of the linear viscoelastic material. A previous study has demonstrated that two-mode

Maxwell model was sufficient to represent the viscoelasticity of agarose gel (Zeng et al., 2006), so we apply two-mode Maxwell model to model the gel. The two-mode model in frequency domain is defined as:

$$E'(\omega) = E_{\infty} + \frac{E_1\omega^2\tau_1^2}{1+\omega^2\tau_1^2} + \frac{E_2\omega^2\tau_2^2}{1+\omega^2\tau_2^2} \quad \textbf{(3-3)}$$

$$E''(\omega) = \frac{E_1\omega\tau}{1+\omega^2\tau_1^2} + \frac{E_2\omega\tau}{1+\omega^2\tau_2^2} \quad \textbf{(3-4)}$$

where E', E'' are the storage modulus and loss modulus, respectively. To obtain the parameters to represent the viscoelastic behavior of agarose gel in our FE solver (ABAQUS, Student version 6.5, Abaqus, Inc.) , we fitted the measured storage modulus as a function of frequency to data collected using oscillatory shear flow tests (Section 3.1.4) using the equation (3-3).

In ABAQUS, the storage modulus can be defined using a Prony series expression:

$$g_R(t) = 1 - \sum_{i=1}^{N} g_i * (1 - e^{-t/\tau_i}) \quad \textbf{(3-5)}$$

where τ_i is the relaxation time, and $g_R(t)$, the relaxation modulus in dimensionless form, defined as:

$$g_R(t) = \frac{E(t)}{E_0} \quad \textbf{(3-6)}$$

where $E(t)$ is the time dependent relaxation modulus in equation (3-2), and E_0 is the instantaneous relaxation modulus. Since the solid agarose gel is nearly incompressible, we assume the Poisson's ratio is 0.5 (Normand et al., 2000).

(d) Boundary, initial and loading conditions

A finite element model allows us to compute stresses from applied displacements by dividing the whole agarose gel into many small elements. The mechanical behavior of each element is governed by three equations: 1) relating strain and displacement, 2) relating stress and strain, and 3) evaluating the static stress equilibrium in each element. The equations for each element are

assembled together in matrix form; mechanical equilibrium and the resulting displacement and stresses are solved for the series of linear equations.

ABAQUS uses the Green's strain matrix to calculate the strain from displacement:

$$\boldsymbol{\varepsilon^G} = \frac{1}{2} * (\boldsymbol{F^T} \cdot \boldsymbol{F} - \boldsymbol{I}) \quad \textbf{(3-7)}$$

where $\boldsymbol{\varepsilon^G}$ is Green's strain matrix, $\boldsymbol{I}$ is the two-dimensional identity tensor, and $\boldsymbol{F^T}$ is the transpose of $\boldsymbol{F}$, which is the deformation gradient tensor and defined as:

$$\boldsymbol{F} = \begin{bmatrix} \frac{\partial u}{\partial X} & \frac{\partial u}{\partial Y} \\ \frac{\partial v}{\partial X} & \frac{\partial v}{\partial Y} \end{bmatrix} + \boldsymbol{I} \quad \textbf{(3-8)}$$

where $\boldsymbol{u}$ and $\boldsymbol{v}$ are the displacements in X- and Y-direction, respectively. For a linear viscoelastic material, the relationship between stress and strain is given by equation (3-2). And the static stress equilibrium for two-dimensional stress plane is governed by:

$$\frac{\partial \sigma}{\partial x} + \boldsymbol{f} = \boldsymbol{0} \quad \textbf{(3-9)}$$

where $\boldsymbol{\sigma}$ is the stress tensor and $\boldsymbol{f}$ is the force tensor.

In order to compute the stresses from displacements, we apply the displacements of the gel as load by defining the boundary conditions and assume that there is no pre-stress presented at the tissue-gel interface before imaging, so the initial condition of the model would be the original positions of the gel at the beginning of tissue extension.

For each step, there are multiple types of analysis in the FE solver, such as static stress analysis, dynamic stress analysis, or visco stress analysis. To model the viscoelastic response of agarose gel, we choose visco stress analysis, which is used to get a transient static stress analysis with time-dependent material response such as viscoelasticity (ABAQUS, 2007). In summary, nonlinear visco stress analysis is used to perform the analysis, and NLGEOM and VISCO parameters on the *STEP option are chosen. A sample ABAQUS input file (.inp) is shown in APPENDIX B.

3.1.6.2 Simulation

Simulation is needed to solve the linear equations. After an input file (.inp) containing the FE mesh, viscoelatic parameters of the agarose gel, initial conditions, and displacement boundary conditions of the gel is created in the pre-processing section. The input file is then imported into the solver of a commercial finite element software ABAQUS to compute the stress distribution in the gel surrounding a sample. ABAQUS uses a Newton solution technique (ABAQUS, 2007) to analyze the nonlinear problems. In brief, displacement is increased step by step over time. For each time increment, the solution converges if it satisfies the preset viscoelastic strain error tolerance, which is less than 0.01%. If the solution does not converge, the solver iteratively reduces the time step by 25% until convergence is achieved.

3.1.6.3 Post-processing

Post-processing is needed to extract stress data from the outputs of FE models. After simulation, the stresses are calculated at specific nodes on the elements. The von Mises stress of each node immediately surrounding anterior and posterior ends of tissues is extracted from the output files (.rpt). To determine the nodes marking the anterior or posterior ends of embedded explant, we first dilated the mask of the source image (image at time 0) by 32 pixels and used the mask to identify all the nodes immediately adjacent to the explant on anterior-posterior and medial-lateral boundaries. Then a preset stress threshold is applied to remove the nodes which are on the medial and lateral sides of the tissue. We calculate mean stress $<\sigma>$ and maximum stress σ_{max} from the stress values of nodes located on anterior and posterior ends of the embedded tissues.

3.1.7 Direct calculation of strain

To validate the precision of strain output from FE model, we directly calculated the nominal strain (NE) from the displacement map in agarose gel produced using image registration. To measure the strain, we first calculated the 2D displacement gradient tensor $\boldsymbol{H}$:

$$\boldsymbol{H} = \begin{bmatrix} \frac{\partial u}{\partial X} & \frac{\partial u}{\partial Y} \\ \frac{\partial v}{\partial X} & \frac{\partial v}{\partial Y} \end{bmatrix} \quad \textbf{(3-10)}$$

where **u** and **v** are the displacements in x- and y-direction, respectively and are defined as:

$$u = X - x$$

$$v = Y - y$$

where (**X**, **Y**) and (**x**, , **y**) are the reference point and deformed point, respectively. Then the deformation gradient tensor **F** is computed by:

$$\boldsymbol{F} = \boldsymbol{H} + \boldsymbol{I} \quad \textbf{(3-11)}$$

where **I** is the two-dimensional identity tensor. With the deformation gradient tensor, the nominal strain **NE** (or Biot's strain) is calculated by:

$$\boldsymbol{NE} = \sqrt{\boldsymbol{F} * \boldsymbol{F}^{\boldsymbol{T}}} - \boldsymbol{I} \quad \textbf{(3-12)}$$

where $\mathbf{F^T}$ is the transpose of **F**. The directly calculated nominal strain was then compared to the nominal strain outputted from the FE solver ABAQUS.

3.1.8 Verify finite element model with spherical indentation

To demonstrate the precision of stress measurement using FE model, we chose to verify our newly developed technique against the well case of spherical indentation. A solid sphere (ball-point from blue pen, uniball corp) of radius ($R = 250$ μm) attached to an optical fiber is used to

indent agarose gel with a half space surface to depth (d) (**Figure 45A**). We coated the solid sphere with very small green fluorescent microspheres (0.2 μm FluoSpheres, *660/680*; absorption/emission wavelength in nm, *Molecular Probes*, Eugene, OR, USA) to detect the deflection (Δx) of optical fiber as it contacts an agarose gel labeled with three types of red fluorescent beads with different sizes (0.2 μm, 1 μm, and 15 μm FluoSpheres, *580/605*; absorption/emission wavelength in nm, *Molecular Probes*, Eugene, OR, USA). Contrasting fluorescent markers on the indenting sphere and in the gel allow us to calculate deformation. The displacement of the optical fiber and the displacements of fluorescent beads in gel domain are recorded using confocal microscopy with 10X objective. Briefly, a confocal z-stack is collected around the middle plane of the solid sphere and a maximal projection of the z-series stacks is produced. To compensate for the viscosity of agarose gel, we wait three minutes for viscous response to dissipate (the gel's relaxation time is less than one second) before collecting z-stack confocal images after each indentation. The applied force is computed by Hooke's law ($F = -k * \Delta x$), where k is the spring constant of the optical fiber determined using a method described previously (Davidson and Keller, 2007). According to the Hertz contact theory (Fischer-Cripps, 2007), the Hertzian contact stress (σ_H) is:

$$\frac{\sigma_H}{p_m} = -\frac{3}{2}\left(1 - \frac{r^2}{a^2}\right) \quad r \leq a \tag{3-13}$$

where $\boldsymbol{a}$ ($=\sqrt{R * d}$) is the contact area of radius, $\boldsymbol{r}$ is the radial distance, and $\boldsymbol{p_m}$ ($=F/\pi a^2$) is the mean contact pressure (**Figure 45A**). The maximum Hertzian contact stress ($\sigma_{H,max}$) is at the center of contact ($r = 0$):

$$\sigma_{H,max} = -\frac{3}{2}p_m = -\frac{3F}{2\pi a^2} \tag{3-14}$$

where ***F*** is the applied force. The stress distribution in gel domain caused by indentation of the solid sphere is computed by our new method and the maximum von Mises stress ($\sigma_{\max}$) at the center of contact is compared to $\sigma_{H,\max}$ (**Figure 45A**).

3.1.9 Measure the tissue extension forces using a long optical fiber

To further validate the precision of stress measurement using FE model, a long optical fiber is prepared to work as a force transducer with spring constant (k = 6.38 nN/μm) to measure the average stress exerted by extending dorsal isolates (**Figure 46A**). Briefly, a dorsal isolate is placed between an immobile backstage and the optical fiber along its anterior-posterior (AP) direction (**Figure 46B**). As the tissue extends, it deforms the optical fiber whose position is recorded by a high resolution objective mounted to a CCD camera. Deflection (Δx) of the fiber and the cross-section area (A) of the tissue at tissue-fiber contact are manually measured using imageJ. The force (F) is computed from the displacement of the fiber and its spring constant by Hooke's law ($F = -k * \Delta x$). The mean stress or pressure (p_m) is calculated by dividing force with its cross-section area ($p_m = F/A$).

3.1.10 Data analysis

The σ_{max} and $<\sigma>$ represent the magnitude of stress in agarose gel applied by an embedded tissue. Two-way ANOVA, which includes treatment and clutch as fixed and random factor, respective, is used to calculate the statistical difference of σ_{max} and $<\sigma>$ between posterior and anterior ends of each tissue, between control and Y27632-treated explants, between sham control and notochord-less explants, or between tissues embedded in gels with different stiffness.

3.2 RESULTS

3.2.1 The gel force sensor

In order to quantify the forces driving convergent extension, we developed a new method to measure force using an agarose gel as a force sensor. Agarose gels have been used to culture cells or tissues and its mechanical properties have been extensively characterized (Balgude et al., 2001; Chen et al., 2004; Gordon et al., 2003; Normand et al., 2000; Ross and Scanlon, 1999; Tokita and Hikichi, 1987; Zeng et al., 2006). We embed microsurgically isolated *Xenopus laevis* embryonic tissues that include the dorsal anlagen (referred to here as the dorsal isolate) in low-gelling temperature agarose in a fluid state at room temperature (**Figure 38A**). Chilling the fluid agarose to 14.5 ºC causes the agarose to solidify around the dorsal isolate. Immediately after gelling, the solid agarose immobilizes the explant, but as the dorsal isolate generates force it pushes on and deforms the surrounding gel along the AP axis (**Figure 38B**). Thus, the gel serves to both hold the tissue in place and acts as a force sensor. In brief, we assess the force production of the explants by first obtaining a map of bead displacements in the gel either by tracking embedded individual fluorescent beads or by tracking groups of beads. To calculate forces from the displacement map of the gel we use a finite element model of the agarose gel. The finite element model requires information on the mechanical properties of the gel which we obtained using a rheometer. Lastly, the finite element model is used to compute the stress field surrounding the elongating tissues from the displacement field and the mechanical properties of the gel (**Figure 38C**).

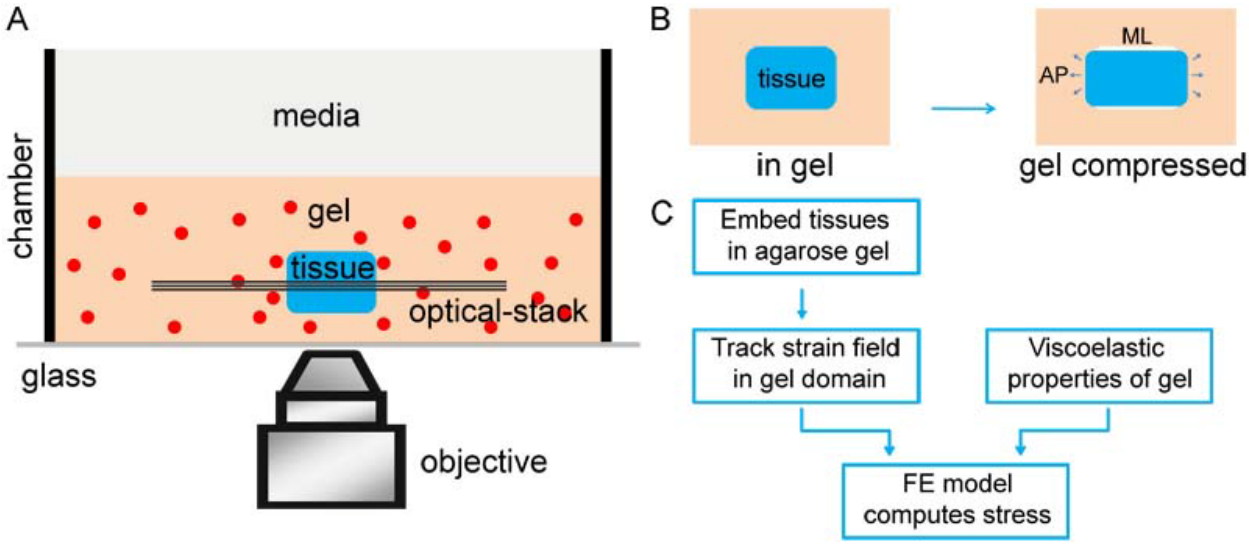

Figure 38. Gel force sensor.

(A) Schematic of gel force sensor shows a dorsal isolate embedded in agarose gel with fluorescent beads. Optical-stack is taken across the center of the tissue to detect the gel deformation. (B) When tissues converge in mediolateral direction and extend along anterior-posterior (AP) axis, they compress the gel in AP ends. (C) Flow chart of the procedure for computing tissue extension forces.

3.2.1.1 Building FE model based on tracking individual beads

As a first step in determining the forces produced by a converging and extending explant we determined the deformation of the gel by tracking individual fluorescent beads embedded in agarose gel (**Figure 39A**). We used a particle tracking algorithm (Sbalzarini and Koumoutsakos, 2005) to analyze displacement of beads obtained from confocal time-lapse imaging and report the bead trajectories (**Figure 39A**). The beads closer to the ends of the tissue along the AP axis moved greater distance (**Figure 39B**), while beads further from the tissue showed little displacement (**Figure 39A**). In order to extract local stresses from maps of bead displacements

we constructed a finite element model based on the positions of every detected bead (**Figure 39C**). We assumed there were no stresses present at the start of the experiment and calculated forces needed to displace each bead in the gel domain to their final position. In standard engineering terms we calculated the stresses within the gel produced by the elongating explant. We computed the equivalent or von Mises stress, which we will simply refer to as 'stress' (σ; (Fischer-Cripps, 2007)) using a commercially available FE solver (see Methods) based on the bead displacements and the viscoelastic properties of agarose gel (**Figure 39D**). We have found that the embedded tissues extend up to 4 hours in the gel and produced a maximum stress (σ_{max}) of 7 Pa (**Figure 39D**). Tissues or embryos confined in gels develop normally through late gastrula and neurula stages (data not shown). The maximum stress always colocalizes with the mediolateral midline of the dorsal isolate (**Figure 39D**), suggesting that the notochord, the most medial tissue, and surrounding pre-somitic mesoderm tissues extends faster and produces larger forces compared to the other tissues.

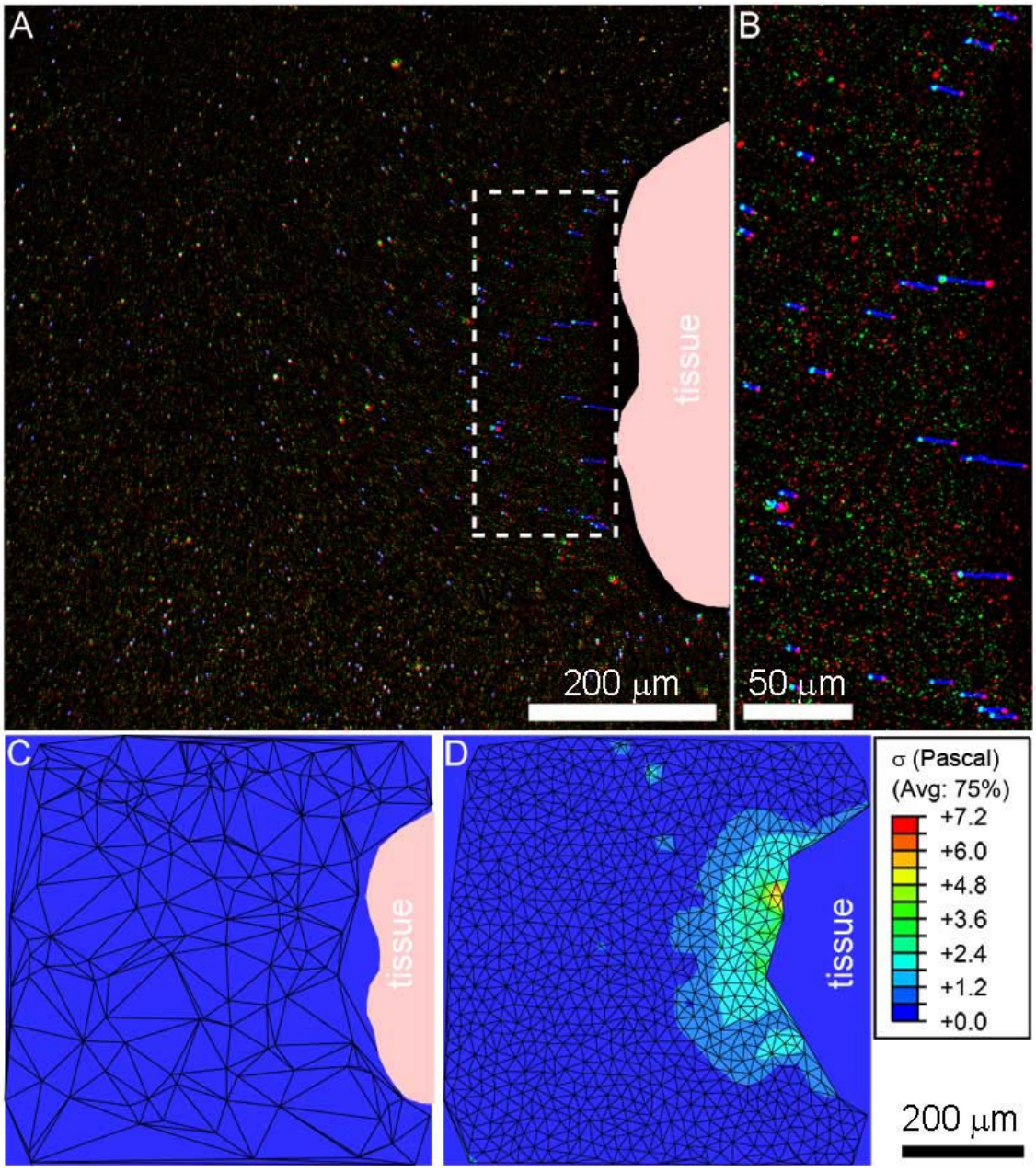

Figure 39. Building FE model based on tracking individual beads.

(A) As tissue (pink) extends, the immediately surrounding gel (black) is deformed demonstrated by embedded fluorescent beads at time 0 (red), after 4 hours (green) and the trajectories of the beads (blue). (B) The beads closer to the ends of the tissue along the AP axis (dash line window in D) moved greater distance. (C) Two-dimensional mesh is built based on the positions of individual beads at time 0. (D) The mesh is refined and the stress field is reported based on the bead displacements and the viscoelastic properties of agarose gel.

3.2.1.2 Building FE model based on tracking groups of beads

The particle tracking algorithm can only track beads if their movements between two consecutive time frames are small. To meet this requirement we collected time-lapse series of images every 3 to10 minutes. Collecting a time-lapse series such as this places practical limits on the number of explants that can be tested at the same time. To develop a high throughput method where more explants could be tracked simultaneously, we adapted an image registration algorithm which detects the deformations in agarose gel by tracking groups of beads (Sorzano et al., 2005). This method, called image registration, uses b-splines to recreate a displacement map between two images collected at much larger time intervals, up to 4 hours. We use this image registration technique to measure the extension forces produced by multiple samples for the remainder of this dissertation.

Elongating dorsal isolates positioned in the gel with the mediolateral axis and anterior-posterior axis aligned with the plane of the confocal section deformed the agarose gel at both anterior and posterior ends of the explant (**Figure 40A and C**). Often as the dorsal isolate converges and extends it loses contact with the gel along the mediolateral sides of the isolate (**Figure 40B and B'**). The displacement of the gel is reported by registration of the two images, one taken shortly after the explant is immobilized and one 4 hours later (**Figure 40D**). The stress distribution in the gel surrounding the explant is computed using a finite element model (**Figure 40E**). We routinely found that posterior ends produced different spatial patterns of stress than the anterior ends; for instance, the posterior end produces a higher, more axially focused pattern of stress than that of the anterior end (**Figure 40E and F**) even though we found no significant difference comparing the maximum or mean stress between the two ends.

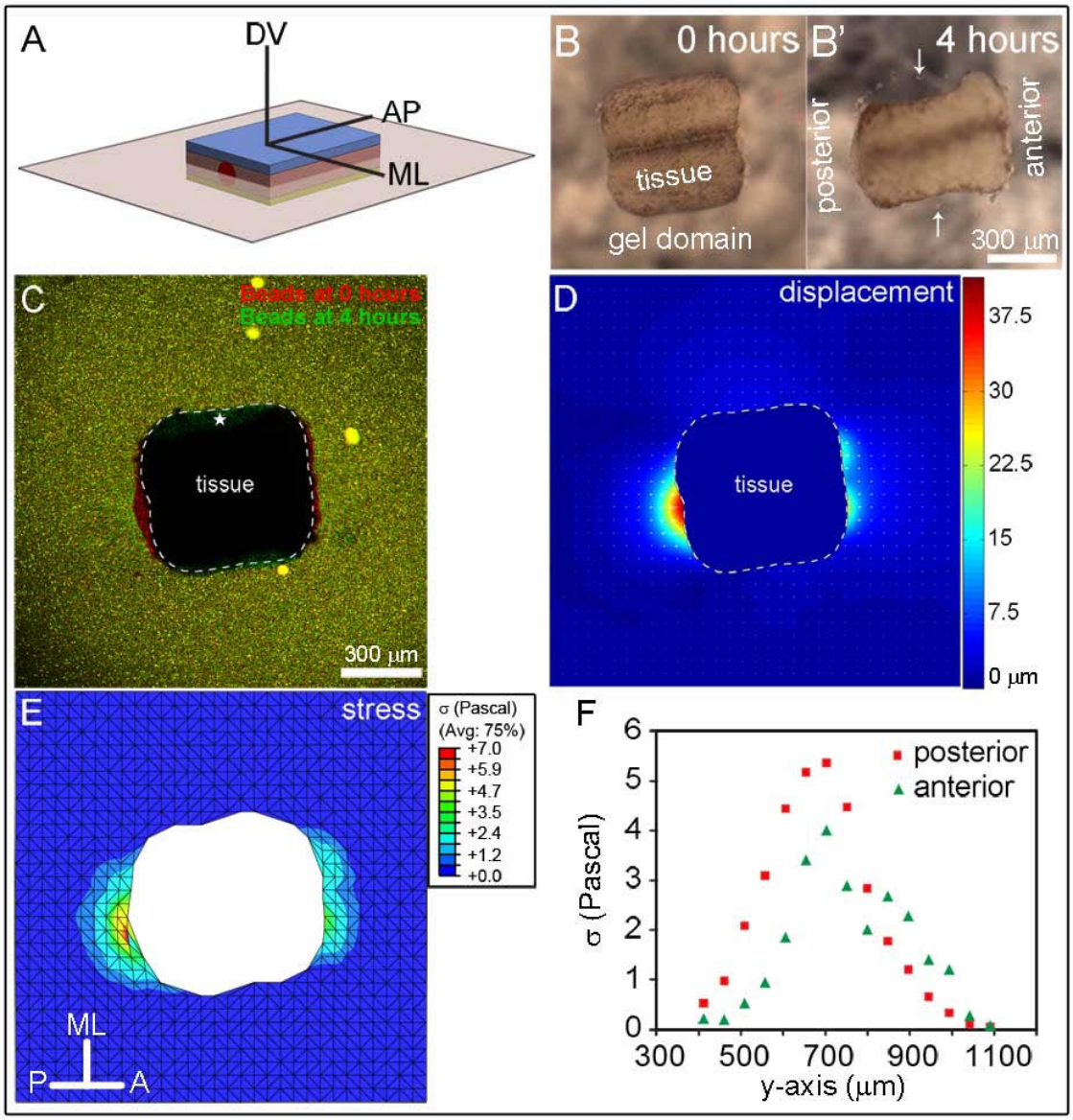

Figure 40. Building FE model based on tracking groups of beads.

(A) Elongating dorsal isolate is positioned in agarose gel with the mediolateral (ML) axis and anterior-posterior (AP) axis aligned with the plane of the confocal section. (B) Dorsal isolate is embedded in gel (dorsal view) at time 0. B') As tissue converges, it loses contact with the gel along the mediolateral sides of the isolate (arrows). (C) Bead map of "null force" (red) and "force loaded" (green). * Green beads "appear" at 4 hours but are not due to deformation but rather are no longer obscured by converging tissues. (D) Gel deformation is calculated by image registration of the two images in (C). (E) Stress distribution computed using a finite element model shows that the posterior end produces a higher, more axially focused pattern of stress than that of the anterior end (F).

3.2.1.3 Detect forces in three dimensions

Using the gel force sensor, we can also assess the forces produced by tissue thickening (Keller et al., 2008) in dorsal-ventral (DV) axis by simply changing the orientation of the dorsal isolate in gel. Dorsal isolates positioned with their DV axis and AP axis aligned with the plane of the confocal section (**Figure 41A**) allowed us to detect both the tissue elongation forces and dorsal ventral thickening forces (**Figure 41B**). We found that tissue thickening in DV axis produced comparable amount of forces as tissue elongation in AP direction. By checking the displacement map, we found that gel deformation in AP axis caused by tissue elongation was focused along the anterior and posterior axis (**Figure 41C**), while deformation by tissue thickening was located at dorsal and ventral sides (**Figure 41D**). There was no gel displacement along the DV direction at anterior and posterior ends (**Figure 41D**) caused by either tissue elongation or thickening, which suggested that tissue elongation did not induce significant gel deformation in DV direction. Such forces might result from bending of the dorsal isolate. Repositioning the dorsal isolate so the explant's ML and DV axes were aligned with the confocal plane (**Figure 41E**) we measured the tissue thickening forces in the middle of the AP axis (**Figure 41F**).

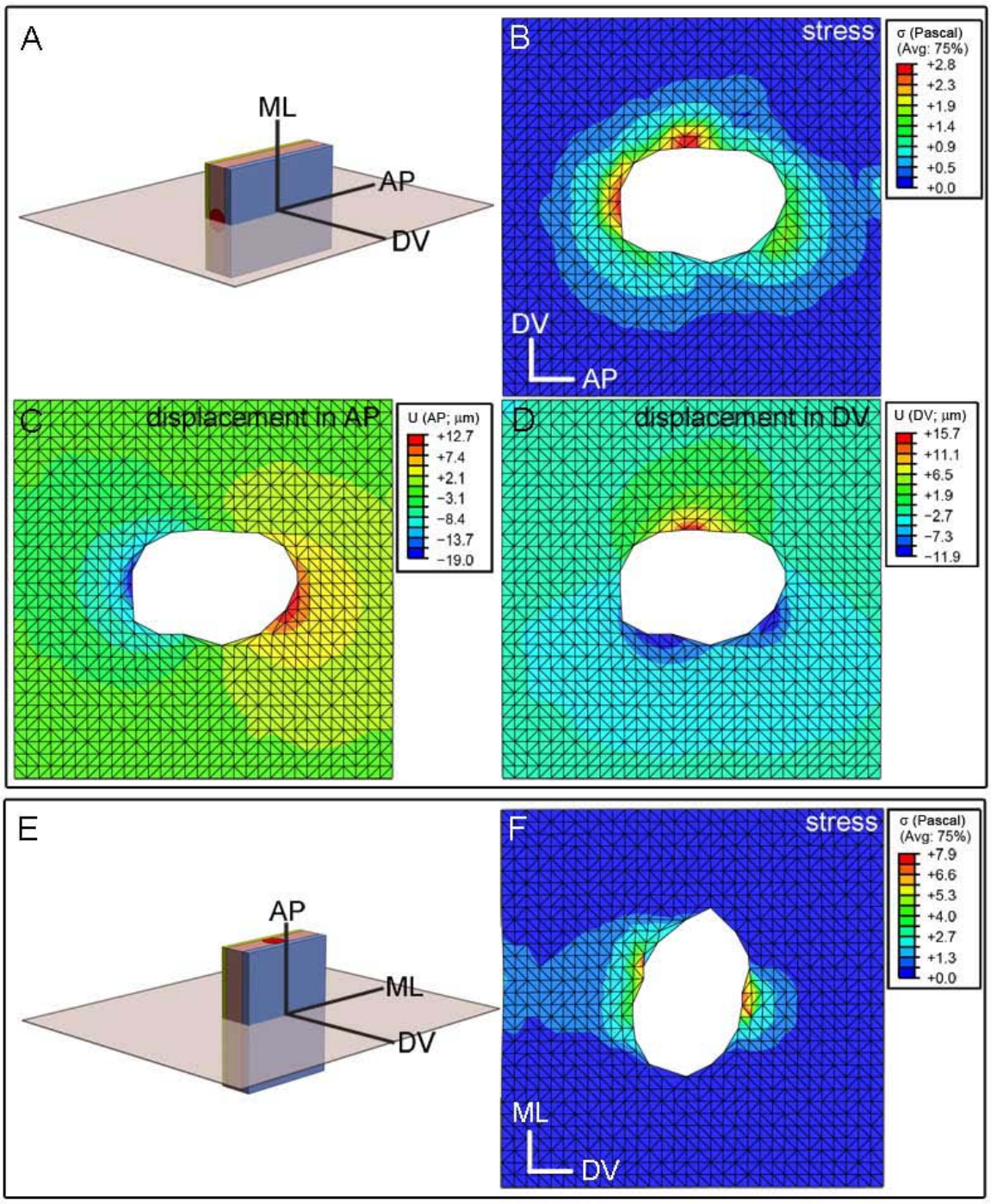

Figure 41. Gel deformation in three-dimensional direction.

(A) Dorsal isolates positioned with their DV axis and AP axis aligned with the plane of the confocal section. (B) Stress produced by both the tissue elongation forces in AP axis and dorsal ventral thickening forces in DV axis. (C) Bead displacement in AP axis caused by tissue elongation is focused along the anterior and posterior axis. (D) Bead

displacement in DV axis caused by tissue thickening is located at dorsal and ventral sides. There is no gel displacement along the DV direction at anterior and posterior ends caused by either tissue elongation or thickening. (E) Dorsal isolates positioned with their DV axis and ML axis aligned with the plane of the confocal section. (F) Stress produced by tissue thickening forces in the middle of the AP axis.

3.2.2 Evaluation of the Gel Force Sensor

In order to measure the small forces generated by embryonic tissue with agarose gels we needed to evaluate the reliability and accuracy of the gel sensor. Since extension forces are determined using the displacement and the material properties of the gel we evaluated the precision of gel sensor to report displacement, strain, and stress.

3.2.2.1 Accuracy of displacement measurements

Several methods can be used to measure displacements in gels. The particle tracking algorithm can resolve sub-pixel movements of beads (Sbalzarini and Koumoutsakos, 2005) and therefore, is able to precisely detect gel displacement. We used particle tracking to evaluate the accuracy of the image registration method by comparing the difference of bead displacements between the two algorithms (**Figure 42A and B**). The difference of bead displacements between the two methods is less than 1 pixel (0.7 μm) in either x- or y-directions (**Figure 42C and D**). The average difference in the reported gel displacement between the two methods is less than 8% and indicates that the image registration detects the gel deformation as well as the particle tracking algorithm.

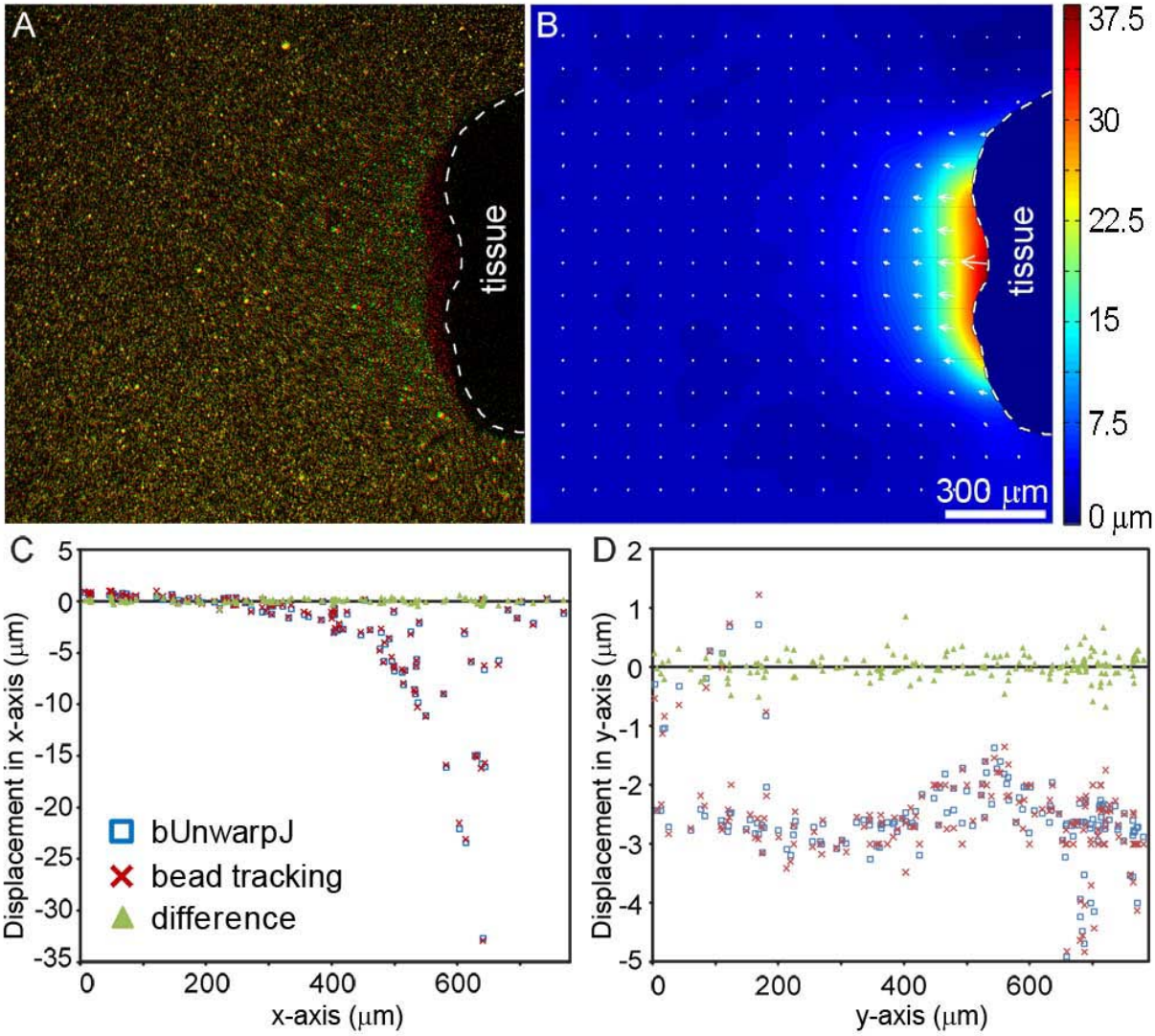

Figure 42.The accuracy of image registration algorithm is verified by the particle tracking algorithm.

(A) The same two images in Figure 39C (red at time 0 and green after 4 hours) were analyzed with image registration algorithm. (B) The absolute displacement calculated by image registration algorithm. (C) The difference of outputs from the image registration and the bead tracking algorithms was less than 0.75 μm in both x- and y-direction (D) and the average difference between the two algorithms is less than 8% for all the beads with more than one pixel movement.

3.2.2.2 Accuracy of strain measurements

Strain in the gel can be calculated directly from the displacement data or can be modeled by finite element methods. To verify the precision of strain measurements reported by the FE model, we directly calculated the nominal strain (NE) by taking the derivative of displacement map produced using image registration. The strain maps from FE model and from direct calculation had similar pattern and the strain values were comparable (**Figure 43A and B**).

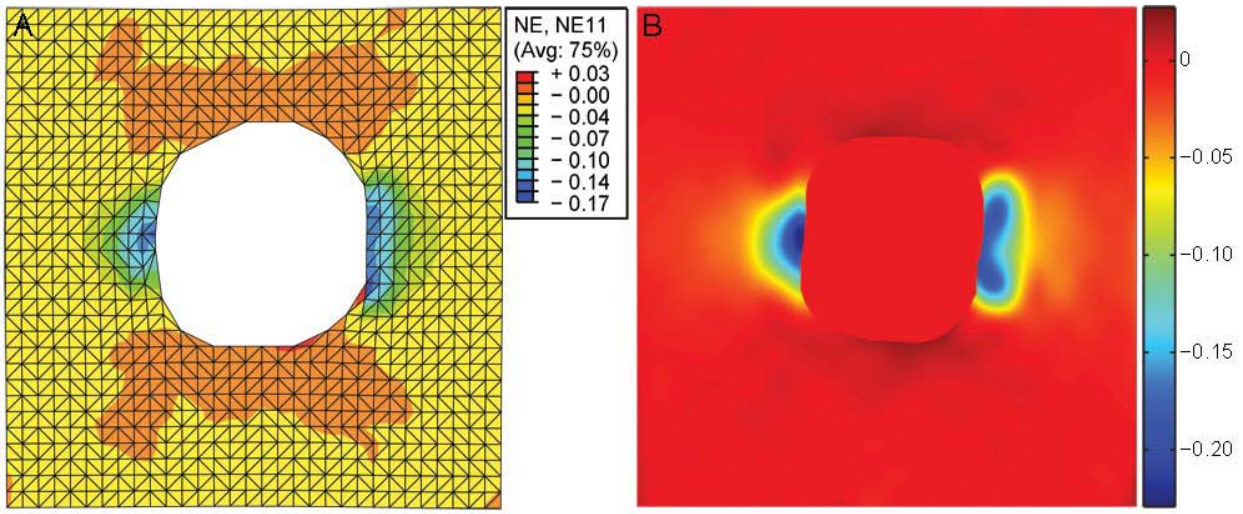

Figure 43.Strain verification by direct computation.

(A) Nominal strain (NE) in anterior-posterior axis (NE11) modeled by finite element (FE) solver. (B) NE11 directly computed from displacement map shows that the strain maps from FE model and from direct calculation had similar pattern.

3.2.2.3 Accuracy of stress measurements

To demonstrate that our technique accurately reports the stress of extending dorsal isolates we carried out three tests. First, we tested our method with microsurgically excised animal cap tissues, which consist of a superficial layer of epithelial cells and a deep layer of mesenchymal

cells. When cultured freely in a dish, animal cap tissues do not converge or extend. When cultured in a gel, animal cap tissues contract and the epithelial cell layer seals up over exposed deep mesenchymal cells in agarose gel (**Figure 44A and B**) and do not generate comparable stress as dorsal isolates (**Figure 44C**). The mean values of maximum von Mises stress produced by animal cap tissues is 0.3 ± 0.1 Pa (n=5), which is much smaller than that of dorsal isolates (5.0 ± 1.6 Pa).

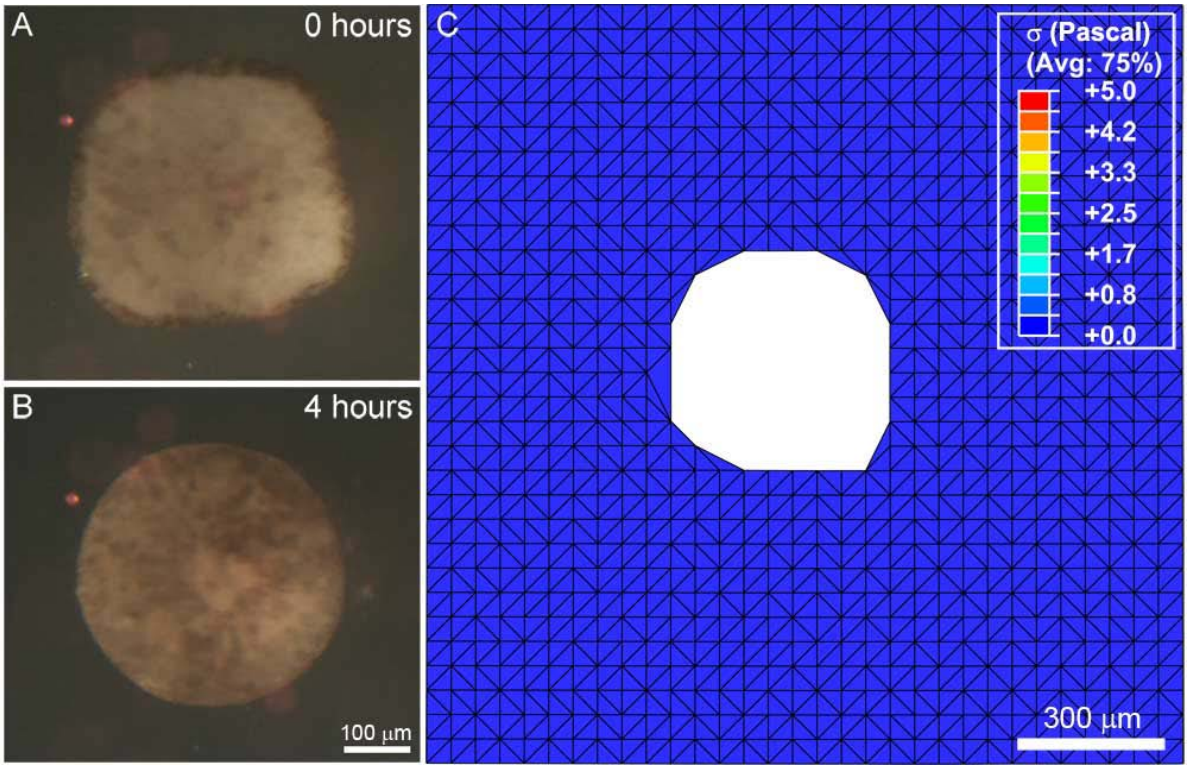

Figure 44. Animal cap tissues do not generate comparable forces.

(A) The embedded animal cap tissue at time 0. (B) Animal cap tissues do not converge or extend, but instead contract and the epithelial cell layer seals up over exposed deep mesenchymal cells after 4 hours. (C) No comparable stress produced by animal cap tissues.

Next, we verified our technique against the well studied case of spherical indentation (**Figure 45A**). By experimentally pushing a sphere with a known diameter into the agarose gel we tested our force-analysis technique against a theoretical prediction of Hertzian contact stress (σ_H) produced by a solid sphere (Hertz, 1881). From gel displacement maps we calculated the stress within the gel (σ_{max}) and compared these values to theoretical predictions ($\sigma_{H,max}$). We found experimentally measured values of σ_{max} were comparable to theoretical values of $\sigma_{H,max}$ even as the indentation forces increased beyond those observed in our studies (**Figure 45B**).

Finally, we compared the gel-measured stresses to the low-throughput measurement of elongation forces using a long optical fiber described in Methods (**Figure 46A**). Dorsal isolates extended along the anterior-posterior axis between an immobile backstage and the optical fiber (**Figure 46B**). The elongating tissue deformed the optical fiber (**Figure 46C**) and produced the maximum force of 0.4 μN (**Figure 46D**) and maximum mean stress of 3.3 Pascal, which is comparable to the maximum mean stress $<\sigma>$ (**Figure 48G**). Thus we have validated our gel-based approach to measure force produced by elongating dorsal isolates at each step of analysis. Thus, embedding *Xenopus* embryonic tissues within a force-reporting agarose gel offers a reliable and high throughput approach to measuring force-production.

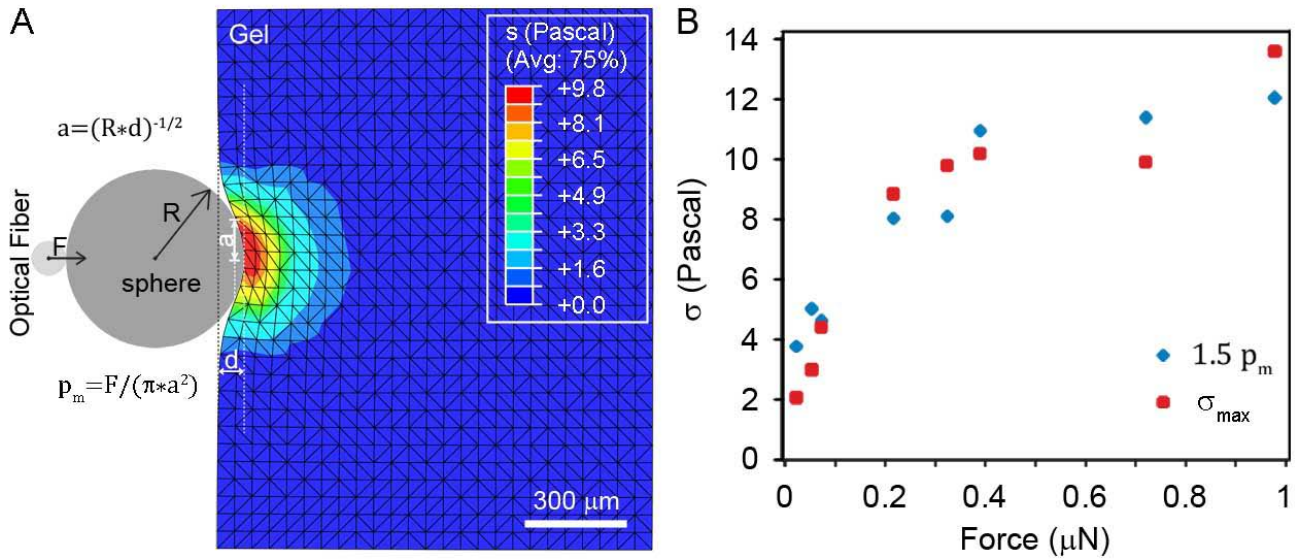

Figure 45. The accuracy of stress is verified by spherical indentation.

(A) A solid sphere with radius (R=250 μm) attached to a optical fiber indented the gel with a half-space surface to depth (d), creating a contact surface with radius (a), and producing stress field in gel domain which is computed by finite element (FE) model. (B) The maximum stresses ($\sigma_{H,max}$) calculated by Hertz contact theory are comparable to maximum Von Mises stresses (σ_{max}) computed from FE model even as the indentation forces increased beyond those observed in our studies.

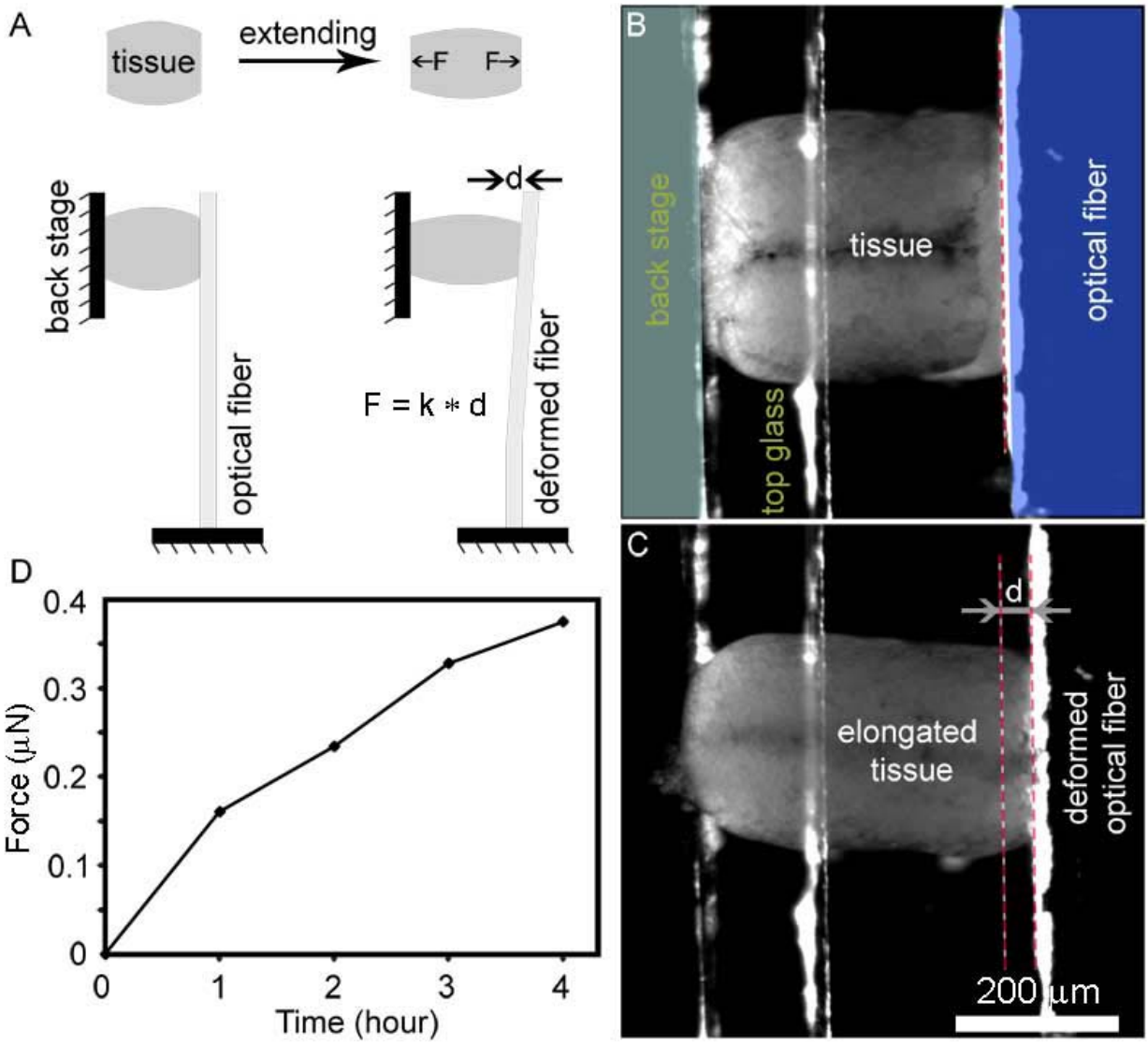

Figure 46. The accuracy of stress is validated by using a long optical fiber.

(A) Sketch of tissue extension without mechanical constrains (top) and sketch of measuring extension forces using a force-reporting optical fiber (below). (B) The tissue is kept between an immobile back stage and a deformable optical fiber at time 0. (C) The elongating tissue deforms the tip of the optical fiber which reported the force. (D) Tissue extension forces measured over 4 hours.

3.2.3 Tissue extending forces regulated by myosin II contractility

With a robust tool to measure force production we investigated the regulation of the tissue extending forces by myosin II contractility. Our previous studies (Zhou et al., 2009) indicated that dorsal isolates were able to elongate approximately 40% over five hours without any physical constraints (**Figure 47A and B**). Interestingly, we found no significant difference of elongation rates between control and myosin inhibitor Y27632-treated tissues (**Figure 47B**), although Y27632 has previously been demonstrated to greatly reduce the tissue stiffness (Zhou et al., 2009). However, when Y27632 treated tissues were embedded in agarose gel, their elongation rate was significantly reduced (**Figure 47A and B**) and they produced much less stress in both anterior and posterior ends (**Figure 47C and D**). The mean value of σ_{max} of control and Y27632 treated tissues was 5.0 ± 1.6 Pa and 1.4 ± 0.7 Pa, respectively. Both the σ_{max} and mean von Mises stress ($<\sigma>$) of Y27632 treated tissues were significantly lower than those of control explants (**Figure 47E-G**). Dorsal isolates incubated in Y27632 exhibited both reduced tissue stiffness and reduced tissue elongation forces, suggesting that embryonic tissues are able to adjust force production to compensate for their internally altered mechanical properties.

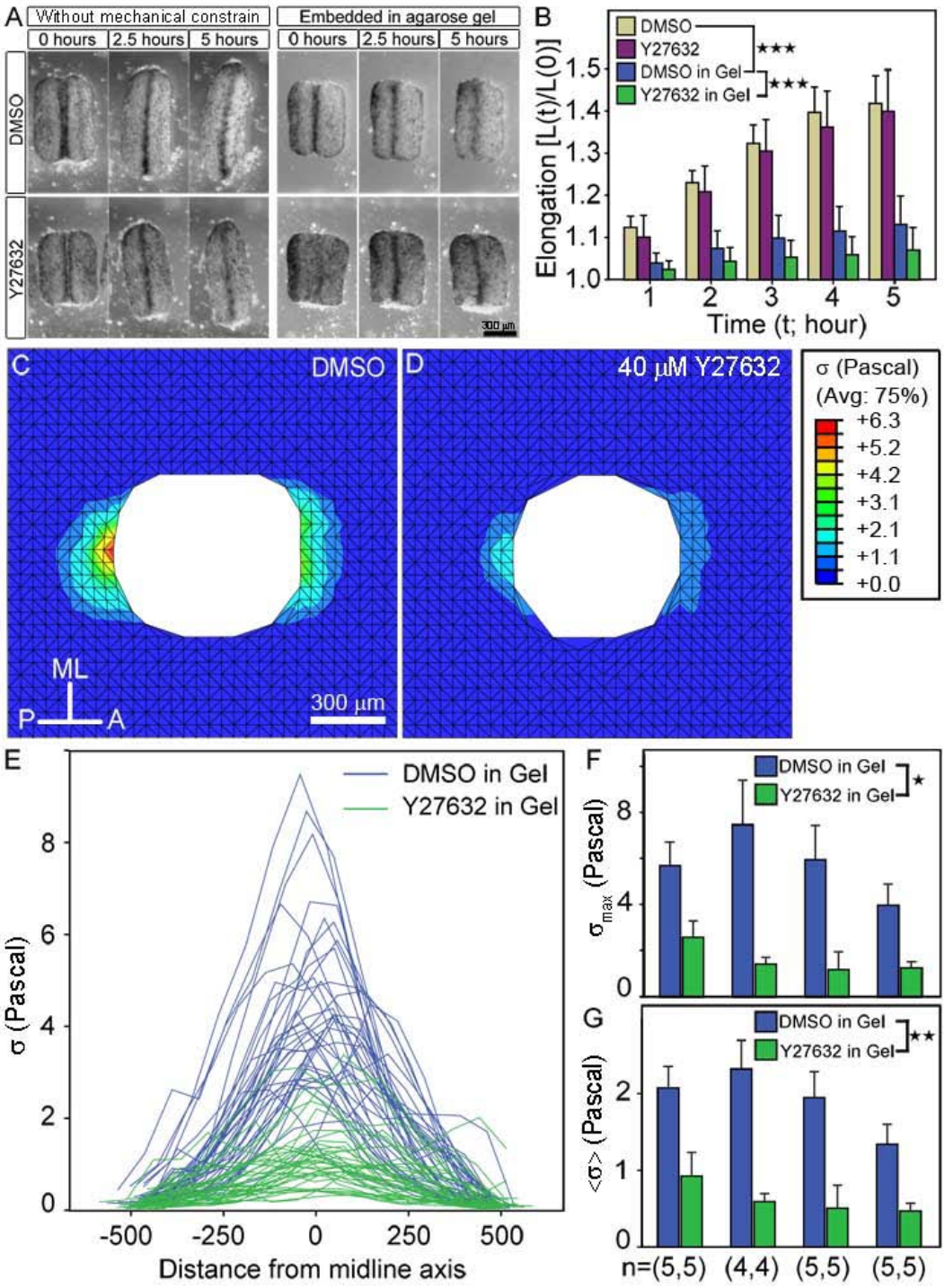

Figure 47. Tissue extension forces are regulated by myosin II contractility.

(A) Dorsal isolates elongate in DMSO and 40 μM Y27632 without mechanical constrain or embedding in agarose gel. (B) Tissues elongate at same rates in DMSO or Y27632 without mechanical constrain, while elongate much less in Y27632 when embedded in gel. (C) Stress field surrounding a tissue in DMSO and a tissue treated with

Y27632 (D) over 4 hours. (E) Stress distribution along the midline axis of the DMSO and Y27632-treated tissues. (F) Both the maximum stress and mean stress (G) of the extending tissues in DMSO were significantly greater than those of tissues in Y27632. Significance of stress measurements among multiple clutches were calculated using two-way ANOVA (*, $p< 0.05$; **, $p< 0.01$; ***, $p<0.005$).

3.2.4 Dorsal isolates in stiffer gel produced greater force

To test whether embryonic tissues could adjust their force production to compensate for external changed mechanical environment, we challenged dorsal isolates with stiffer environment. Our gel-based force sensor allows us to easily change the mechanical environment by simply altering the concentration of agarose gels. To determine the effects of mechanical environment on the force production of dorsal isolates, we measured force production by explants embedded in gels made with three different concentrations 0.6%, 0.9% and 1.2%, whose long-term elastic modulus were typically 30, 200, and 500 Pa, respectively. We found that dorsal isolates embedded in 0.9% or 1.2% gel generated greater forces than those embedded in 0.6% gel (**Figure 48A-C**). Both the σ_{max} and $<\sigma>$ produced by dorsal isolates in 0.6% gel were significantly lower than those in 0.9% or 1.2% gel (**Figure 48E-G**). Comparisons between the elongation forces produced in 0.9% and 1.2% gel are challenging since 1.2% gels introduce higher background "noise" due to inaccuracies in measuring small gel displacements. Thus, the dorsal isolate can adapt of differing mechanical environment; generating larger forces when faced with a stiffer microenvironment.

Since dorsal isolates confined in gels do not elongate we wondered whether the internal architecture of axial and paraxial tissues were altered and could account for unusually high force production. To check the architecture of dorsal isolates for irregular development, we fixed

unconfined and gel-bound explants, stained explants for fibronectin fibrils, and confocal sectioned the intact dorsal isolates. The projections of fibronectin fibrils in confocal stacks show boundaries between germ layers and that tissues embedded in stiffer gels had wider, "knob-shaped" notochords in their posterior ends and the notochords were curved in stiff gels (**Figure 48A'- C'**) compared to dorsal isolates cultured without mechanical restriction (**Figure 48D**). Our findings corroborate previous observations that notochord and somatic tissues actively shear and that the notochord moves, or is drawn toward the posterior end of paraxial mesoderm (Keller et al., 1992a; Wilson et al., 1989). Other tissue morphogenesis, including somite formation and neural tube closure, are not perturbed in gel-confined explants.

3.2.5 Notochords do not contribute to force production

The presence of the notochord knob at the posterior end of a dorsal isolate cultured in a stiff gel suggests that notochord extrusion at the posterior end induces the asymmetric stress patterns at the anterior and posterior end of elongating dorsal isolates and suggests that the notochord may contribute to force production. To test the contribution of notochords to active force generation, we compared the forces produced by `sham-operated' control dorsal isolates and dorsal isolates lacking a notochord. The sham-operated control and notochord-less dorsal isolates (**Figure 49A**) were microsurgically prepared as described previously (chapter 2, section 2) and their architectures were confirmed by confocal sections of stained fibronectin fibrils (**Figure 49B' and C'**). We found that notochord-less dorsal isolates embedded in 30 Pa gel generated a similar magnitude and pattern of force to that generated by sham control dorsal isolates (**Figure 49B and C**). The mean value of σ_{max} produced by sham control and notochord-less dorsal isolates was 4.5 ± 1.1 Pa and 4.1 ± 1.7 Pa, respectively (**Figure 49D**). Furthermore, there are no

significant difference between either both the σ_{max} or $<\sigma>$ produced by sham control and notochord-less dorsal isolates (**Figure 49E and F**). However, due to the effects of microsurgery, both sham control and notochord-less dorsal isolates generated less forces compared to wide-type control dorsal isolates, whose mean value of σ_{max} was 5.9 ± 1.7 Pa (13 notochord-less and 18 wide-type control explants from four clutches, data not shown). Thus, the notochord is unlikely to contribute to the magnitude and patterning of the forces driving tissue elongation during late gastrulation and early neurulation.

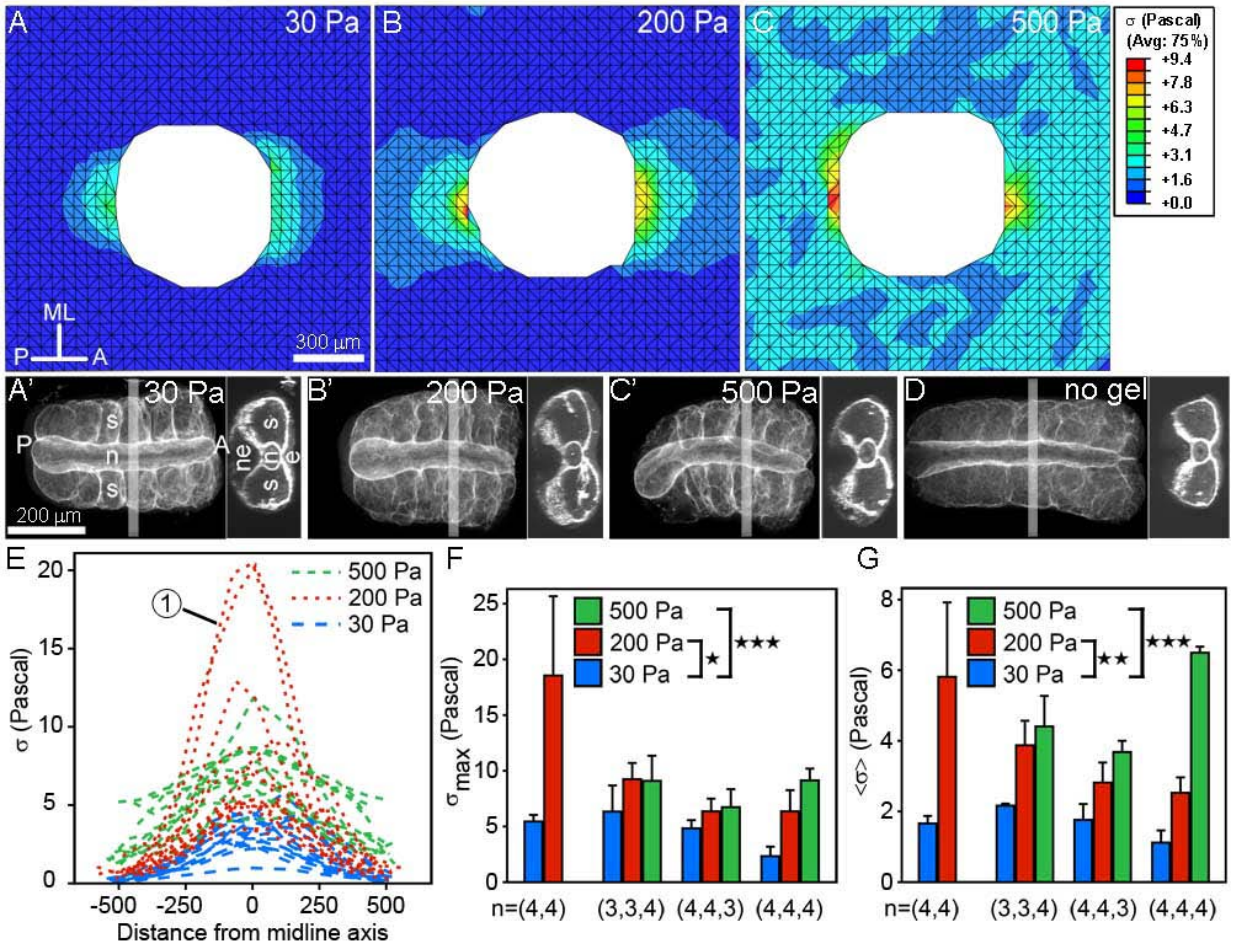

Figure 48. Dorsal isolates in stiffer gel produced greater force.

(A) Dorsal isolates are embedded in 30 Pascal (Pa), in 200 Pa (B), and in 500 Pa gel (C). A') Representative average projections and transverse maximum projections of fibronectin fibrils in confocal stacks taken from tissues embedded in 30 Pa, in 200 Pa (B'), in 500 Pa gel (C'), and in DMSO without mechanical constrains (D) show that tissues had wider, "knob-shaped" notochords in their posterior ends and the notochords are curved in stiff gels. (E) Stress distribution along the midline axis of dorsal isolates embedded in gels with different elastic modulus. ①: note, high stresses from a single clutch. (F) Both the maximum stress and mean stress (G) of the dorsal isolates in 30 Pa gel are significantly less than those of tissues in 200 Pa or 500 Pa gels. Significance of stress measurements among multiple clutches were calculated using two-way ANOVA (*, $p< 0.05$; **, $p< 0.01$; ***, $p<0.005$).

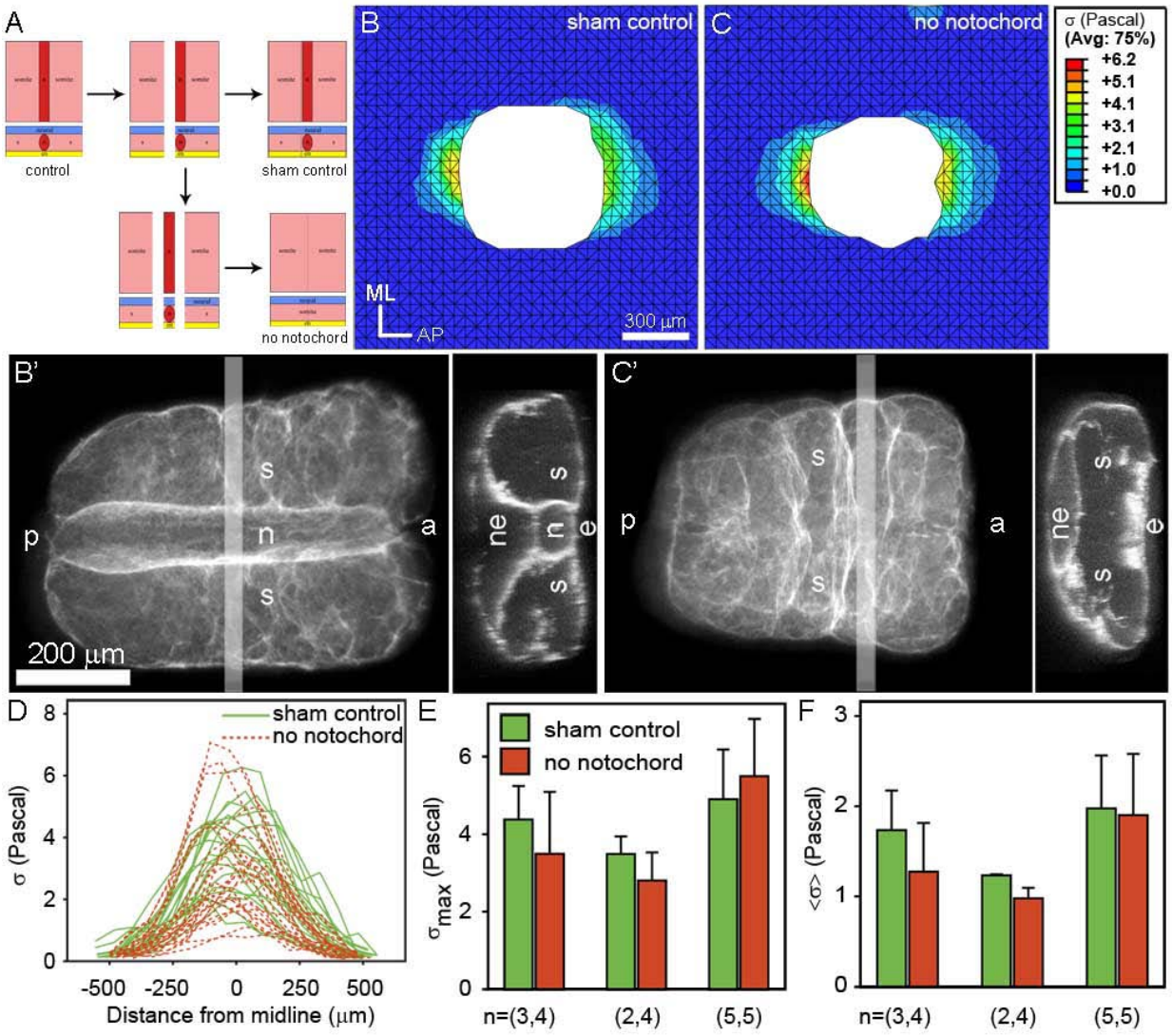

Figure 49. Contribution of the notochord to force production.

(A) Schematic shows `sham-operated' control dorsal isolates and notochord-less dorsal isolates. (B) Stress maps of sham control and notochord-less dorsal isolates (C) embedded in 30 Pa gels. (B') Representative average projections and transverse maximum projections of confocal sections of stained fibronectin fibrils of sham control and no-notochord dorsal isolates (C') show that the sham control dorsal isolate contains neural ectoderm (ne), notochord (n), paraxial somitic mesoderm (s) and endoderm (e), while the notochord-less dorsal isolate does not have notochord (p, posterior and a, anterior). (D) Stress distribution along the midline axis of sham control and notochord-less dorsal tissues. (E) Both the maximum and mean stress (F) of the sham control and notochord-less dorsal isolates are not significantly different. Significance of stress measurements among multiple clutches were calculated using two-way ANOVA (*, $p< 0.05$; **, $p< 0.01$; ***, $p<0.005$).

3.3 DISCUSSION

In this chapter, we developed a high throughput technique to reliable measure the tissue extension forces and used this technique to reveal the hidden changes in force production during convergent extension. The decreased or increased force production balances the reduction in tissue stiffness or balance the increase in the stiffness of external environment, respectively, to allow the tissues to have constant degree of deformation, which indicated that convergent extension movements were robust to physical forces and tissue stiffness. These results suggest how mechanical process maintains the same growth rate from embryo to embryo even as there is large variation in their stiffness and in their force production.

3.3.1 High throughput technique

We developed an innovative high throughput method to reliably measure the extension forces of embryonic dorsal isolates. We tested and validated the accuracy of the method by evaluating the precision of the displacement, strain, and stress measurements. The new method had several advantages over the existing methods. First, the agarose gel holds the tissue without slipping as the tissue extends and changes its shape. Second, it is a high throughput technique which allows us to measure the mechanical forces of more than ten explants at the same time. Third, the agarose gel force sensor is easily adapted to evaluate the stress or strain in different ranges by tuning the elastic modulus of the agarose gel by changing gel concentration. Although the method is designed to measure uniaxial elongating forces of dorsal tissues, it would also be applied to study other tissue types, for example, from developing organs in mammalian embryos or growing tumors, which extend in single or multiple dimensions.

We applied the new technique to measure the extending force produced by dorsal isolates. Both dorsal isolates and animal cap tissues were able to grow normally when they were embedded in gels. Dorsal isolates generated stresses of 5.0 ± 1.6 Pa on the surrounding gel, while animal cap tissue explants generated stresses of 0.3 ± 0.1 Pa, which is almost negligible. Although anterior and posterior ends of dorsal isolates must generate the same total force, the posterior end produced slightly larger stress than that of anterior end due to the smaller cross-section area of posterior end at contact (Keller et al., 1992a; Wilson et al., 1989).

3.3.2 Mechanical environment provided feedback to tissue extension forces

Our results suggest feedback mechanisms operate during development to allow robust morphogenetic movements in the face of variation in physical mechanics, eg. stiffness and force production, of the early embryo. Previous studies showed that embryos successfully completed gastrulation and neurulation even when there was a two-fold variance among embryonic tissue stiffness (von Dassow and Davidson, 2009), or when tissue stiffness was significantly decreased experimentally by inhibiting myosin II contractility (Zhou et al., 2009). Here, by examining the tissue extending forces, we found that the variance in tissue force production was comparable to that in tissue stiffness (**Figure 47E**). Moreover, we found that the extending forces of dorsal isolates were significantly decreased when myosin II contractility was reduced by Y27632. Our results support the idea that force production and tissue stiffness are highly coordinated during early development.

How can embryos develop normally against a background of mechanical variation that must inevitably arise due to genetic and environmental variation in real populations? Do feed-back mechanisms operate through high-level control of gene expression or is feedback

maintained at the level of the cytoskeleton? Many possible routes for mechanotransduction or mechanical feedback have been observed in cultured cells (Schwartz and DeSimone, 2008) but it is still unknown how the active force production and passive mechanical properties are coordinated in embryos.

3.3.3 An approach with broad applications

The technique developed here enables analysis of convergent extension movements of embryonic dorsal tissues and also offers promise to understand other instances of force generation during morphogenesis, organogenesis, and tumor growth. For example, the technique could be directly used to investigate the elongation forces produced by ventral embryonic tissues during neurula and tailbud stages (Drawbridge and Steinberg, 2000; Larkin and Danilchik, 1999). With minor modification, our technique could also be applied to study the forces driving the neural tube formation, an important morphogenesis movement (Nagele et al., 1989; Sadler, 1998). Micropatterning approach has been developed to study tissue deformation such as branch morphogenesis by creating cavites in Polydimethylsiloxane (PDMS) to mimic the mammary epithelial tubules (Mori et al., 2009; Nelson et al., 2008; Nelson et al., 2006). However, no direct force measurement is avaible in these studies. By tracking fluorensce beads added in the PDMS, our technique could be adapted to estimate the temporospatial stress patterns induced by these tissues. Lastly, by embedding tumor tissues in gels with appropriate ECM such as collagen, we could measure the growth forces of expanding tumors to study the tumour invasion and metastasis.

3.3.4 Limitation

There are several limitations of our current version of gel force sensor. First, due to the technique difficulties, we were unable to determine the gel deformation in three dimensions neither by tracking individual beads nor by tracking groups of beads, which makes it hard to model the tissue extending movements in three dimensions using our finite element models. Second, we measured the maximum forces produced by stalled explants and were not able to estimate the rate of force generation during convergent and extension.

4.0 SUMMARY AND CONCLUSIONS

4.1 SUMMARY OF FINDINGS

We addressed three specific aims to study the passive mechanical properties and active force generation capacities of frog embryonic tissues. In chapter 2, we addressed aim 1 to characterize the temporal and spatial variation of tissue stiffness in dorsal isolates. By measuring the stiffness of dorsal isolates from different stages and the stiffness of dorsal explants with their sub-components iteratively removed, we found large temporal and spatial variance in tissue mechanics. Dorsal isolates increase 6-fold in stiffness within several hours. Pre-somitic mesoderm, but not notochord, supports the dorsal part of early embryos. Endoderm tissues are the least stiff component in dorsal explants and dependent on other dorsal parts to maintain their structures.

In section 2.2.2 and 2.2.3, we addressed aim 2 to evaluate the contribution of subcellular and cellular structures to embryonic tissue stiffness. We found the passive mechanical properties of dorsal isolates were determined by thousands of closely compacted individual cells, but not their surrounding extracellular matrix. Using small molecule inhibitors we found the mechanical properties of these cells largely depended on the actin cytoskeleton and myosin II contractility, while microtubules did not mechanically contribute to the tissue mechanics, but regulated tissue stiffness by altering actomyosin contractility through a RhoGEF mediated signaling pathway.

In chapter 3, we addressed aim 3 to investigate how mechanical environment affects forces generated by dorsal isolates. By estimating the active force production using a newly developed gel force reporting sensor, we found that passive and active tissue mechanics are coordinated through actomyosin contractility. Reducing the myosin II contractility decreased both tissue stiffness and extending forces, which allow the embryonic tissues to have robust convergent extension movements. The mechanical environment provided feedbacks to the force production machines to generate larger forces in stiffer environments.

4.2 SIGNIFICANCE OF THE FINDINGS

By finishing these three aims, we revealed several key principles in the mechanical design of vertebrate embryonic tissues during late gastrulation and early neurulation and resolved several hypotheses about the mechanical process of embryonic development.

First, we found that paraxial mesoderm rather than notochord played an important role providing the mechanical support for early embryos. The failure in axial elongation may cause severe neural tube defects in vertebrates including humans (Kibar et al., 2007; Wallingford et al., 2002). Based on our studies, we suggest to further investigate the mechanical roles of paraxial mesoderm in neural tube closure, since it is the paraxial mesoderm who determines the physical resistance and perhaps the force generation of the dorsal tissues during axial elongation and neural tube closure.

Second, ECM is typically treated as a simple scaffold that mechanically supports tissues or organs but is now recognized to affect multiple cellular processes (Daley et al., 2008) and several tissue movements such as convergent extension, somite formation, branch

morphogenesis in vertebrates through signaling pathways (Darribere and Schwarzbauer, 2000; Davidson et al., 2004; Davidson et al., 2006; George et al., 1993; Georges-Labouesse et al., 1996; Julich et al., 2009; Koshida et al., 2005; Larsen et al., 2006; Sakai et al., 2003; Yang et al., 1999). However, these earlier studies suggested a wide range of mechanical functions for the ECM including mechanical support and protection. Our studies ruled out the contribution of ECM to tissue mechanics in early frog embryonic tissues and suggested that ECM may only play signaling role in these early developmental stages. In contrast, ECM does contribute to the tissue mechanics in late stages such as tail-bud stage, during which collagen sheath increased internal tension in notochord field and thus straighten the whole dorsal embryo (Adams et al., 1990; Koehl et al., 2000). Combined with these studies, our results demonstrate how tightly ECM must be regulated both temporally and spatially. These findings suggest that tissue engineers should reconsider their designs of extracellular matrix scaffolds to allow more temporally and spatially controlled mechanical properties to mimic the mechanical environment in native ECM. For instance, decellularized native matrix may provide a promising scaffold to build artificial hearts (Ott et al., 2008). The decellularization process keeps the intact three-dimensional geometry and fiber architecture, while still changes the mechanical properties of the matrix (Liao et al., 2008; Ott et al., 2008). Thus, there is still a long way to go to make commercial matrix scaffolds (Place et al., 2009) and studies from developmental biology are essential to define what is the best matrix to design (Ingber and Levin, 2007).

Third, surprisingly, we demonstrated that microtubules did not mechanically contribute to tissue stiffness, but rather molecularly regulate the tissue stiffness. Microtubules are involved in many cellular processes (Akhmanova et al., 2009) and tissue movements (Brun and Garson, 1983; Karfunkel, 1971; Kwan and Kirschner, 2005; Nakaya et al., 2008; Rodriguez et al., 2003; Solnica-Krezel and Driever, 1994). For the first time, we showed that disruption of microtubules

could increase tissue stiffness as a result of increase in actomyosin contractility. Our studies provide a new perspective that requires us to re-think the role of microtubules in tissue movement. For example, reducing microtubules may increase tissue stiffness, which may cause severe defects in morphogenetic development such as mammalian neurulation (Copp et al., 2003).

Fourth, we revealed that actomyosin contractility controlled both passive mechanical properties and active force production to maintain a "balance" between driving forces and resistance to allow the robust convergent extension movements. Actomyosin contractility has been shown to mediate multiple tissue movements such as apical constriction, neural tube closure, mesoderm invagination, and convergent extension in *Xenopus lavis*, *zebrafish*, *Drosophila*, and in mice (Fernandez-Gonzalez et al., 2009; Martin, in Press). In most cases, actomyosin contractility was studied as the driving forces to the cellular or tissue movements, without concern for the role of actomyosin in establishing or maintaining tissue stiffness. Furthermore the contribution of actomyosin contractility to passive tissue mechanical properties was rarely examined due to the difficulties in measuring the passive tissue mechanics in species such as *zebrafish* and *Drosophila.* However, our studies remind us that tissue deformation is dominated by both active force and passive tissue mechanics. Thus the spatial and temporal regulation of tissue stiffness revealed in our frog *Xenopus lavis* model could provide valuable information to investigate the tissue movement in human embryos and other model systems since the genetic and biochemical regulation of tissue mechanical properties is common to all animal cells or tissues.

4.3 FUTURE DIRECTIONS

We demonstrated the temporal and spatial variation in tissue stiffness and showed that cytoskeletal components, such as F-actin, myosin II motors, microtubules regulate the tissue mechanics. However, we did not detect significance difference of F-actin and phosphorylated myosin II protein expression in time and space. Future studies are needed to reveal what mediates the temporospatial variation presented in tissue stiffness. In order to investigate the contribution of molecular- and cellular-structures to tissue stiffness, we applied a panel of drugs to manipulate the subcellular structures such as disrupting intermediate filament with acrylamide, inhibiting myosin II function with blebbistatin, or activating myosin II contractility with calyculin A and increasing actin polymerization with jasplakinolide. These drugs are not very specific and there are numerous avenues for future studies. We showed that inhibiting actomyosin contractility by Y27632 decrease the tissue stiffness, but did not induce defects in axial elongation or embryonic developments. However, other studies have showen that know-down myosin IIB significantly reduced tissue stiffness and disrupted the convergent extension movements (Rolo et al., 2009; Skoglund et al., 2008). The discrepancy suggested that myosin heavy chains and light regulatory chains had distinct effects on tissue mechanics and tissue movements and future studies are needed to explore the role of myosin motors in morphogenetic movements. By investigating the contribution of actomyosin contractility to both tissue stiffness and elongating forces, we found that actomyosin contractility regulates the two processes simultaneously, which makes the convergent extension movements robust to the tissue mechanics. However, we did not yet reveal how actomyosin contractility is able to regulate the two processes at the same time and keep the constant ratio between the two parameters in different conditions. We only can postulate that cellular traction forces control both the tissue

elongating force and tissue stiffness and thus reducing traction forces decreases force and stiffness, or it is possible that there is feedback between force and stiffness and so force (or stiffness) could modulate the other process. Microtubules regulate multiple cellular processes in addition to tissue stiffness. Mechanical rescue the tissue stiffness did not fully recover the embryonic development and axial elongation, which suggests that other cellular processes that microtubules involve are also important to convergent extension movements. More experiments are needed to study the roles of microtubules playing in tissue deformation such as microtubules mediated cell polarity or cell shape changes.

APPENDIX A

REGULATION OF TISSUE STIFFNESS BY MOLECULE STRUCTURES

Targets	Treatment	Treatment time	Tissue stiffness	p-value
Cadherin	control		46.6±8.3 (n=8)	0.001
	Catenin Binding Region-glucocorticoid receptor (CBR-GR, 14 ng per embryo)		24.0±6.4 (n=8)	
F-actin	control	1 hour	49.3±10.4 (n=9)	0.222
	1 uM Jasplakinolide (Jasp)		54.4±8.8 (n=9)	
	control	1 hour	47.7±6.7(n=8)	0.072
	2 uM Jasp		53.2±4.9 (n=7)	
	control	40 minutes	43.8±9.6 (n=8)	0.161
	3 uM Jasp		37.5±5.5 (n=8)	
	control	1 hour	72.5±8.6 (n=9)	0.001
	10 uM Jasp		55.3±8.6 (n=9)	
	0.6 uM Latrunculin B (LatB)	20 minutes	34.8±7.3 (n=8)	0.036
	LatB+1uM Jasp		42.8±6.4 (n=9)	
Myosin II	control	30 minutes	50.1±12.1 (n=8)	0.888
	40 nM Calyculin A (CalyA)		50.9±8.2 (n=9)	
	40 uM Y27632	30 minutes	30.0±3.9 (n=9)	0.011
	Y27632+40 nM CalyA		38.8±7.5 (n=9)	
	40 uM Y27632	30 minutes	30.7±4.1(n=9)	0.003
	Y27632+60 nM CalyA		39.0±5.1(n=9)	
Microtubule	50 uM Nocodazole (Noco)	40 minutes	118.2±19.0 (n=8)	0.000
	Noco+0.6 μM LatB		41.7±23.1 (n=7)	
Fibrillin fibrils	control		55.0±8.6 (n=8)	0.721
	Fibrillin Morpholino (10 μM per embryo)		58.1±11.7(n=8)	

APPENDIX B

ABAQUS INPUT FILE

The following is a sample ABAQUS input file named sample.inp. The node, element, Elset, Nset, boundary condition sections have been shortened to save space.

```
*Heading
** Job name: sample Model name: sample
*Preprint, echo=NO, model=NO, history=NO, contact=NO
** PARTS
*Part, name=PART-1
*Node
      1,   24.2187004,   24.2187004
      2,   24.2187004,   72.6561966
      ..............................
    873,    1525.7793,   1477.34192
    874,    1525.7793,    1525.7793
*Element, type=CPS3
   1,   1, 33,   2
   2,   2, 33,  34
   ................
1621, 731, 763, 732
1622, 446, 427, 445
*Elset, elset=_PICKEDSET3, internal
```

```
    1,    2,    3,    4,    5,    6,    7,    8,    9,   10,   11,
    12,   13,   14,   15,   16,   17,   18,   19,   20,   21,   22,
    ..........................................................
    1594, 1595, 1596, 1597, 1598, 1599, 1600, 1601, 1602, 1603, 1604,
    1605, 1606, 1607, 1608, 1609, 1610, 1611, 1612, 1613, 1614, 1615,
** Section: Section-1-_PICKEDSET3
*Solid Section, elset=_PICKEDSET3, material=VISCOELASTIC
1.,
*End Part
** ASSEMBLY
*Assembly, name=Assembly
*Instance, name=PART-1-1, part=PART-1
*End Instance
*Nset, nset=_PICKEDSET1, internal, instance=PART-1-1
 1,
*Nset, nset=_PICKEDSET2, internal, instance=PART-1-1
 2,
 ..................................................
*Nset, nset=_PICKEDSET873, internal, instance=PART-1-1
 873,
*Nset, nset=_PICKEDSET874, internal, instance=PART-1-1
 874,
*End Assembly
** MATERIALS
*Material, name=VISCOELASTIC
*Elastic, moduli=INSTANTANEOUS
 25.965, 0.5
*Viscoelastic, time=PRONY
  0.0922,    0., 0.046
 0.10298,    0., 0.634
** ----------------------------------------------------------------
```

```
** STEP: Step-1
*Step, name=Step-1, nlgeom=YES, inc=3000
*Visco, cetol=0.0001
480., 14400., 0.144, 14400.
** BOUNDARY CONDITIONS
** Name: Disp-BC-1 Type: Displacement/Rotation
*Boundary
_PICKEDSET1, 1, 1, 1.0116
** Name: Disp-BC-2 Type: Displacement/Rotation
*Boundary
_PICKEDSET1, 2, 2, 0.3087
.....
** Name: Disp-BC-1747 Type: Displacement/Rotation
*Boundary
_PICKEDSET874, 1, 1, 0.4537
** Name: Disp-BC-1748 Type: Displacement/Rotation
*Boundary
_PICKEDSET874, 2, 2, -1.3685
*End Step
```

BIBLIOGRAPHY

ABAQUS. (2007). Abaqus Theory Manual, (version 6.7).

Adams, D. S., Keller, R. and Koehl, M. A. (1990). The mechanics of notochord elongation, straightening and stiffening in the embryo of Xenopus laevis. *Development* **110**, 115-30.

Akhmanova, A., Stehbens, S. J. and Yap, A. S. (2009). Touch, Grasp, Deliver and Control: Functional Cross-Talk Between Microtubules and Cell Adhesions. *Traffic* **10**, 268-274.

Alberts, B., Johnson, A., Lewis, J., Raff, M., Roberts, K. and Walter, P. (2008). Molecular Biology of the Cell. New York: Garland Science.

Amano, M., Ito, M., Kimura, K., Fukata, Y., Chihara, K., Nakano, T., Matsuura, Y. and Kaibuchi, K. (1996). Phosphorylation and activation of myosin by Rho-associated kinase (Rho-kinase). *J Biol Chem* **271**, 20246-9.

Ananthakrishnan, R., Guck, J., Wottawah, F., Schinkinger, S., Lincoln, B., Romeyke, M., Moon, T. and Kas, J. (2006). Quantifying the contribution of actin networks to the elastic strength of fibroblasts. *J Theor Biol* **242**, 502-16.

Arthur, W. T., Noren, N. K. and Burridge, K. (2002). Regulation of Rho family GTPases by cell-cell and cell-matrix adhesion. *Biol Res* **35**, 239-46.

Balgude, A. P., Yu, X., Szymanski, A. and Bellamkonda, R. V. (2001). Agarose gel stiffness determines rate of DRG neurite extension in 3D cultures. *Biomaterials* **22**, 1077-84.

Benko, R. and Brodland, G. W. (2007). Measurement of in vivo stress resultants in neurulation-stage amphibian embryos. *Ann Biomed Eng* **35**, 672-81.

Birkenfeld, J., Nalbant, P., Bohl, B. P., Pertz, O., Hahn, K. M. and Bokoch, G. M. (2007). GEF-H1 modulates localized RhoA activation during cytokinesis under the control of mitotic kinases. *Dev Cell* **12**, 699-712.

Blystone, S. D. (2004). Integrating an integrin: a direct route to actin. *Biochim Biophys Acta* **1692**, 47-54.

Botto, L. D., Moore, C. A., Khoury, M. J. and Erickson, J. D. (1999). Neural-tube defects. *N Engl J Med* **341**, 1509-19.

Brand-Saberi, B. and Christ, B. (2000). Evolution and development of distinct cell lineages derived from somites. *Curr Top Dev Biol* **48**, 1-42.

Brooke, B. S., Karnik, S. K. and Li, D. Y. (2003). Extracellular matrix in vascular morphogenesis and disease: structure versus signal. *Trends Cell Biol* **13**, 51-6.

Brozovich, F. V. (2002). Myosin light chain phosphatase: it gets around. *Circ Res* **90**, 500-2.

Brun, R. B. and Garson, J. A. (1983). Neurulation in the Mexican salamander (Ambystoma mexicanum): a drug study and cell shape analysis of the epidermis and the neural plate. *J Embryol Exp Morphol* **74**, 275-95.

Bubb, M. R., Senderowicz, A. M., Sausville, E. A., Duncan, K. L. and Korn, E. D. (1994). Jasplakinolide, a cytotoxic natural product, induces actin polymerization and competitively inhibits the binding of phalloidin to F-actin. *J Biol Chem* **269**, 14869-71.

Bubb, M. R., Spector, I., Beyer, B. B. and Fosen, K. M. (2000). Effects of jasplakinolide on the kinetics of actin polymerization. An explanation for certain in vivo observations. *J Biol Chem* **275**, 5163-70.

Chang, Y. C., Nalbant, P., Birkenfeld, J., Chang, Z. F. and Bokoch, G. M. (2008). GEF-H1 Couples Nocodazole-induced Microtubule Disassembly to Cell Contractility via RhoA. *Mol Biol Cell* **19**, 2147-53.

Chen, Q., Suki, B. and An, K. N. (2004). Dynamic mechanical properties of agarose gels modeled by a fractional derivative model. *J Biomech Eng* **126**, 666-71.

Chimini, G. and Chavrier, P. (2000). Function of Rho family proteins in actin dynamics during phagocytosis and engulfment. *Nat Cell Biol* **2**, E191-6.

Christensen, R. M. (1991). Mechanics of Composite Materials. Malabar, Florida: Krieger Publishing Company.

Collinsworth, A. M., Zhang, S., Kraus, W. E. and Truskey, G. A. (2002). Apparent elastic modulus and hysteresis of skeletal muscle cells throughout differentiation. *Am J Physiol Cell Physiol* **283**, C1219-27.

Colognato, H. and Yurchenco, P. D. (2000). Form and function: the laminin family of heterotrimers. *Dev Dyn* **218**, 213-34.

Copp, A. J., Greene, N. D. and Murdoch, J. N. (2003). The genetic basis of mammalian neurulation. *Nat Rev Genet* **4**, 784-93.

Coulombe, P. A., Bousquet, O., Ma, L., Yamada, S. and Wirtz, D. (2000). The 'ins' and 'outs' of intermediate filament organization. *Trends Cell Biol* **10**, 420-8.

Daley, W. P., Peters, S. B. and Larsen, M. (2008). Extracellular matrix dynamics in development and regenerative medicine. *J Cell Sci* **121**, 255-264.

Danowski, B. A. (1989). Fibroblast contractility and actin organization are stimulated by microtubule inhibitors. *J Cell Sci* **93 (Pt 2)**, 255-66.

Darribere, T. and Schwarzbauer, J. E. (2000). Fibronectin matrix composition and organization can regulate cell migration during amphibian development. *Mechanisms of Development* **92**, 239-250.

Davidson, L. and Keller, R. (2007). Measuring mechanical properties of embryos and embryonic tissues. *Methods Cell Biol* **83**, 425-39.

Davidson, L., von Dassow, M. and Zhou, J. (2009a). Multi-scale mechanics from molecules to morphogenesis. *Int J Biochem Cell Biol*.

Davidson, L. A., Dzamba, B. D., Keller, R. and Desimone, D. W. (2008). Live imaging of cell protrusive activity, and extracellular matrix assembly and remodeling during morphogenesis in the frog, Xenopus laevis. *Dev Dyn* **237**, 2684 - 2692.

Davidson, L. A., Keller, R. and DeSimone, D. W. (2004). Assembly and remodeling of the fibrillar fibronectin extracellular matrix during gastrulation and neurulation in Xenopus laevis. *Dev Dyn* **231**, 888-95.

Davidson, L. A., Marsden, M., Keller, R. and DeSimone, D. W. (2006). Integrin [alpha]5[beta]1 and Fibronectin Regulate Polarized Cell Protrusions Required for Xenopus Convergence and Extension. *Current Biology* **16**, 833-844.

Davidson, L. A., Oster, G. F., Keller, R. E. and Koehl, M. A. (1999). Measurements of mechanical properties of the blastula wall reveal which hypothesized mechanisms of primary invagination are physically plausible in the sea urchin Strongylocentrotus purpuratus. *Dev Biol* **209**, 221-38.

Davidson, L. A., Von Dassow, M. and Zhou, J. (2009b). Multi-scale mechanics from molecules to morphogenesis. *International Journal of Biochemistry and Cell Biology*.

Desprat, N., Supatto, W., Pouille, P. A., Beaurepaire, E. and Farge, E. (2008). Tissue deformation modulates twist expression to determine anterior midgut differentiation in Drosophila embryos. *Dev Cell* **15**, 470-7.

Discher, D. E., Janmey, P. and Wang, Y. L. (2005). Tissue cells feel and respond to the stiffness of their substrate. *Science* **310**, 1139-43.

Drawbridge, J. and Steinberg, M. S. (2000). Elongation of axolotl tailbud embryos requires GPI-linked proteins and organizer-induced, active, ventral trunk endoderm cell rearrangements. *Dev Biol* **223**, 27-37.

Elul, T. and Keller, R. (2000). Monopolar protrusive activity: a new morphogenic cell behavior in the neural plate dependent on vertical interactions with the mesoderm in Xenopus. *Dev Biol* **224**, 3-19.

Elul, T., Koehl, M. A. and Keller, R. (1997). Cellular mechanism underlying neural convergent extension in Xenopus laevis embryos. *Dev Biol* **191**, 243-58.

Engler, A. J., Carag-Krieger, C., Johnson, C. P., Raab, M., Tang, H.-Y., Speicher, D. W., Sanger, J. W., Sanger, J. M. and Discher, D. E. (2008). Embryonic cardiomyocytes beat best on a matrix with heart-like elasticity: scar-like rigidity inhibits beating. *J Cell Sci*, jcs.029678.

Engler, A. J., Sen, S., Sweeney, H. L. and Discher, D. E. (2006). Matrix elasticity directs stem cell lineage specification. *Cell* **126**, 677-89.

Enomoto, T. (1996). Microtubule disruption induces the formation of actin stress fibers and focal adhesions in cultured cells: possible involvement of the rho signal cascade. *Cell Struct Funct* **21**, 317-26.

Espeseth, A., Marnellos, G. and Kintner, C. (1998). The role of F-cadherin in localizing cells during neural tube formation in Xenopus embryos. *Development* **125**, 301-12.

Esue, O., Carson, A. A., Tseng, Y. and Wirtz, D. (2006). A direct interaction between actin and vimentin filaments mediated by the tail domain of vimentin. *J Biol Chem* **281**, 30393-9.

Farge, E. (2003). Mechanical induction of Twist in the Drosophila foregut/stomodeal primordium. *Curr Biol* **13**, 1365-77.

Fernandez-Gonzalez, R., Simoes, S. d. M., Rer, J.-C., Eaton, S. and Zallen, J. A. (2009). Myosin II Dynamics Are Regulated by Tension in Intercalating Cells. **17**, 736-743.

Fey, J. and Hausen, P. (1990). Appearance and distribution of laminin during development of Xenopus laevis. *Differentiation* **42**, 144-52.

Findley, W. N., Lai, J. S. and Onaran, K. (1989). Creep and relaxation of nonlinear viscoelastic materials. New York: Dover Publications, Inc.

Fischer-Cripps, A. C. (2007). Introduction to Contact Mechanics. *New York: Springer.*

Forgacs, G., Foty, R. A., Shafrir, Y. and Steinberg, M. S. (1998). Viscoelastic properties of living embryonic tissues: a quantitative study. *Biophys J* **74**, 2227-34.

Gardel, M. L., Kasza, K. E., Brangwynne, C. P., Liu, J. and Weitz, D. A. (2008). Chapter 19: Mechanical response of cytoskeletal networks. *Methods Cell Biol* **89**, 487-519.

Gardel, M. L., Nakamura, F., Hartwig, J. H., Crocker, J. C., Stossel, T. P. and Weitz, D. A. (2006). Prestressed F-actin networks cross-linked by hinged filamins replicate mechanical properties of cells. *Proc Natl Acad Sci U S A* **103**, 1762-7.

Gardel, M. L., Shin, J. H., MacKintosh, F. C., Mahadevan, L., Matsudaira, P. and Weitz, D. A. (2004). Elastic behavior of cross-linked and bundled actin networks. *Science* **304**, 1301-5.

George, E., Georges-Labouesse, E., Patel-King, R., Rayburn, H. and Hynes, R. (1993). Defects in mesoderm, neural tube and vascular development in mouse embryos lacking fibronectin. *Development* **119**, 1079-1091.

Georges-Labouesse, E. N., George, E. L., Rayburn, H. and Hynes, R. O. (1996). Mesodermal development in mouse embryos mutant for fibronectin. *Developmental Dynamics* **207**, 145-156.

Ghosh, K. and Ingber, D. E. (2007). Micromechanical control of cell and tissue development: implications for tissue engineering. *Adv Drug Deliv Rev* **59**, 1306-18.

Gibson, L. J. and Ashby, M. F. (1988). Cellular solids: structure and properties. New York: Pergamon Press.

Gibson, L. J. and Ashby, M. F. (1997). Cellular solids: structure and properties. New York: Cambridge University Press.

Gilbert, S. F. (2006). Developmental Biology. Sunderland: Sinauer Associates, Inc.

Gordon, V. D., Valentine, M. T., Gardel, M. L., Andor-Ardo, D., Dennison, S., Bogdanov, A. A., Weitz, D. A. and Deisboeck, T. S. (2003). Measuring the mechanical stress induced by an expanding multicellular tumor system: a case study. *Exp Cell Res* **289**, 58-66.

Gumbiner, B. M. (2005). Coordinate Gene Regulation by Two Different Catenins. *Developmental Cell* **8**, 795-796.

Habas, R., Dawid, I. B. and He, X. (2003). Coactivation of Rac and Rho by Wnt/Frizzled signaling is required for vertebrate gastrulation. *Genes Dev.* **17**, 295-309.

Herrmann, H., Bar, H., Kreplak, L., Strelkov, S. V. and Aebi, U. (2007). Intermediate filaments: from cell architecture to nanomechanics. *Nat Rev Mol Cell Biol* **8**, 562-73.

Hertz, H. (1881). "On the contact of elastic solids". *J.Reine Angew. Math.* **92**, pp.156-171.

Hopwood, N. D., Pluck, A. and Gurdon, J. B. (1989). MyoD expression in the forming somites is an early response to mesoderm induction in Xenopus embryos. *EMBO J* **8**, 3409-17.

Hutton, E., Paladini, R. D., Yu, Q. C., Yen, M., Coulombe, P. A. and Fuchs, E. (1998). Functional differences between keratins of stratified and simple epithelia. *J Cell Biol* **143**, 487-99.

Ingber, D. E. (2003). Tensegrity I. Cell structure and hierarchical systems biology. *J Cell Sci* **116**, 1157-73.

Ingber, D. E. (2006). Cellular mechanotransduction: putting all the pieces together again. *FASEB J.* **20**, 811-827.

Ingber, D. E. and Levin, M. (2007). What lies at the interface of regenerative medicine and developmental biology? *Development* **134**, 2541-7.

Ishihara, H., Martin, B. L., Brautigan, D. L., Karaki, H., Ozaki, H., Kato, Y., Fusetani, N., Watabe, S., Hashimoto, K., Uemura, D. et al. (1989). Calyculin A and okadaic acid: inhibitors of protein phosphatase activity. *Biochem Biophys Res Commun* **159**, 871-7.

Jacobson, A. G. and Gordon, R. (1976). Changes in the shape of the developing vertebrate nervous system analyzed experimentally, mathematically, and by computer simulation. *Journal of Experimental Zoology* **197**, 191-246.

Janmey, P. A., Euteneuer, U., Traub, P. and Schliwa, M. (1991). Viscoelastic properties of vimentin compared with other filamentous biopolymer networks. *J Cell Biol* **113**, 155-60.

Janmey, P. A. and McCulloch, C. A. (2007). Cell mechanics: integrating cell responses to mechanical stimuli. *Annu Rev Biomed Eng* **9**, 1-34.

Joshi, S. D., von Dassow, M. and Davidson, L. A. (2009). Experimental control of excitable embryonic tissues: three stimuli induce rapid epithelial contraction. *Exp Cell Res*.

Julich, D., Mould, A. P., Koper, E. and Holley, S. A. (2009). Control of extracellular matrix assembly along tissue boundaries via Integrin and Eph/Ephrin signaling. *Development* **136**, 2913-2921.

Kaibuchi, K., Kuroda, S. and Amano, M. (1999). Regulation of the cytoskeleton and cell adhesion by the Rho family GTPases in mammalian cells. *Annu Rev Biochem* **68**, 459-86.

Kao, K. R., Masui, Y. and Elinson, R. P. (1986). Lithium-induced respecification of pattern in Xenopus laevis embryos. *Nature* **322**, 371-373.

Karfunkel, P. (1971). The role of microtubules and microfilaments in neurulation in Xenopus. *Dev Biol* **25**, 30-56.

Karfunkel, P. (1972). The activity of microtubules and microfilaments in neurulation in the chick. *J Exp Zool* **181**, 289-301.

Katsumi, A., Milanini, J., Kiosses, W. B., del Pozo, M. A., Kaunas, R., Chien, S., Hahn, K. M. and Schwartz, M. A. (2002). Effects of cell tension on the small GTPase Rac. *J Cell Biol* **158**, 153-64.

Kay, B. K. and Peng, H. B. (1991). *Xenopus laevis*: practical uses in cell and molecular biology. New York: Academic Press.

Keller, H. U., Naef, A. and Zimmermann, A. (1984). Effects of colchicine, vinblastine and nocodazole on polarity, motility, chemotaxis and cAMP levels of human polymorphonuclear leukocytes. *Exp Cell Res* **153**, 173-85.

Keller, R. (2000). The origin and morphogenesis of amphibian somites. *Curr Top Dev Biol* **47**, 183-246.

Keller, R. (2002). Shaping the vertebrate body plan by polarized embryonic cell movements. *Science* **298**, 1950-4.

Keller, R., Cooper, M. S., Danilchik, M., Tibbetts, P. and Wilson, P. A. (1989). Cell intercalation during notochord development in Xenopus laevis. *Journal of Experimental Zoology* **251(2)**, 134-54.

Keller, R., Davidson, L., Edlund, A., Elul, T., Ezin, M., Shook, D. and Skoglund, P. (2000a). Mechanisms of convergence and extension by cell intercalation. *Philos Trans R Soc Lond B Biol Sci* **355**, 897-922.

Keller, R., Davidson, L., Edlund, A., Elul, T., Ezin, M., Shook, D. and Skoglund, P. (2000b). Mechanisms of convergence and extension by cell intercalation. *Phil. Trans. R. Soc. Lond. B* **355**, 897-922.

Keller, R., Davidson, L. A. and Shook, D. R. (2003). How we are shaped: the biomechanics of gastrulation. *Differentiation* **71**, 171-205.

Keller, R. and Shih, J. (1992). Mediolateral intercalation of mesodermal cells in the xenopus-laevis gastrula.

Keller, R., Shih, J. and Domingo, C. (1992a). The patterning and functioning of protrusive activity during convergence and extension of the Xenopus organizer. *Development (supplement)*, 81-91.

Keller, R., Shih, J. and Sater, A. (1992b). The cellular basis of the convergence and extension of the Xenopus neural plate. *Developmental Dynamics* **193(3)**, 199-217.

Keller, R., Shook, D. and Skoglund, P. (2008). The forces that shape embryos: physical aspects of convergent extension by cell intercalation. *Phys Biol* **5**, 15007.

Kibar, Z., Capra, V. and Gros, P. (2007). Toward understanding the genetic basis of neural tube defects. *Clin Genet* **71**, 295-310.

Kidoaki, S., Matsuda, T. and Yoshikawa, K. (2006). Relationship between apical membrane elasticity and stress fiber organization in fibroblasts analyzed by fluorescence and atomic force microscopy. *Biomech Model Mechanobiol* **5**, 263-72.

Kinsey, R., Williamson, M. R., Chaudhry, S., Mellody, K. T., McGovern, A., Takahashi, S., Shuttleworth, C. A. and Kielty, C. M. (2008). Fibrillin-1 microfibril deposition is dependent on fibronectin assembly. *J Cell Sci* **121**, 2696-704.

Kintner, C. (1992). Regulation of embryonic cell adhesion by the cadherin cytoplasmic domain. *Cell* **69**, 225-36.

Kitchin, I. C. (1949). The effects of notochordectomy in Amblystoma mexicanum. *J Exp Zool* **112**, 393-415.

Klymkowsky, M. W. (1995). Intermediate filaments: new proteins, some answers, more questions. *Curr Opin Cell Biol* **7**, 46-54.

Klymkowsky, M. W., Maynell, L. A. and Polson, A. G. (1987). Polar asymmetry in the organization of the cortical cytokeratin system of Xenopus laevis oocytes and embryos. *Development* **100**, 543-57.

Klymkowsky, M. W., Shook, D. R. and Maynell, L. A. (1992). Evidence that the deep keratin filament systems of the Xenopus embryo act to ensure normal gastrulation. *Proc Natl Acad Sci U S A* **89**, 8736-40.

Koehl, M. A. R., Adams, D. S. and Keller, R. E. (1990). Mechanical development of the notochord in *Xenopus* early tail-bud embryos. In *Biomechanics of active movement and deformation.*, vol. H 42 (ed. N. Akkas), pp. 471-485. Berlin Heidelberg: Springer-Verlag.

Koehl, M. A. R., Quillin, K. J. and Pell, C. A. (2000). Mechanical design of fiber-wound hydraulic skeletons: The stiffening and straightening of embryonic notochords. *American Zoologist* **40**, 28-41.

Kofron, M., Heasman, J., Lang, S. A. and Wylie, C. C. (2002). Plakoglobin is required for maintenance of the cortical actin skeleton in early Xenopus embryos and for cdc42-mediated wound healing. *J Cell Biol* **158**, 695-708.

Kolm, P. J. and Sive, H. L. (1995). Efficient hormone-inducible protein function in Xenopus laevis. *Dev Biol* **171**, 267-72.

Koshida, S., Kishimoto, Y., Ustumi, H., Shimizu, T., Furutani-Seiki, M., Kondoh, H. and Takada, S. (2005). Integrin[alpha]5-Dependent Fibronectin Accumulation for Maintenance of Somite Boundaries in Zebrafish Embryos. *Developmental Cell* **8**, 587-598.

Krendel, M., Zenke, F. T. and Bokoch, G. M. (2002). Nucleotide exchange factor GEF-H1 mediates cross-talk between microtubules and the actin cytoskeleton. *Nat Cell Biol* **4**, 294-301.

Krieg, M., Arboleda-Estudillo, Y., Puech, P. H., Kafer, J., Graner, F., Muller, D. J. and Heisenberg, C. P. (2008). Tensile forces govern germ-layer organization in zebrafish. *Nat Cell Biol* **10**, 429-36.

Kwan, K. M. and Kirschner, M. W. (2005). A microtubule-binding Rho-GEF controls cell morphology during convergent extension of Xenopus laevis. *Development* **132**, 4599-610.

Lane, M. C. and Keller, R. (1997). Microtubule disruption reveals that Spemann's organizer is subdivided into two domains by the vegetal alignment zone. *Development* **124**, 895-906.

Larkin, K. and Danilchik, M. V. (1999). Ventral cell rearrangements contribute to anterior-posterior axis lengthening between neurula and tailbud stages in Xenopus laevis. *Dev Biol* **216**, 550-60.

Larsen, M., Wei, C. and Yamada, K. M. (2006). Cell and fibronectin dynamics during branching morphogenesis. *J Cell Sci* **119**, 3376-84.

Lee, C. H. and Gumbiner, B. M. (1995). Disruption of gastrulation movements in Xenopus by a dominant-negative mutant for C-cadherin. *Dev Biol* **171**, 363-73.

Lee, J. S., Hale, C. M., Panorchan, P., Khatau, S. B., George, J. P., Tseng, Y., Stewart, C. L., Hodzic, D. and Wirtz, D. (2007). Nuclear lamin A/C deficiency induces defects in cell mechanics, polarization, and migration. *Biophys J* **93**, 2542-52.

Lee, J. Y. and Harland, R. M. (2007). Actomyosin contractility and microtubules drive apical constriction in Xenopus bottle cells. *Dev Biol* **311**, 40-52.

Levental, I., Georges, P. C. and Janmey, P. A. (2007). Soft biological materials and their impact on cell function. *Soft Matter* **3**, 299-306.

Levental, K. R., Yu, H., Kass, L., Lakins, J. N., Egeblad, M., Erler, J. T., Fong, S. F., Csiszar, K., Giaccia, A., Weninger, W. et al. (2009). Matrix crosslinking forces tumor progression by enhancing integrin signaling. *Cell* **139**, 891-906.

Liao, J., Joyce, E. M. and Sacks, M. S. (2008). Effects of decellularization on the mechanical and structural properties of the porcine aortic valve leaflet. *Biomaterials* **29**, 1065-1074.

Liao, J., Yang, L., Grashow, J. and Sacks, M. S. (2007). The relation between collagen fibril kinematics and mechanical properties in the mitral valve anterior leaflet. *J Biomech Eng* **129**, 78-87.

Lo, C. M., Wang, H. B., Dembo, M. and Wang, Y. L. (2000). Cell movement is guided by the rigidity of the substrate. *Biophysical Journal* **79**, 144-152.

Lodish, H. M., P. Berk, A. Ploegh, P. Scott, M. (2007). Molecular Cell Biology: W. H. Freeman Company.

Machesky, L. M. and Hall, A. (1997). Role of actin polymerization and adhesion to extracellular matrix in Rac- and Rho-induced cytoskeletal reorganization. *J Cell Biol* **138**, 913-26.

Malacinski, G. M. and Youn, B. W. (1981). Neural plate morphogenesis and axial stretching in "notochord-defective" Xenopus laevis embryos. *Dev Biol* **88**, 352-7.

Marsden, M. and DeSimone, D. W. (2001). Regulation of cell polarity, radial intercalation and epiboly in Xenopus: novel roles for integrin and fibronectin. *Development* **128**, 3635-47.

Marsden, M. and DeSimone, D. W. (2003). Integrin-ECM interactions regulate cadherin-dependent cell adhesion and are required for convergent extension in Xenopus. *Curr Biol* **13**, 1182-91.

Martens, J. C. and Radmacher, M. (2008). Softening of the actin cytoskeleton by inhibition of myosin II. *Pflugers Arch* **456**, 95-100.

Martin, A. C. (in Press). Pulsation and stabilization: Contractile forces that underlie morphogenesis *Developmental Biology*.

Millard, T. H., Sharp, S. J. and Machesky, L. M. (2004). Signalling to actin assembly via the WASP (Wiskott-Aldrich syndrome protein)-family proteins and the Arp2/3 complex. *Biochem J* **380**, 1-17.

Moore, S. W. (1994). A fiber optic system for measuring dynamic mechanical properties of embryonic tissues. *IEEE Trans Biomed Eng* **41**, 45-50.

Moore, S. W., Keller, R. E. and Koehl, M. A. (1995). The dorsal involuting marginal zone stiffens anisotropically during its convergent extension in the gastrula of Xenopus laevis. *Development* **121**, 3131-40.

Mori, H., Gjorevski, N., Inman, J. L., Bissell, M. J. and Nelson, C. M. (2009). Self-organization of engineered epithelial tubules by differential cellular motility. *Proc Natl Acad Sci U S A* **106**, 14890-5.

Nagayama, M., Haga, H., Takahashi, M., Saitoh, T. and Kawabata, K. (2004). Contribution of cellular contractility to spatial and temporal variations in cellular stiffness. *Exp Cell Res* **300**, 396-405.

Nagele, R. G., Bush, K. T., Kosciuk, M. C., Hunter, E. T., Steinberg, A. B. and Lee, H. Y. (1989). Intrinsic and extrinsic factors collaborate to generate driving forces for neural tube formation in the chick: a study using morphometry and computerized three-dimensional reconstruction. *Brain Res Dev Brain Res* **50**, 101-11.

Nakaya, Y., Sukowati, E. W., Wu, Y. and Sheng, G. (2008). RhoA and microtubule dynamics control cell-basement membrane interaction in EMT during gastrulation. *Nat Cell Biol* **10**, 765-75.

Nelson, C. M., Inman, J. L. and Bissell, M. J. (2008). Three-dimensional lithographically defined organotypic tissue arrays for quantitative analysis of morphogenesis and neoplastic progression. *Nat Protoc* **3**, 674-8.

Nelson, C. M., VanDuijn, M. M., Inman, J. L., Fletcher, D. A. and Bissell, M. J. (2006). Tissue Geometry Determines Sites of Mammary Branching Morphogenesis in Organotypic Cultures. *Science* **314**, 298-300.

Nieuwkoop, P. D. and Faber, J. (1967). Normal tables of *Xenopus laevis* (Daudin). Amsterdam: Elsevier North-Holland Biomedical Press.

Noren, N. K., Liu, B. P., Burridge, K. and Kreft, B. (2000). P120 Catenin Regulates the Actin Cytoskeleton via Rho Family Gtpases. *J. Cell Biol.* **150**, 567-580.

Normand, V., Lootens, D. L., Amici, E., Plucknett, K. P. and Aymard, P. (2000). New insight into agarose gel mechanical properties. *Biomacromolecules* **1**, 730-8.

Ott, H. C., Matthiesen, T. S., Goh, S. K., Black, L. D., Kren, S. M., Netoff, T. I. and Taylor, D. A. (2008). Perfusion-decellularized matrix: using nature's platform to engineer a bioartificial heart. *Nat Med* **14**, 213-21.

Parsons, M. J., Pollard, S. M., Sade, L., Feldman, B., Coutinho, P., Hirst, E. M. A. and Stemple, D. L. (2002). Zebrafish mutants identify an essential role for laminins in notochord formation. *Development* **129**, 3137-3146.

Paszek, M. J., Zahir, N., Johnson, K. R., Lakins, J. N., Rozenberg, G. I., Gefen, A., Reinhart-King, C. A., Margulies, S. S., Dembo, M., Boettiger, D. et al. (2005). Tensional homeostasis and the malignant phenotype. *Cancer Cell* **8**, 241-54.

Pelham, R. J., Jr. and Wang, Y. (1997). Cell locomotion and focal adhesions are regulated by substrate flexibility. *Proc Natl Acad Sci U S A* **94**, 13661-5.

Peyton, S. R. and Putnam, A. J. (2005). Extracellular matrix rigidity governs smooth muscle cell motility in a biphasic fashion. *J Cell Physiol* **204**, 198-209.

Philip, J. T. and Dahl, K. N. (2008). Nuclear mechanotransduction: response of the lamina to extracellular stress with implications in aging. *J Biomech* **41**, 3164-70.

Place, E. S., Evans, N. D. and Stevens, M. M. (2009). Complexity in biomaterials for tissue engineering. *Nat Mater* **8**, 457-470.

Potard, U. S., Butler, J. P. and Wang, N. (1997). Cytoskeletal mechanics in confluent epithelial cells probed through integrins and E-cadherins. *Am J Physiol Cell Physiol* **272**, C1654-1663.

Ramos, J. W. and DeSimone, D. W. (1996). Xenopus embryonic cell adhesion to fibronectin: position-specific activation of RGD/synergy site-dependent migratory behavior at gastrulation. *J Cell Biol* **134**, 227-40.

Riehl, R., Johnson, K., Bradley, R., Grunwald, G. B., Cornel, E., Lilienbaum, A. and Holt, C. E. (1996). Cadherin function is required for axon outgrowth in retinal ganglion cells in vivo. *Neuron* **17**, 837-48.

Rodriguez, O. C., Schaefer, A. W., Mandato, C. A., Forscher, P., Bement, W. M. and Waterman-Storer, C. M. (2003). Conserved microtubule-actin interactions in cell movement and morphogenesis. *Nat Cell Biol* **5**, 599-609.

Rolo, A., Skoglund, P. and Keller, R. (2009). Morphogenetic movements driving neural tube closure in Xenopus require myosin IIB. *Dev Biol* **327**, 327-38.

Ross, K. A. and Scanlon, M. G. (1999). ANALYSIS OF THE ELASTIC MODULUS OF AGAR GEL BY INDENTATION. *Journal of Texture Studies* **30**, 17-27.

Rotsch, C. and Radmacher, M. (2000). Drug-induced changes of cytoskeletal structure and mechanics in fibroblasts: an atomic force microscopy study. *Biophys J* **78**, 520-35.

Sadler, T. W. (1998). Mechanisms of neural tube closure and defects. *Mental Retardation and Developmental Disabilities Research Reviews* **4**, 247-253.

Sakai, T., Larsen, M. and Yamada, K. M. (2003). Fibronectin requirement in branching morphogenesis. *Nature* **423**, 876-81.

Sater, A. K., Steinhardt, R. A. and Keller, R. (1993). Induction of neuronal differentiation by planar signals in Xenopus embryos. *Dev Dyn* **197**, 268-80.

Sato, M., Theret, D. P., Wheeler, L. T., Ohshima, N. and Nerem, R. M. (1990). Application of the Micropipette Technique to the Measurement of Cultured Porcine Aortic Endothelial Cell Viscoelastic Properties. *Journal of Biomechanical Engineering* **112**, 263-268.

Sbalzarini, I. F. and Koumoutsakos, P. (2005). Feature point tracking and trajectory analysis for video imaging in cell biology. *J Struct Biol* **151**, 182-95.

Scherrer, L. C., Picard, D., Massa, E., Harmon, J. M., Simons, S. S., Jr., Yamamoto, K. R. and Pratt, W. B. (1993). Evidence that the hormone binding domain of steroid receptors confers hormonal control on chimeric proteins by determining their hormone-regulated binding to heat-shock protein 90. *Biochemistry* **32**, 5381-6.

Schiff, P. B. and Horwitz, S. B. (1980). Taxol stabilizes microtubules in mouse fibroblast cells. *Proceedings of the National Academy of Sciences of the United States of America* **77**, 1561-1565.

Schroer, T. A. and Sheetz, M. P. (1991). Functions of microtubule-based motors. *Annu Rev Physiol* **53**, 629-52.

Schwartz, M. A. and DeSimone, D. W. (2008). Cell adhesion receptors in mechanotransduction. *Curr Opin Cell Biol* **20**, 551-6.

Selman, G. G. (1955). Studies on the forces producing neural closure in amphibia. *Proceedings of the Royal Physical Society of Edinburgh* **24**, 24-27.

Selman, G. G. (1958). The forces producing neural closure in amphibia. *Journal of Embryology and Experimental Morphology* **6**, 448-465.

Shih, J. and Keller, R. (1992). Cell motility driving mediolateral intercalation in explants of Xenopus laevis. *Development* **116**, 901-14.

Sive, H. L., Grainger, R. M. and Harland, R. M. (2000). Early development of Xenopus laevis: a laboratory manual., (ed., pp. 338. Cold Spring Harbor, New York: Cold Spring Harbor Laboratory Press.

Skoglund, P., Dzamba, B., Coffman, C. R., Harris, W. A. and Keller, R. (2006). Xenopus fibrillin is expressed in the organizer and is the earliest component of matrix at the developing notochord-somite boundary. *Dev Dyn* **235**, 1974-83.

Skoglund, P. and Keller, R. (2007). Xenopus fibrillin regulates directed convergence and extension. *Dev Biol* **301**, 404-16.

Skoglund, P., Rolo, A., Chen, X., Gumbiner, B. M. and Keller, R. (2008). Convergence and extension at gastrulation require a myosin IIB-dependent cortical actin network. *Development* **135**, 2435-2444.

Sokal, R. R. and Rohlf, F. J. (1994). Biometry. New York: W. H. Freeman and Company.

Solnica-Krezel, L. and Driever, W. (1994). Microtubule arrays of the zebrafish yolk cell: organization and function during epiboly. *Development* **120**, 2443-55.

Somlyo, A. P. and Somlyo, A. V. (2000). Signal transduction by G-proteins, rho-kinase and protein phosphatase to smooth muscle and non-muscle myosin II. *J Physiol* **522 Pt 2**, 177-85.

Sorzano, C. O., Thevenaz, P. and Unser, M. (2005). Elastic registration of biological images using vector-spline regularization. *IEEE Trans Biomed Eng* **52**, 652-63.

Stamenovic, D. (2005a). Effects of cytoskeletal prestress on cell rheological behavior. *Acta Biomater* **1**, 255-62.

Stamenovic, D. (2005b). Microtubules may harden or soften cells, depending of the extent of cell distension. *Journal of Biomechanics* **38**, 1728-1732.

Stamenovic, D., Liang, Z., Chen, J. and Wang, N. (2002). Effect of the cytoskeletal prestress on the mechanical impedance of cultured airway smooth muscle cells. *J Appl Physiol* **92**, 1443-1450.

Stern, C. D. (2004). Gastrulation: From Cells to Embryo. University College London.

Stewart, R. M. and Gerhart, J. C. (1990). The anterior extent of dorsal development of the Xenopus embryonic axis depends on the quantity of organizer in the late blastula. *Development* **109**, 363-72.

Tahinci, E. and Symes, K. (2003). Distinct functions of Rho and Rac are required for convergent extension during Xenopus gastrulation. *Dev Biol* **259**, 318-35.

Takai, E., Costa, K. D., Shaheen, A., Hung, C. T. and Guo, X. E. (2005). Osteoblast elastic modulus measured by atomic force microscopy is substrate dependent. *Ann Biomed Eng* **33**, 963-71.

Takaya, H. (1977). Types of neural tissues induced through the presumptive notochord of newt embryo. *Differentiation* **7**, 187-92.

Talbot, W. S., Trevarrow, B., Halpern, M. E., Melby, A. E., Farr, G., Postlethwait, J. H., Jowett, T., Kimmel, C. B. and Kimelman, D. (1995). A homeobox gene essential for zebrafish notochord development. *Nature* **378**, 150-7.

Tan, J. L., Ravid, S. and Spudich, J. A. (1992). Control of nonmuscle myosins by phosphorylation. *Annu Rev Biochem* **61**, 721-59.

Tao, Q., Nandadasa, S., McCrea, P. D., Heasman, J. and Wylie, C. (2007). G-protein-coupled signals control cortical actin assembly by controlling cadherin expression in the early Xenopus embryo. *Development* **134**, 2651-61.

Thevenaz, P., Ruttimann, U. E. and Unser, M. (1998). A pyramid approach to subpixel registration based on intensity. *IEEE Trans Image Process* **7**, 27-41.

Tint, I. S., Hollenbeck, P. J., Verkhovsky, A. B., Surgucheva, I. G. and Bershadsky, A. D. (1991). Evidence that intermediate filament reorganization is induced by ATP-dependent contraction of the actomyosin cortex in permeabilized fibroblasts. *J Cell Sci* **98 (Pt 3)**, 375-84.

Tokita, M. and Hikichi, K. (1987). Mechanical studies of sol-gel transition: Universal behavior of elastic modulus. *Phys Rev A* **35**, 4329-4333.

Tomasek, J. J. and Hay, E. D. (1984). Analysis of the role of microfilaments and microtubules in acquisition of bipolarity and elongation of fibroblasts in hydrated collagen gels. *J Cell Biol* **99**, 536-49.

Torpey, N. P., Heasman, J. and Wylie, C. C. (1990). Identification of vimentin and novel vimentin-related proteins in Xenopus oocytes and early embryos. *Development* **110**, 1185-95.

Trickey, W. R., Vail, T. P. and Guilak, F. (2004). The role of the cytoskeleton in the viscoelastic properties of human articular chondrocytes. *J Orthop Res* **22**, 131-9.

Tsai, M. and O'Malley, B. W. (1994). Molecular Mechanisms of Action of Steroid/Thyroid Receptor Superfamily Members. *Annual Review of Biochemistry* **63**, 451-486.

Uehata, M., Ishizaki, T., Satoh, H., Ono, T., Kawahara, T., Morishita, T., Tamakawa, H., Yamagami, K., Inui, J., Maekawa, M. et al. (1997). Calcium sensitization of smooth muscle mediated by a Rho-associated protein kinase in hypertension. *Nature* **389**, 990-4.

Valentine, M. T., Perlman, Z. E., Mitchison, T. J. and Weitz, D. A. (2005). Mechanical properties of Xenopus egg cytoplasmic extracts. *Biophys J* **88**, 680-9.

Van Aelst, L. and Symons, M. (2002). Role of Rho family GTPases in epithelial morphogenesis. *Genes Dev* **16**, 1032-54.

Verin, A. D., Birukova, A., Wang, P., Liu, F., Becker, P., Birukov, K. and Garcia, J. G. (2001). Microtubule disassembly increases endothelial cell barrier dysfunction: role of MLC phosphorylation. *Am J Physiol Lung Cell Mol Physiol* **281**, L565-74.

von Dassow, M. and Davidson, L. A. (2009). Natural variation in embryo mechanics: gastrulation in Xenopus laevis is highly robust to variation in tissue stiffness. *Dev Dyn* **238**, 2-18.

Wakatsuki, T., Kolodney, M. S., Zahalak, G. I. and Elson, E. L. (2000). Cell mechanics studied by a reconstituted model tissue. *Biophys J* **79**, 2353-68.

Wakatsuki, T., Schwab, B., Thompson, N. C. and Elson, E. L. (2001). Effects of cytochalasin D and latrunculin B on mechanical properties of cells. *J Cell Sci* **114**, 1025-36.

Wallingford, J. B., Fraser, S. E. and Harland, R. M. (2002). Convergent extension: the molecular control of polarized cell movement during embryonic development. *Dev Cell* **2**, 695-706.

Wang, N., Naruse, K., Stamenovic, D., Fredberg, J. J., Mijailovich, S. M., Tolic-Norrelykke, I. M., Polte, T., Mannix, R. and Ingber, D. E. (2001). Mechanical behavior in living cells consistent with the tensegrity model. *Proc Natl Acad Sci U S A* **98**, 7765-70.

Wang, N. and Stamenovic, D. (2000). Contribution of intermediate filaments to cell stiffness, stiffening, and growth. *Am J Physiol Cell Physiol* **279**, C188-94.

Wang, N., Tolic-Norrelykke, I. M., Chen, J., Mijailovich, S. M., Butler, J. P., Fredberg, J. J. and Stamenovic, D. (2002). Cell prestress. I. Stiffness and prestress are closely associated in adherent contractile cells. *Am J Physiol Cell Physiol* **282**, C606-16.

Watanabe, N., Kato, T., Fujita, A., Ishizaki, T. and Narumiya, S. (1999). Cooperation between mDia1 and ROCK in Rho-induced actin reorganization. *Nat Cell Biol* **1**, 136-143.

Wheeler, G. N., Hamilton, F. S. and Hoppler, S. (2000). Inducible gene expression in transgenic Xenopus embryos. *Current Biology* **10**, 849-852.

Wiebe, C. and Brodland, G. W. (2005). Tensile properties of embryonic epithelia measured using a novel instrument. *J Biomech* **38**, 2087-94.

Wilson, P. A., Oster, G. and Keller, R. (1989). Cell rearrangement and segmentation in Xenopus: direct observation of cultured explants. *Development* **105(1)**, 155-66.

Wu, Z. Z., Zhang, G., Long, M., Wang, H. B., Song, G. B. and Cai, S. X. (2000). Comparison of the viscoelastic properties of normal hepatocytes and hepatocellular carcinoma cells under cytoskeletal perturbation. *Biorheology* **37**, 279-290.

Yamada, S., Pokutta, S., Drees, F., Weis, W. I. and Nelson, W. J. (2005). Deconstructing the Cadherin-Catenin-Actin Complex. *Cell* **123**, 889-901.

Yang, J. T., Bader, B. L., Kreidberg, J. A., Ullman-Culler, M., Trevithick, J. E. and Hynes, R. O. (1999). Overlapping and Independent Functions of Fibronectin Receptor Integrins in Early Mesodermal Development. *Developmental Biology* **215**, 264-277.

Youn, B. W. and Malacinski, G. M. (1981). Axial structure development in ultraviolet-irradiated (notochord-defective) amphibian embryos. *Dev Biol* **83**, 339-52.

Zamir, E. A. and Taber, L. A. (2004a). Material properties and residual stress in the stage 12 chick heart during cardiac looping. *J Biomech Eng* **126**, 823-30.

Zamir, E. A. and Taber, L. A. (2004b). On the effects of residual stress in microindentation tests of soft tissue structures. *Journal of Biomechanical Engineering-Transactions of the Asme* **126**, 276-283.

Zeng, D., Ferrari, A., Ulmer, J., Veligodskiy, A., Fischer, P., Spatz, J., Ventikos, Y., Poulikakos, D. and Kroschewski, R. (2006). Three-dimensional modeling of mechanical forces in the extracellular matrix during epithelial lumen formation. *Biophys J* **90**, 4380-91.

Zhou, J., Kim, H. Y. and Davidson, L. A. (2009). Actomyosin stiffens the vertebrate embryo during crucial stages of elongation and neural tube closure. *Development* **136**, 677-688.